Dynamic trajectory planning and synthesis for fully actuated cable-suspended parallel robots

Thèse

Xiaoling Jiang

Doctorat en Génie Mécanique
Philosophiæ doctor (Ph. D.)

Québec, Canada

Dynamic trajectory planning and synthesis for fully actuated cable-suspended parallel robots

Thèse

Xiaoling Jiang

Sous la direction de:

Clément Gosselin, directeur de recherche

Résumé

Les tendances actuelles de la robotique requièrent une opération de plus en plus rapide dans un grand espace de travail. Afin d'adresser ces exigences, la conception de trajectoires dynamiques pour des robots parallèles suspendus entraînés par des câbles (RPSC) qui peuvent s'étendre à l'extérieur de l'espace de travail statique des robots est présentée. Des stratégies sont présentées pour explorer des trajectoires pendant lesquelles les tensions de tous les câbles est garantie d'être positive afin de respecter la propriété unilatérale des câbles.

Tout d'abord, la planification et la synthèse des trajectoires dynamiques périodiques sont investiguées pour des robots à trois degrés de liberté (DDL) de masse ponctuelle, des robots à trois DDL plans et des RPSC à six DDL. Sur la base d'une approche analytique, des trajectoires de translation pure et un mouvement plus complexe qui inclut des changements de position et d'orientation sont produits. Un système mécanique passif qui équivaut à un RPSC est présenté pour donner un aperçu et faciliter la conception de ces trajectoires. Il est démontré que les équations différentielles dynamiques qui gouvernent la partie de translation du mouvement pendant une trajectoire sont linéaires pour certaines conditions. Les fréquences naturelles du système linéaire équivalent sont obtenues et une généralisation des trajectoires périodiques est développée en intégrant ce système d'équations différentielles linéaires. Des trajectoires naturelles découlant d'un système à ressorts ayant une raideur constante et dont l'amplitude n'est pas restreinte sont obtenues. En utilisant cette formulation, la partie de rotation des RPSC à trois DDL plans devient un ressort non-linéaire dont la trajectoire peut être trouvée dans la littérature, ce qui réduit largement la complexité de la planification de la trajectoire. Pour les RPSC à six DDL, les angles d'inclinaison et de torsion sont utilisés pour définir les composantes de rotation des trajectoires et les conditions mathématiques correspondant aux trajectoires linéaires sont obtenues.

Les trajectoires périodiques ci-dessus donnent un aperçu des propriétés fondamentales du mécanisme et peuvent être utilisées dans certaines applications spécifiques. Cependant, la plupart des situations pratiques exigent que le robot passe d'un point cible à un autre. Une technique de planification de trajectoire dynamique point à point pour obtenir une série de points pour une masse ponctuelle de trois DDL est donc proposée. Chaque segment de trajectoire est conçu pour avoir une vitesse nulle à ses points d'extrémité. Cette formulation permet des trajectoires

qui s'étendent au-delà de l'espace de travail statique du robot. Un mouvement de base est introduit, qui est une fonction mathématique qui peut être adaptée pour chaque direction de coordonnées le long de chaque segment de trajectoire. Les contraintes cinématiques sont satisfaites grâce à la sélection des coefficients pour cette fonction. Les contraintes dynamiques sont imposées en définissant des régions réalisables à l'intérieur de l'espace de travail pour chaque point d'extrémité du segment, en fonction du point final précédent. Cette procédure est étendue à la planification de la trajectoire des RPSC à six DDL. Chaque segment de trajectoire est conçu pour avoir une vitesse de translation et de rotation nulle à ses points d'extrémité ; Les transitions entre chaque segment ont une accélération de translation et de rotation. En outre, une interpolation lisse et un évitement des singularités sont obtenus en utilisant une quaternion unitaire pour représenter la composante de rotation des trajectoires.

Ensuite, une technique de planification de la trajectoire de transition dynamique pour les RPSC de masse ponctuelle à trois DDL est proposée pour satisfaire une application réelle où le robot doit passer d'une trajectoire à une autre. Cette trajectoire est conçue pour faire la transition automatiquement entre plusieurs trajectoires pré-générées au-delà de l'espace de travail statique en séquence avec différents points de départ, ainsi que pour offrir la capacité de démarrer à partir de, et de terminer par, une position de repos tout en assurant un mouvement continu jusqu'au niveau de l'accélération. Deux trajectoires consécutives sont impliquées dans la transition, une trajectoire source et une trajectoire cible. En utilisant des fonctions de temps appropriées, la trajectoire cible est progressivement atteinte en approchant les paramètres d'amplitude et les fréquences de ceux de la trajectoire source. En outre, pour chaque transition, le point de départ de la trajectoire source, le point d'arrivée sur la trajectoire cible et le temps de transition est optimisé pour minimiser le temps de transition tout en respectant les contraintes du robot. Un exemple est fourni pour démontrer la nouvelle technique de planification de la trajectoire dans lequel le robot doit commencer à partir d'un état de repos, exécuter deux différentes ellipses consécutives, une ligne droite et un cercle en séquence, puis revenir à l'état de repos.

Enfin, une validation expérimentale des trajectoires périodiques et point-à-point est implémentée sur le prototype d'un RPSC à masse ponctuelle à trois DDL et d'un RPSC à six DDL. Des fichiers vidéo supplémentaires sont inclus pour démontrer les résultats.

Abstract

In the trend that robots are required to operate at increasingly high speeds and in large workspaces, dynamic trajectories of fully actuated cable-suspended parallel robots (CSPRs) that can extend beyond the robots' static workspace are designed. Due to the unilateral property of cables, strategies to explore trajectories during which cable tensions can be guaranteed to remain positive are proposed.

The planning and synthesis of dynamic periodic trajectories are first investigated for three-DOF point-mass, three-DOF planar, and six-DOF CSPRs. Based on an analytical approach, pure translation trajectories and more complex motion that includes changes in position and orientation are produced. A passive mechanical system that is equivalent to a CSPR is introduced to provide insight and facilitate the design of such trajectories. The dynamic differential equations that govern the translational component of the trajectories are shown to become linear under some conditions. Natural frequencies of the equivalent linear system are obtained and a generalization of periodic trajectories is accomplished by the integration of the linear system of differential equations. Natural trajectories associated with equivalent springs of constant stiffness and without any restriction of the amplitude are obtained. Using this formulation, the rotational component of three-DOF planar CSPRs becomes a nonlinear spring whose trajectories can be found in literature, which largely reduces the complexity of its trajectory planning. For six-DOF CSPRs, tilt and torsion angles are used to define the rotational component of the trajectories and the mathematical conditions corresponding to the linear trajectories are obtained.

The above periodic trajectories provide insight into the fundamental properties of the mechanism and can be used in some specific applications. However, most practical situations require that the robot moves from one target point to another. Thus, a point-to-point dynamic trajectory planning technique for reaching a series of points for a point-mass three-DOF CSPR is proposed. Each trajectory segment is designed to have zero velocity at its endpoints. This formulation allows for trajectories that extend beyond the static workspace of the robot. A basis motion is introduced, which is a mathematical function that can be adapted for each coordinate direction along each trajectory segment. Kinematic constraints are satisfied through the selection of the coefficients for this function. Dynamic constraints are imposed by defining fea-

sible regions within the workspace for each segment endpoint, based on the previous endpoint. This scheme is expanded to the trajectory planning of a six-DOF CSPR. Each trajectory segment is designed to have zero translational and rotational velocity at its endpoints; transitions between segments have translational and rotational acceleration. Additionally, smooth interpolation and singularity avoidance is achieved by using a unit quaternion to represent the rotational component of the trajectories.

Then, a dynamic transition trajectory planning technique for three-DOF point-mass CSPRs is proposed to satisfy a real application where the robot is required to move from one trajectory to the next. This trajectory is designed to automatically chain multiple pre-generated trajectories beyond the static workspace in sequence with different starting points, as well as have the ability of starting from/ending with a resting position, while ensuring continuity up to the acceleration level. Two consecutive target trajectories are involved in the transition trajectory by using proper time functions, such that a goal trajectory is gradually reached by approaching the amplitude parameters and frequencies from those of a source trajectory. Additionally, each transition is based on the optimization of the departure point from its source trajectory and a minimum time for the transition to its goal trajectory. An example is provided to demonstrate the novel trajectory-planning technique. The robot is requested to start from the state of rest, merge into two consecutive ellipses, a straight line and a circle in sequence and then go back to the state of rest.

Finally, experimental validation of the periodic and point-to-point trajectories is implemented on the prototype of a three-DOF point-mass CSPR and a six-DOF CSPR. Supplementary video files are included to demonstrate the results.

Contents

List of Tables

List of Figures

List of the video extension

All the videos are available in the following address:

http://robot.gmc.ulaval.ca/publications/these-de-doctorat

in the section Xiaoling Jiang.

Foreword

First and foremost, I would like to thank my supervisor Prof. Clément Gosselin for giving me the chance to join his team, his precious time and supervision, his tremendous support and encouragement over the last years. His charming personality, creativity, openness to various ideas and belief in his students has been a continuing source of inspiration. His comprehensive expertise in robotics and mechanisms has been keeping me always on track and has given me great enthusiasm to discover what else could be accomplished.

I would like to give my sincere gratitude to Mr. Simon Foucault and Dr. Eric Barnett for their precious help during the experimental validation of the project. Without their superior knowledge and experience on the robotic mechanisms, the implementation would not have smoothly advanced. Special thanks are given to Dr. Eric Barnett for giving comments and support on our two articles.

Then, I wish to express my gratitude to my thesis defence committee and especially to Prof. Marco Carricato from University of Bologna, Prof. Philippe Cardou and Prof. Yves St-Amant from Laval University. Their detailed remarks and suggestions are valuable to modify the final version of my thesis.

Furthermore, I would like to acknowledge all the members of the Robotics Laboratory for their help and friendship as well as for their contributions to creating the most pleasing working atmosphere that I ever enjoyed. Special thanks are given to my dearest friends and colleagues, Dr. Dinh-Son Vu and Mr. André Gallant, for their great help in different aspects and for their invaluable friendship. I would also like to thank Mr. François Guay for his help when I was looking for a postdoctoral position.

Last but not least, I am deeply indebted to my family. Without their love and understanding, this work would not have been possible.

Chapter 1

Introduction

1.1 General Background

Cable-driven parallel robots (CDPRs) possess some desirable features and have therefore attracted the interest of researchers. With cables wound on spools, these robots can potentially provide a very large workspace (Gosselin, 2014). Since cables have negligible inertia and mass, they are particularly suitable for systems that require high-performance and high-speed applications, as evidenced by the design of FALCON-7 (Kawamura et al., 1995, 2000) and SEGESTA (Bruckmann et al., 2006). Indeed, conventional parallel robots involve the motion of significant mass while cable mechanisms remain light even during large motions. The most essential issue in CDPRs is that the robots can only operate properly if positive cable tensions are ensured during the robot motion since cables can only pull the end-effector but cannot push on it (Merlet, 2013). Therefore, the relationship between the pose and the feasible wrenches at the platform is a fundamental issue for CDPRs.

Several definitions and the determination of the workspace can be found in the literature. One particularly relevant concept is that of wrench closure workspace (WCW) (Gouttefarde and Gosselin, 2006), which can be defined as the set of poses of the platform for which any wrench applied on the platform can be balanced by pulling on the cables. Different approaches were applied to provide an effective way of determining the boundaries of WCW, see for instance in (Gouttefarde et al., 2006; Stump and Kumar, 2006; Azizian et al., 2012; Pott and Kraus, 2016; Li et al., 2016). In (Bosscher and Ebert-Uphoff, 2004; Gouttefarde et al., 2007, 2011; Duan et al., 2015), wrench feasible workspace (WFW) is defined and used for the design of a CDPR that can be better tailored to a given set of tasks. This workspace is the set of poses in which the cable tensions (remaining below a given maximum) can balance any platform wrench belonging to a set of prescribed wrenches. The shape and size of the WFW depends on the geometry of the mechanism, on the maximum cable tensions, and on the shape and size of the required wrench set. In (Barrette and Gosselin, 2005), the dynamic workspace for specific directions of motion and accelerations of a CDPR was studied. By dynamically

controlling CDPRs, useful workspace can be extended beyond the static workspace. The dynamic workspace is defined as the set of poses that the platform can reach with at least one kinematic state (position, velocity and acceleration) with all cables in tension. In other words, the platform can reach points beyond the static workspace with a controlled kinematic state (e.g. a zero velocity but non-zero acceleration) (Barrette and Gosselin, 2005). This can be applied in some cases that require very large workspace and fast speed.

A well-known result in the literature on CDPRs is that at least $n+1$ cables are required in order to fully constrain an n-degree-of-freedom (n-DOF) CDPR. By the use of optimization of redundant cables, a proper distribution of the cable tensions for given trajectories can be exerted and large internal forces can be avoided. Four performance indices were proposed in order to solve the underdetermined problem associated with the distribution of the forces in (Gosselin and Grenier, 2011). Possible tension distribution algorithms can be found in (Pott, 2014; Gouttefarde et al., 2015b; Fortin-Côté et al., 2016) and the design of efficient control schemes were proposed in (Ming and Higuchi, 1994; Reichert et al., 2015; Kraus, 2015; Khosravi and Taghirad, 2014; Babaghasabha et al., 2015). However, in under-constrained CDPRs, the difficulties of control are slightly different since there generally exists no configuration in which internal forces can be generated.

Cable-suspended parallel robots (CSPRs) are a class of under-constrained CDPRs in which the tensioning is generally generated by gravity. Since the workspace below the platform is free of cables, collision risks between cables and obstacles can be reduced. The first commercial application of CSPRs was the Skycam shown in Fig. 1.1, which is a large CSPR that is positioned above a stadium field for filming sports events and other performances (Cone, 1985). Since cables are small and hardly visible, the Skycam does not perturb the visibility for the local audience. In industry, the NIST RoboCrane (Albus et al., 1993), with six controllable degrees of freedom, was proposed for stabilizing crane loads. The NIST RoboCrane, shown in Fig. 1.2, was introduced as an upside-down Gough–Stewart platform with triangular base and platform. They were designed to carry on a series of application research on assembly, lifting, spraying, and building with the cable robot. More recently, CSPRs have been applied in the development of very large radio-telescopes, such as the five-hundred-metre aperture spherical radio telescope (FAST) (Nan et al., 2011; Yao et al., 2010; Liu et al., 2013), shown in Fig. 1.3, developed in China.

Researches on the design, planning and control of CSPRs can be found in (Alp and Agrawal, 2002; Oh and Agrawal, 2003; Pusey et al., 2004; Berti et al., 2015) and many other prototypes of CSPRs for different applications can be found in the literature. An example of a CSPR with six cables was developed in Laval University and was used for scanning of large artefacts (Gosselin and Bouchard, 2010) (more specifically, taking photos of artefacts from a large number of camera poses in order to construct a digital model), shown in Fig. 1.4, and for large-scale 3D printing (Barnett and Gosselin, 2015a), shown in Fig 1.5. Objects of sizes from

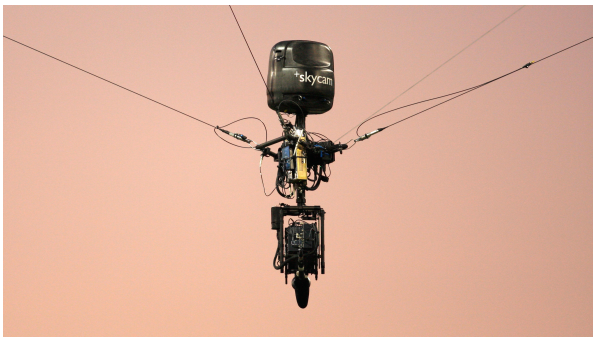

Figure 1.1 – Skycam.

Figure 1.2 – The mobile 2 m octahedral gantry frame RoboCrane mounted to three skid-steer trucks.

a few centimetres to several meters were successfully scanned and printed. In the Germany Pavilion at the EXPO 2015, an exhibition system, shown in Fig. 1.6, was built by applying two CSPRs (Tempel et al., 2015) each consisting of a platform looking like the eye of a bee and eight cables controlled by winches. Elsewhere, the project CoGiRo, "Control of Giant Robots", uses eight-cable six-DOF CSPRs, shown in Fig. 1.7, to achieve large workspaces and possibly handling heavy to very heavy payloads. The CoGiRo appears as a good compromise between complexity, geometric balance and workspace capabilities (Lamaury et al., 2012; Nguyen et al., 2013; Lamaury and Gouttefarde, 2013; Gouttefarde et al., 2015a).

1.2 Trajectory Planning

Conventionally, robot control algorithms are divided into two stages, namely, path/trajectory planning and path tracking/control. The path tracker attempts to make the actual position and velocity of the robot to match their desired values which are provided to the controller

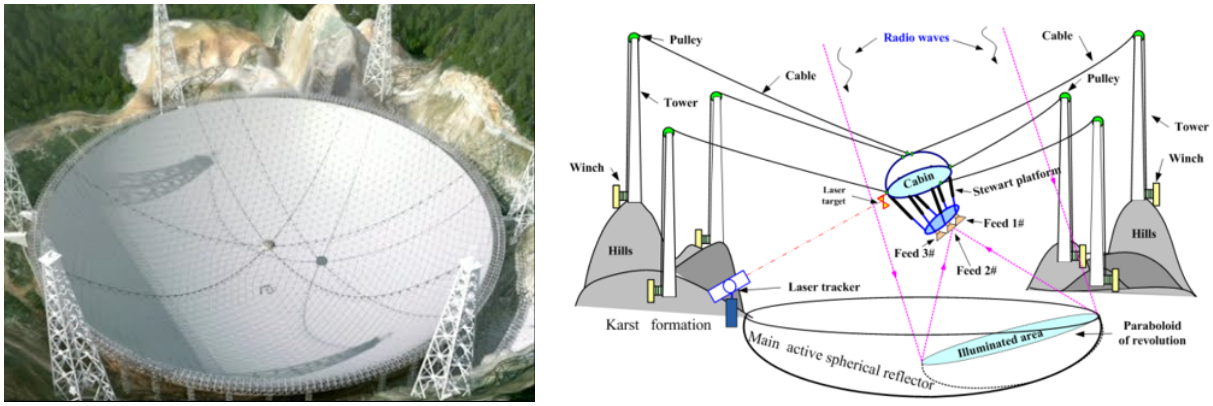

(a) (b)

Figure 1.3 – The five-hundred-metre aperture spherical radio telescope (FAST) developed in China

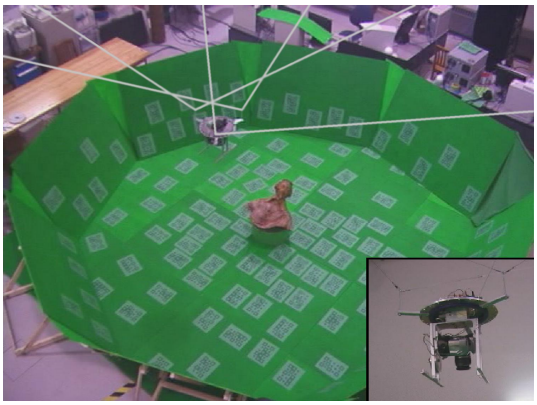

Figure 1.4 – Prototype of a six-DOF CSPR for the scanning of artefacts.

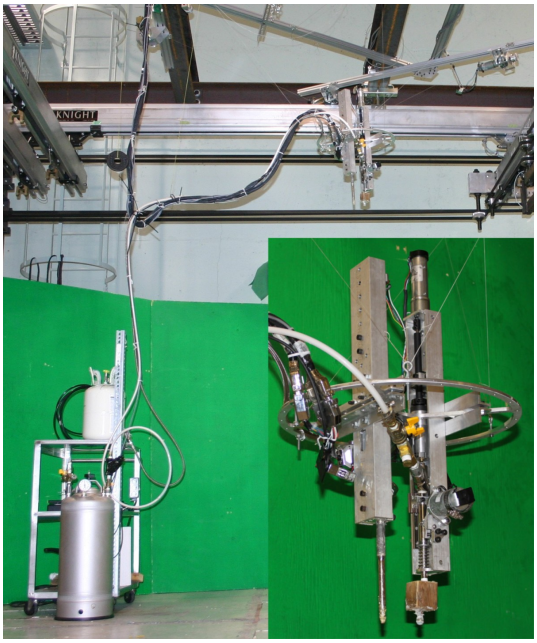

Figure 1.5 – Prototype of a six-DOF CSPR for 3D printing of large objects.

by the trajectory planner. A time history of the desired positions and velocities are computed and sent as input into the trajectory planner. Then, the path tracker minimizes the deviation of the actual position and velocity from the desired values (Shin and McKay, 1985a; Chettibi et al., 2004).

This division has been adopted mainly as a means of alleviating difficulties in dealing with robot dynamics which is complicated, highly nonlinear and coupled. Trajectory planning usually determines the kinematic and geometric constraints without considering the robot's

Figure 1.6 – Cable robots in the German Pavilion at the World Exhibition EXPO 2015 in Milan.

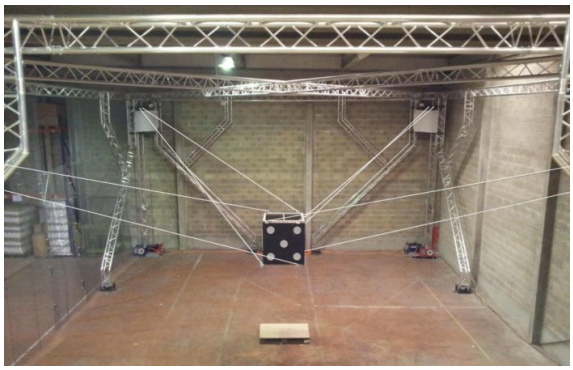

Figure 1.7 – CoGiRo: A large-dimension cable-driven parallel robot.

dynamics while the path tracker is frequently a linear controller, such as a PD/PID controller. Consequently, the simplicity due to the division comes at the expense of efficiency in utilizing robot capabilities. This inefficiency arises from the trajectory planning. Indeed, instead of considering the robot dynamics, constant or piecewise constant bounds on the robot's velocity and acceleration are assumed (Luh and Walker, 1977). Global greatest lower bounds of the values must be chosen. Such bounds can result in considerable inefficiency or underutilization of the robot, since these bounds vary with position, payload mass, and also with payload shape.

Additionally, trajectory planning based on kinematic models can produce very high execution velocities, particularly when transfer time is minimized. It induces excessive torque amplitudes which can be harmful for the system state. Therefore, it is desirable to incorporate dynamic models for a more realistic control of the robot dynamic behaviour. This becomes more significant especially in the trend that robots are designed to operate at increasingly very high execution velocity in order to achieve shorter production time. Indeed, high operating speed requires extreme performance from the actuators and the control system. Publications dealing with trajectory planning involve a variety of problems and a large diversity of solution schemes. Since many different ways are possible to perform the same task, algorithms of trajectory planning are exploited for the optimization of a given performance criterion (LaValle, 2006; Gasparetto et al., 2015; Donald and Xavier, 1995; Fraichard and Laugier, 1993b,a).

The minimum-time motion problem along specified paths using the phase plane method was among early techniques taking into account the robot dynamic behaviour and limitations of the actuator torque (Bobrow et al., 1985; Shin and McKay, 1985b; Pfeiffer and Johanni, 1987; Shiller and Lu, 1992; Žlajpah, 1996). This method was extended to the design of free motions as well (Shiller and Dubowsky, 1989). The arc length and velocity of the end-effector along the specified path was taken as the state vector. The dynamics as well as constraints that can be formulated in terms of the trajectory parameter and its time derivatives were converted

into bounds on parametric accelerations along the path. The maximum velocity capacity of a given path was obviously expressed by a minimum time trajectory which makes use of maximum acceleration/deceleration power of the manipulator. In (Bobrow et al., 1985; Shin and McKay, 1985b), switching points along the path were determined in a numerical search procedure. In (Pfeiffer and Johanni, 1987), these points were found in a computationally very efficient way. The properties of the boundary curve of velocity were illustrated which leads to a very illustrative method to find the maximum velocity.

For many robotic systems, trajectory planning can be accomplished by considering only kinematic and geometric constraints. However, for CSPRs, dynamic constraints must also be considered in most cases, due to the unilateral tension property of cables. Several techniques have been proposed for CSPR trajectory planning. In (Bohigas et al., 2016), wrench-feasible trajectories were designed for cable-driven hexapods. In (Barnett and Gosselin, 2015b; Fahham and Farid, 2010; Bamdad, 2013), trajectories were planned to minimize the time required to follow fully specified paths. Some of these techniques adapted a trajectory planning approach developed for serial manipulators (Bobrow et al., 1985; Shin and McKay, 1985b; Pfeiffer and Johanni, 1987). Elsewhere, the dynamic load-carrying capacity defined in (Korayem and Bamdad, 2009) was taken into account in the formulation of optimal trajectories for CSPRs (Korayem et al., 2010, 2012).

More recently, dynamic trajectories of pendulum-like CSPRs for point-to-point operations were found in the literature. Additionally, dynamic trajectories of fully actuated CSPRs, including periodic trajectories, point-to-point trajectories and transition trajectories, were investigated. Since these trajectories can extend beyond the robot's static workspace, they can potentially be used for many novel CSPR applications.

1.2.1 Dynamic Trajectory Planning of Underactuated CSPRs

For point-to-point trajectory planning, underactuated CSPRs (pendulum-like robots) were first introduced. Due to the underactuation, only a subset of the kinematically possible global trajectories are achievable. Nevertheless, in a point-to-point operation, a full control of the end-effector is not required since one may not be interested in the actual path followed by the robot. Thus, pendulum-like robots are very well suited in these situations by offering simple and cost-effective design solutions.

The MIT Winch-Bot shown in Fig. 1.8 is a pioneer design for investigating pendulum-like CSPRs. The robot only has one controllable axis but actuates two degrees of freedom (Cunningham and Asada, 2009). The known properties of the Mathieu Equation were used to accommodate the swing amplitude and energy level in the point-to-point motion with soft-landing capabilities. However, the control algorithm is based on an off-line trajectory planning. It requires specific initial conditions that may be incompatible with the architecture or the

current configuration of the robot.

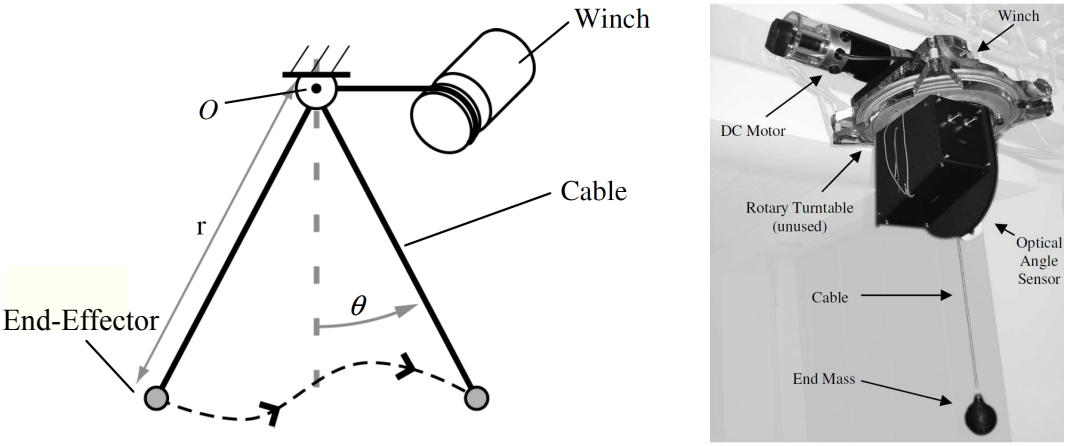

(a) Schematic diagram (b) Prototype

Figure 1.8 – Winch-bot.

To alleviate these drawbacks, different techniques were proposed, which require on-line numerical integration of the differential equations associated with the manipulator dynamics. In order to produce point-to-point motion between prescribed poses, the techniques focus on approaches of controlling the actuator inputs.

In (Lefrançois and Gosselin, 2010), a three-DOF underactuated serial pendulum-like device shown in Fig. 1.9, capable of point-to-point motions on a planar workspace, was studied. Inspired from the physics of children pumping playground swings (Case and Swanson, 1990; Case, 1996; Piccoli and Kulkarni, 2005), an effective and robust trajectory planning scheme that allows the real-time control of the robot was provided. Sine-like functions were used as the actuated joint trajectory, using the natural frequency of the system and the pendulum-like natural motion of the robot. In (Zanotto et al., 2011), a novel design for a three-DOF pendulum-like cable-based device was introduced. The system was decoupled by applying a convenient input-state transformation and thus the control algorithm was simplified. As a result, the uncontrolled dynamics reduce to those of an equivalent variable-length pendulum, whose behaviour has been explored (Belyakov et al., 2009; Stilling and Szyszkowski, 2002).

Serial cable-suspended architecture can hardly be extended to a spatial robot and thus a three-DOF parallel underactuated CSPR shown in Fig. 1.10 was designed (Zoso and Gosselin, 2012) in which both actuators are fixed to the ground and no actuator is mounted on the suspended body. A trajectory planning approach was developed, which was based on the natural frequency of the pendulum-like free motion (unconstrained degree of freedom). Sine-like excitation functions were used and their frequency and phase delay were determined using simulation results. The experimental results confirmed that the robot presented in this article

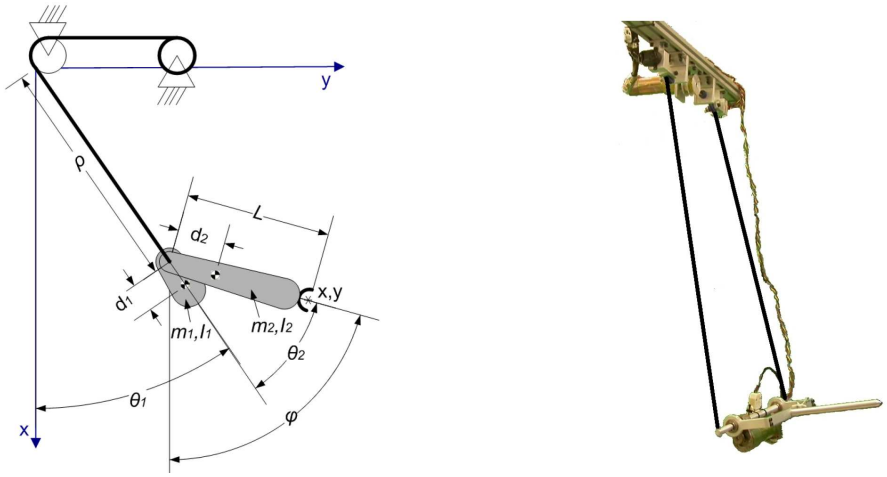

(a) Schematic diagram (b) Prototype

Figure 1.9 – A three-DOF underactuated cable-suspended serial robot.

was effective enough to be used for point-to-point trajectories. Other work can also be found in (Idá et al., 2018).

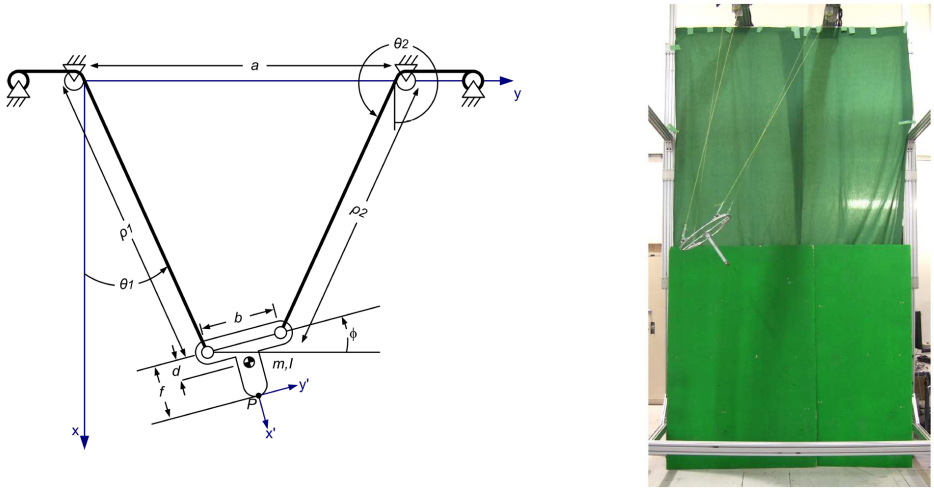

(a) Schematic diagram (b) Prototype

Figure 1.10 – A three-DOF planar underactuated CSPR.

1.2.2 Dynamic Trajectory Planning of Fully Actuated CSPRs

With fewer actuators than degrees of freedom, the control problem is challenging (Fantoni and Lozano, 2002) for underactuated CSPRs, since the motion of the unactuated joints is generally related to that of the other joints by complex dynamics. In order to alleviate the trajectory planning, fully actuated CSPRs, having the same number of actuators as degrees of freedom, were studied. The fact that all the degrees of freedom of fully actuated robots can be controlled makes the trajectory planning much easier. The algorithms used for the

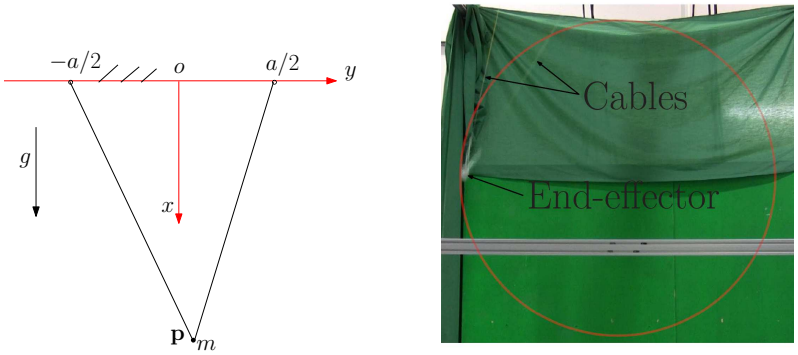

(a) Schematic diagram (b) Prototype

Figure 1.11 – A two-DOF CSPR with a point-mass end-effector

trajectory planning of underactuated robots focus on controlling the actuator inputs to reach prescribed target points. As opposed to that, algorithms for the trajectory planning of fully actuated CSPRs are based on prescribed continuous Cartesian trajectories.

Dynamic Periodic Trajectory Planning

A dynamic periodic trajectory planning approach for point-mass CSPRs was developed, which globally guarantees that cables remain taut and does not need to verify or impose tension constraints *locally* along the trajectory. A planar two-DOF robot with a point-mass end-effector suspended on two cables, schematically shown in Fig. 1.11, was considered in (Gosselin et al., 2012). A series of periodic trajectories were defined parametrically as analytic functions of time, revealing the existence of certain oscillation frequencies for which the equations of motion become linear, with constant ratios between the force and length for each cable. This approach greatly reduces the complexity of algebraic cable tension calculations and allows for the design of periodic trajectories that can always be feasible, with theoretically unbounded amplitude. The approach was expanded to a spatial three-DOF CSPR with a point-mass end-effector in (Gosselin, 2013), shown in Fig. 1.12. However, the generalization of the periodic trajectories are not addressed and the role that special oscillation frequencies play in the dynamic equations is unveiled yet.

Dynamic trajectories for three-DOF point-mass CSPRs that can go beyond the static workspace can also be found in some other work. In (Schmidt et al., 2014), a user-friendly approach was proposed to extend and control the dynamic trajectories designed in (Gosselin et al., 2012; Gosselin, 2013). In (Zhang and Shang, 2016; Zhang et al., 2017), a geometry-based trajectory planning approach was introduced, with periodic linear and circular trajectories designed in the position-acceleration phase plane.

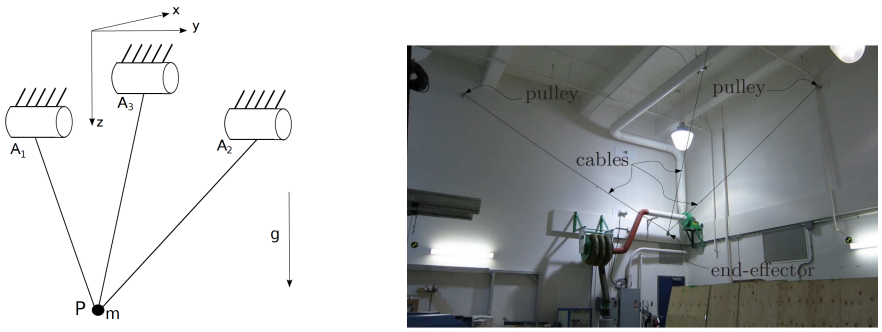

(a) Schematic diagram (b) Prototype

Figure 1.12 – A three-DOF CSPR with a point-mass end-effector

Dynamic Point-to-Point Trajectory Planning

Periodic trajectories provide insight into the fundamental properties of CSPRs and it is found that these properties can be applied when robots are required to move between prescribed points in sequence. The planning of trajectories with the segment connecting consecutive points that have a zero instantaneous velocity at its end points as well as to ensure continuity of the accelerations were investigated. These trajectories can go beyond the static workspace. In (Gosselin and Foucault, 2014), the dynamic trajectory planning of a planar two-DOF point-mass CSPR was addressed. Polynomial trajectories and trajectories based on trigonometric functions were proposed. The main advantage of the latter is that the feasibility can be verified by using simple algebraic expressions and does not require a discretization of the trajectory. However, in order to ensure the continuity of the acceleration, the frequency associated with the motion corresponding to an interval has to be calculated based on the preceding interval. This greatly reduces the chances of obtaining feasible target points. Although this limitation is not a critical issue for the two-DOF robot studied in (Gosselin and Foucault, 2014), it may be more significant for spatial systems with three DOFs or even six DOFs. In spatial systems, target points are no longer located on any of the vertical planes defined by the cable attachment points and thus it is not intuitive to find proper target points. Predicting a region for the next target points then becomes a very useful tool. Moreover, (Gosselin and Foucault, 2014) does not address the case where target points are not feasible and the possible introduction of intermediate points.

In (Zhang and Shang, 2016; Zhang et al., 2017), a straight line path was applied for the trajectory planning of a three-DOF CSPR with a point mass. Although any prescribed points that are located in a feasible workspace can be reached, the robot has to follow specified points in sequence since it only goes along straight lines. This limitation may result in inefficiency as some points have to be reached repeatedly.

Dynamic Transition Trajectory Planning

The periodic trajectories obtained in the above references do not include points representing the state of rest. Thus, transition trajectories were also proposed in (Gosselin et al., 2012; Gosselin, 2013; Zhang and Shang, 2016; Zhang et al., 2017) to start from rest and blend into a periodic motion, and to end a periodic motion by returning to the state of rest. The transition trajectories were obtained by progressively increasing the amplitude of motion during the first phase of the trajectory, until the steady-state periodic trajectory is reached. In (Dion-Gauvin and Gosselin, 2017), transition trajectory planning was accomplished using the ideal kinematic states, which yield mathematical expressions that have the same signs as the cable forces, thereby providing a means to produce *dynamically feasible* trajectories. However, in a real application the robot is required to move from one trajectory to the next in order to automatically chain multiple pre-generated trajectories with different starting points. This could be useful since feasible generic trajectories can be used as building blocks to synthesize more complex trajectories.

1.3 The Representation of Orientations

Most of the trajectory planning techniques in the literature related to CSPRs are for *translational* motion; rotational trajectory planning is still a challenge. Translation can be well described by curves in R^3. However, the case for representing the motion of rotational component is different since the curve is formulated in $SO(3)$, that is

$$SO(3) = \{\mathbf{Q} \in \mathbb{R}^{3\times 3} : \mathbf{Q}\mathbf{Q}^T = \mathbf{1}, \det \mathbf{Q} = +1\},$$

where $\mathbf{Q}$ represents the rotation matrix. The notation SO abbreviates *special*, *orthogonal*. Special refers to the fact that $\det \mathbf{Q} = +1$ rather than ± 1.

In three-dimensional space, according to *Euler's rotation theorem*, any rotation or sequence of rotations of a rigid body or coordinate system about a fixed point is equivalent to a single rotation by a given angle about a fixed axis (called the *Euler axis*) that runs through the fixed point. The Euler axis is typically represented by a unit vector. Therefore, any rotation in three dimensions can be represented as a combination of a unit axis vector and an angle.

1.3.1 Euler Angles

The Euler angles provide the most popular description of rigid body orientation. They are three angles introduced by *Leonhard Euler* to describe the orientation of a rigid body with respect to a fixed coordinate system. Any orientation can be achieved by composing three elemental rotations, i.e., rotations about the axes of a coordinate system. In each elemental rotation, an orientation can be described by only specifying the angles of the rotations, in

analogy to describing the orientation in a plane using a single angle. In (Tempel et al., 2015), Euler angles are used for rotational trajectory planning for CSPRs.

The order in which the three rolls are performed is important, due to the fact that rotations in space do not generally commute. There are twelve different sequences of the three rotations, and hence, there can be twelve Euler-angle conventions. In addition, the conversion from a general rotation to Euler angles is ambiguous since the same rotation can be obtained with different sets of Euler angles. Although different possible conventions and their multiple interpretations bring a certain confusion in the use of the term Euler angles, standard convention has been established in different fields. For example, the zyz convention is usually employed in robotics and the xyz convention is used with the three angles *roll, pitch* and *yaw* in aeronautical engineering. Moreover, according to the property of the system, different conventions are modelled. The convention with three different axes suits well when small orientations occur frequently, while the use of only two axes gives a clearer geometric picture of an orientation defined by an arbitrary set of Euler angles. Nevertheless, Euler angles have several other drawbacks compared to alternative approaches.

1.3.2 Rotation Matrices

Rotation matrices, representing the orientation of a frame with respect to another, are a typical choice for implementing Euler angles. When $\mathbf{Q}$ represents a rotation at an angle α about a coordinate axis, it has the form, denoted as $\mathbf{Q}_x(\alpha)$, $\mathbf{Q}_y(\alpha)$ and $\mathbf{Q}_z(\alpha)$. Multiplying them with the position vector for a point in space gives the position vector for the rotated point. An advantage of matrix implementations is that the mathematics is well-known and that matrix applications are relatively easy to implement. However, the matrix representation of Euler angles has an innate singularity in the parametrization and it is not suitable for the interpolation of a sequence of orientations, mainly due to the following two disadvantages (Dam et al., 1998):

- Gimbal lock. The gimbal lock occurs when two of the three Euler angles become dependent and a degree of freedom is lost. Singularities can never be eliminated in any three-dimensional representation of $SO(3)$. Due to singularities, the differential properties of $\mathbf{Q}(t)$ and the Euler angles may not be preserved.

- Implementing interpolation is difficult. Normally the coordinates of each basis axis are interpolated independently, thereby the interdependencies between the axes are ignored. This results in unexpected effects that $\mathbf{Q}(t)$ cannot preserve the intrinsic property, i.e., $\det(\mathbf{Q}(t)) = 1$ easily.

1.3.3 Quaternions

Quaternions are hyper-complex numbers consisting of one real and three imaginary parts. The quaternions were discovered by sir W. R. Hamilton in 1843, after several years of trying to find an extension to complex numbers. Analog to the unit complex numbers—i.e., numbers of the form $e^{i\theta} = \cos(\theta) + i\sin(\theta)$— that can describe rotations in the plane, unit quaternions provide a convenient mathematical notation for representing orientations and rotations of objects in three-dimensional space.

Unit quaternions, a globally non-singular representation of rotation, are frequently used for the interpolation of orientation in computer graphics, animation, and robotics (Campa and Camarillo, 2008). The geometric interpretation of rotation is simpler using quaternions, which involve one rotation about a single axis; Euler angles are represented by rotations about three explicit axes. Quaternions also permit interpolation between orientations to be achieved more readily, and they are not subject to gimbal lock. Additionally, since the interdependencies between the axes are automatically taken into account during interpolation, the intrinsic property can be well preserved.

1.4 Objectives and Overview of the Thesis

This thesis aims at developing synthesis approaches for the planning of dynamic trajectories of fully actuated CSPRs, including periodic trajectories, point-to-point trajectories and transition trajectories. These trajectories can go beyond the static workspace of the robot. For this purpose, the kinematics and dynamics of the mechanisms are analysed in detail. An analytical method that involves linearizing the dynamic equations is introduced to produce periodic trajectories, while a basis motion is introduced that yields a systematic way of planning point-to-point trajectories. A general, simple but effective method is proposed for the generation of transition trajectories in which a target trajectory can be gradually achieved from a source trajectory. For the implementation and experimental evaluation, a spatial three-DOF point-mass CSPR prototype and a six-DOF CSPR prototype are used. The experimental evaluation is only intended as a proof of concept that can demonstrate that the designed trajectories are feasible and clearly exit the static workspace. The overview of the thesis is as follows.

The first part introduces an analytical approach for the planning of periodic trajectories that can be guaranteed to be feasible, i.e., the cables are guaranteed to remain in tension during the whole trajectory. In Chapter 2, a one-DOF point-mass CSPR is first investigated in order to show the process of linearizing its dynamic equation which is obtained by replacing the cables with constant-stiffness springs and with zero free length. Natural frequencies as well as associated periodic trajectories are obtained from the integration of the dynamic model of this equivalent mass-spring system. This method is then extended to the periodic trajectory planning of a three-DOF point-mass CSPR. A series of natural trajectories associated with

constant-stiffness equivalent springs are obtained. In Chapter 3, an equivalent mass-spring system of a three-DOF planar CSPR is first introduced. The translational component is integrated from the linearized differential equations. Correspondingly, the differential equation that governs the rotational component becomes a nonlinear differential equation but with constant coefficients. Therefore, the solution for the rotational component can be found in the literature. In Chapter 4, the conditions that define linear trajectories are first introduced. Then, following the same reasoning for the translational components in the preceding chapters, natural trajectories associated with constant-stiffness equivalent springs are obtained. Moreover, extended linear trajectories associated with variable-stiffness equivalent springs are designed and corresponding global conditions that can keep the cables in tension are obtained. Finally, example trajectories are provided and videos of the implementation on prototypes are included in order to illustrate the results.

The second part proposes a systematic approach for the generation of dynamic point-to-point trajectories by using a basis motion. These trajectories are designed to connect consecutive points in sequence that may extend beyond the static workspace of the robot. The technique ensures zero velocity at each of the target points and continuity of the accelerations. The dynamic model for the robot is used for planning each trajectory segment, which ensures that cables always remain in tension. In Chapter 5, a linear trajectory in one dimension is first represented by adding the kinematic constraints at endpoints of a trajectory segment. The basis motion which is suitable to produce zero or non-zero acceleration at the end of each trajectory segment is introduced. This novel trajectory-planning technique using this motion is then applied for a specific architecture. In Chapter 6, the quaternion-based kinematic and dynamic models of the mechanism are first obtained. Then, the linear trajectory segment and the basis motion introduced in Chapters 5 are extended to the point-to-point trajectory generation of a six-DOF CSPR, including the translational component and the rotational component. Both in Chapters 5 and 6, attainable regions are determined to search for the next target point, while feasible regions of intermediate points are generated in cases for which a given point cannot be directly attained. Example trajectories and experimental results are applied for a specific architecture. Finally, videos of the implementation on the prototype of a three-DOF point-mass CSPR and a six-DOF CSPR are included in order to illustrate the results.

Chapter 7 which composes the third part of this thesis shows the design of transition trajectories which can be used to combine feasible trajectories in sequence as well as have the ability that allow the robot to start from/end with the state of rest, while respecting cable force constraints. Kinematic and dynamic models of the mechanism are first presented. The novel transition trajectory planning technique in which a target trajectory is gradually attained from a source trajectory is then introduced. Example trajectories are provided to demonstrate the scheme.

In the last chapter, some discussion and a summary of the contributions obtained in this thesis, as well as future work are given.

1.5 Notation and Assumptions

In this thesis, each cable is assumed to be massless and inelastic, and passes through a guide such as an eyelet before extending in a straight line to an attachment point on the end-effector (platform). The kinematic model of a cable robot is represented schematically in Fig. 1.13. Relevant symbols which are used throughout this thesis are explained in the following.

- $\mathcal{F}_O$ is the fixed reference frame with the origin O located at the centroid of the base.
- $\mathcal{F}_P$ is the moving reference frame with the origin P located at the centre of mass of the end-effector.
- $\mathbf{b}_j$ is the position vector of the attachment point B_j of the jth cable on the ground expressed in $\mathcal{F}_O$. The points corresponding to the cable outputs of the spools are assumed to be fixed, in practice an eyelet or a pulley can be used.
- $\mathbf{a}_j$ is the position vector of the attachment point A_j of the jth cable on the end-effector expressed in $\mathcal{F}_P$.
- $\mathbf{Q}$ is the rotation matrix from the fixed frame to the moving frame.
- $\mathbf{p}$ is the position vector of the centre of mass of the end-effector with respect to the origin of the fixed reference frame. $\ddot{\mathbf{p}}$ is the acceleration vector of the centre of mass of the end-effector.

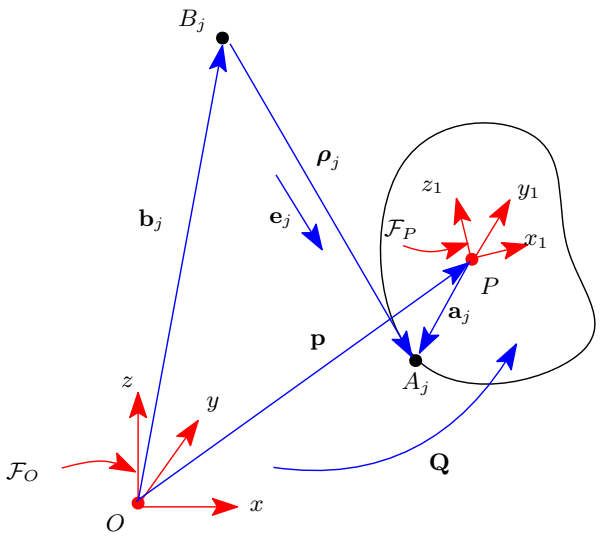

Figure 1.13 – Kinematic model of a CSPR.

- $\boldsymbol{\omega}$ and $\dot{\boldsymbol{\omega}}$ are respectively the angular velocity vector and angular acceleration vector of the moving platform with respect to the moving frame.
- $\boldsymbol{\rho}_j$ is the vector connecting point B_j to point A_j along the jth cable and ρ_j is its length.
- $\mathbf{e}_j = \boldsymbol{\rho}_j/\rho_j$ is a unit vector in the direction of the jth cable and oriented from the base to the end-effector.
- m is the mass of the end-effector.
- f_j is the tension in the jth cable.
- $k_j = f_j/\rho_j$ is the jth cable stiffness of equivalent spring with zero free length.
- $\mathbf{g}$ is the vector of gravitational acceleration, whose magnitude is g and which is assumed to be directed in the negative direction of the z axis of the fixed coordinate frame.
- A plural form of an item h_j is denoted $\{h_j\}_1^c$, which means that $\{h_j\}_1^c$ represents h_1,..., h_c whereas c is the number of cables.

Part I

Dynamic Periodic Trajectory Planning

Chapter 2

Dynamic Periodic Trajectory Planning of Point-Mass CSPRs

2.1 Introduction

For most of the prior work on dynamic trajectory planning for CSPRs, the dynamic equations governing the motion of cable robots are used as constraints that can keep the cables under tension (Gosselin et al., 2012; Gosselin, 2013; Schmidt et al., 2014; Zhang and Shang, 2016). However, in order to facilitate the trajectory planning and provide insight into the fundamental properties of CSPRs, natural trajectories are designed. These trajectories are based on the equivalent passive mechanical system with springs of *constant* stiffness and with zero free length. If such motions are then followed by the robot, it can be guaranteed that the cable tensions will be positive at all times because the spring forces of the passive free vibrating system are positive at all times. The results obtained generalize the harmonic trajectories obtained in (Gosselin et al., 2012; Gosselin, 2013) and highlight the critical role that special oscillation frequencies play in the dynamic equations.

This chapter proposes a periodic trajectory generation technique for fully actuated CSPRs with point mass. In Section 2.2, the process of determining natural frequencies and response of the equivalent linear system is recalled by introducing a one-DOF point-mass CSPR. In Section 2.3, this process is applied to three-DOF point-mass CSPRs. Natural frequencies of the equivalent linear system are obtained and a generalization of periodic trajectories is accomplished by the integration of the linear system of differential equations. Natural trajectories associated with constant stiffness of equivalent springs and without any restriction on the amplitude are obtained. A specific mechanism is introduced to demonstrate the scheme of trajectory planning. Natural trajectories are accomplished. An experimental implementation is also presented using a three-DOF prototype and a video extension is provided to demonstrate the results.

2.2 One-DOF Point-Mass CSPRs

From a free vibration point of view, a CSPR can be studied by considering an undamped mass-spring system. Indeed, each of the actuator-cable modules can be replaced with an equivalent spring with variable stiffness (k_j) and with zero free length. Therefore the complete system can be replaced with an end-effector suspended by springs with extension dependent stiffness. The stiffness is due to the variation of the forces in cables, which are produced by the control of the actuators. A one-DOF CSPR and its corresponding mass-spring system are demonstrated in Fig. 2.1. It is important to point out that the springs are not used to model the cables (which are inelastic) but rather to define a virtual system that is used to study feasible trajectories. Indeed, the tension in the springs is always positive for free vibrating natural motions.

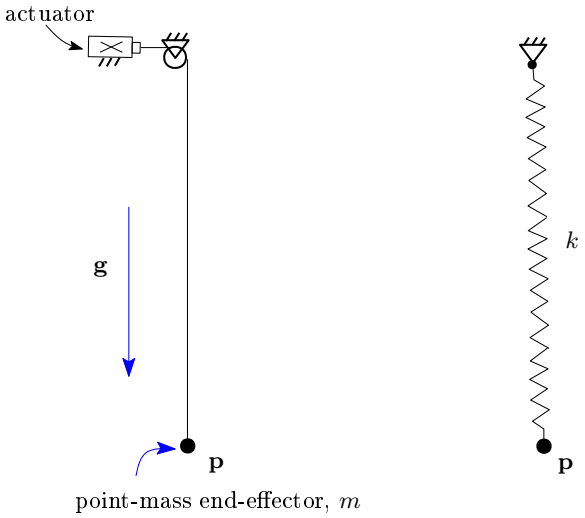

Figure 2.1 – One-DOF CSPR with point-mass and its virtual corresponding mass-spring system.

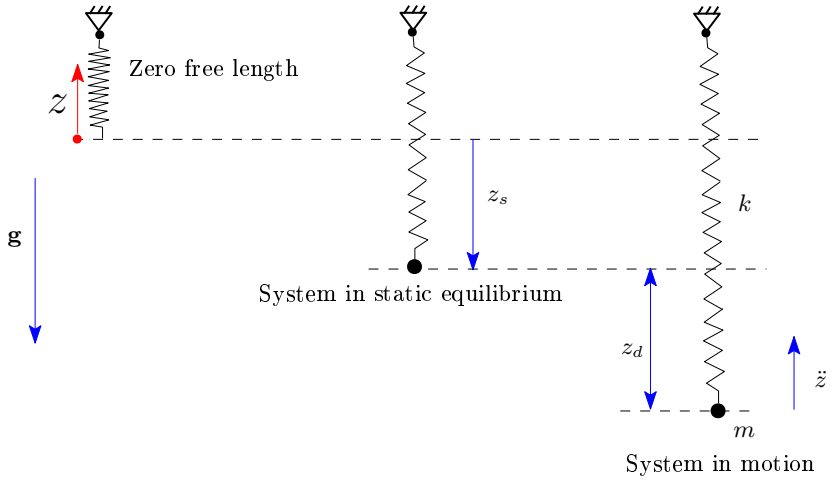

Figure 2.2 – System in motion.

When the cable-actuator unit of the robot is replaced with a linear extension spring of constant stiffness k, the system becomes linear. The process of determining natural frequencies and response of the linear system are recalled. From the diagram of Fig. 2.2, Newton's second law gives

$$m\ddot{z} = -k(z_s + z_d) - mg.$$

At the static equilibrium position, the sum of the forces is zero, so that

$$-kz_s - mg = 0,$$

which yields

$$k = -mg/z_s. \tag{2.1}$$

Thus, it is observed that the pair of forces $-kz_s$ and mg on the right-hand side of the motion equation cancel, giving

$$m\ddot{z}_d + kz_d = 0, \tag{2.2}$$

which is the differential equation of motion of this equivalent system when a coordinate frame with its origin at the equilibrium position is used. Then, natural frequencies are obtained

$$\omega_n = \sqrt{\frac{k}{m}} = \sqrt{\frac{g}{-z_s}}. \tag{2.3}$$

It can be observed from (2.3) that the natural frequency of the linear system can be obtained when the static equilibrium position z_s is given. Besides, the response/motion of the system can be readily obtained which is a set of periodic trajectories, namely,

$$z = z_s + z_d, \quad z_d = \mu_c \cos \omega_n t + \mu_s \sin \omega_n t, \tag{2.4}$$

where constant parameters μ_c and μ_s are determined from knowledge of the initial displacement of z and initial velocity $\dot{z}$ of the mass.

Clearly, if a natural free motion of the virtual system with a spring can be found, the same motion is necessarily feasible by the robot with positive tensions in the cables.

2.3 Three-DOF Spatial Point-Mass CSPRs

The process proposed for the one-DOF point-mass CSPRs is now applied to three-DOF spatial point-mass robots which can be modeled as a linear system of three mass-springs that exhibits 3D undamped harmonic oscillation if the spring stiffnesses are constant. The vibration model of a passive equivalent system of the robot is first derived. Natural frequencies and natural trajectories without any theoretical bounds on amplitudes are obtained from the integration of the linear dynamic differential equations. For a specific architecture, natural trajectories are implemented.

2.3.1 Vibration Model of a Passive Equivalent System

A spatial three-DOF CSPR with three cables and a point mass end-effector is considered here, as illustrated in Fig. 2.3. The symbols are denoted in the introduction of the thesis, unless specified otherwise. Below, indices j should be assumed to go from 1 to 3 and a plural form of an item h_j is denoted $\{h_j\}_1^3$.

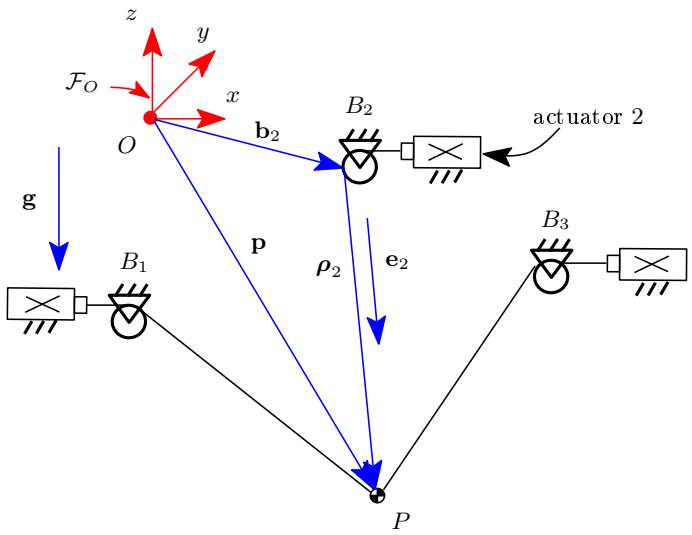

Figure 2.3 – Spatial three-dof cable-suspended robot with point-mass.

A fixed reference frame $\mathcal{F}_O$ with origin O is defined on the base of the robot, as illustrated in Fig. 2.3. The z axis of the fixed reference frame points upwards, opposite to the direction of gravity. The inverse kinematic equations can be written as

$$\boldsymbol{\rho}_j = \mathbf{p} - \mathbf{b}_j,$$

and the effective cable length ρ_j is given by

$$\rho_j = \sqrt{(\mathbf{p} - \mathbf{b}_j)^T(\mathbf{p} - \mathbf{b}_j)}.$$

Finally, $\mathbf{e}_j = \boldsymbol{\rho}_j/\rho_j$ is oriented from B_j to the end-effector.

The dynamic model is built by considering the force balance on the point-mass end-effector, which yields

$$\sum_{j=1}^{3} \left(\frac{-f_j}{\rho_j} \boldsymbol{\rho}_j \right) + m\mathbf{g} = m\ddot{\mathbf{p}}. \tag{2.5}$$

A virtual equivalent mass-spring system of a three-DOF spatial point-mass robot is illustrated in Fig. 2.4. Referring to the principle used in (2.5), the dynamic equations of the passive system

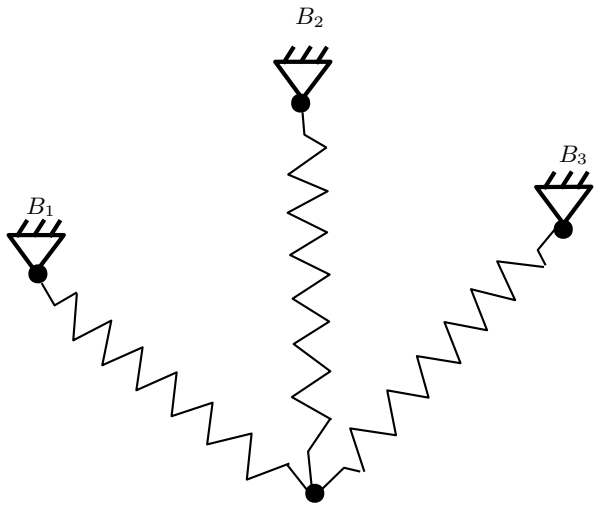

Figure 2.4 – A virtual equivalent mass-spring system.

of Fig. 2.4 can be written as

$$\begin{aligned} m\ddot{\mathbf{p}} &= \mathbf{f}_{res} + m\mathbf{g} \\ &= -\sum_{j=1}^{3} k_j(\mathbf{p} - \mathbf{b}_j) + m\mathbf{g}, \end{aligned} \tag{2.6}$$

where $\mathbf{f}_{res}$ is the resultant cable force, $k_j = f_j/\rho_j$ is the stiffness of the jth equivalent spring with zero free length. For feasible trajectories during which cables are taut, the $\{k_j\}_1^3$ are non-negative since they represent ratios between cable tensions and cable lengths.

2.3.2 Natural Frequencies and Natural Trajectories

The cable-actuator units of the robot are replaced with linear extension springs of constant stiffness k_j and with zero free length. By analyzing this passive system, natural frequencies and the corresponding free motions can be determined. These natural trajectories have no theoretical bounds on the amplitude and the resultant cable tension always points toward a fixed point. If such motions are then reproduced by the actuated robot, it can be guaranteed that the cable tensions will be positive at all times because the spring forces of the passive free vibrating system are positive at all times.

When the passive system of Fig. 2.4 is in static equilibrium, (2.6) can be written at the equilibrium positions

$$\mathbf{w} + m\mathbf{g} = K\mathbf{p}_s, \tag{2.7}$$

where $\mathbf{p}_s$ stands for the position of the static equilibrium state, the constant force vector $\mathbf{w}$

represents

$$\mathbf{w} = \sum_{j=1}^{3} k_j \mathbf{b}_j, \tag{2.8}$$

and the constant total stiffness K represents

$$K = \sum_{j=1}^{3} k_j. \tag{2.9}$$

Substituting (2.7), (2.8) and (2.9) into (2.6) then yields the following linear differential equations with constant coefficients

$$m\ddot{\mathbf{p}}_d + K\mathbf{p}_d = \mathbf{0} \tag{2.10}$$

where $\mathbf{p}_d = \mathbf{p} - \mathbf{p}_s$, i.e., $\mathbf{p}_d$ represents the displacement from the equilibrium position. Therefore, the natural frequency and the response/motion of the system can be obtained. The characteristic equation of each scalar linear equation in (2.10) has two complex roots and therefore solutions from the integration of the differential equations are of the following form

$$\mathbf{p} = \mathbf{p}_d + \mathbf{p}_s \tag{2.11}$$

where $\mathbf{p}_s = [x_s, y_s, z_s]^T$ can be determined from the conditions for the static equilibrium position, namely (2.7) and (2.9) in the form of $\{k_j\}_1^3$, $\mathbf{p}_d$ is

$$\mathbf{p}_d = \mathbf{c}\cos\omega_n t + \mathbf{s}\sin\omega_n t, \tag{2.12}$$

where the natural frequency, ω_n, is

$$\omega_n = \sqrt{\frac{K}{m}} \tag{2.13}$$

and $\mathbf{c} = [\mu_{xc}, \mu_{yc}, \mu_{zc}]^T$, $\mathbf{s} = [\mu_{xs}, \mu_{ys}, \mu_{zs}]^T$. The parameters $\mathbf{c}$ and $\mathbf{s}$ can be any values which are set as desired to determine the shape of the motion. Therefore, oscillation in different directions can be used to produce linear, circular, and elliptical trajectories.

If the cable attachment points $\{B_j\}_1^3$ are in a plane at the same height and the origin of fixed frame $\mathcal{F}_O$ lies in this plane, the z-component of each vector $\mathbf{b}_j$ is zero. Combining with (2.8) and (2.9), the last row of (2.7) can then be written as

$$K = \frac{-mg}{z_s}, \tag{2.14}$$

and the natural frequency is determined as

$$\omega_n = \sqrt{\frac{-g}{z_s}} \tag{2.15}$$

where $z_s < 0$ is the central static equilibrium position on the z axis, and constant. Since *unbounded* parameters μ_{zc} and μ_{zs} determine the amplitude of the motion, it implies that the end-effector can go *above* the cable attachment points $\{B_j\}_1^3$.

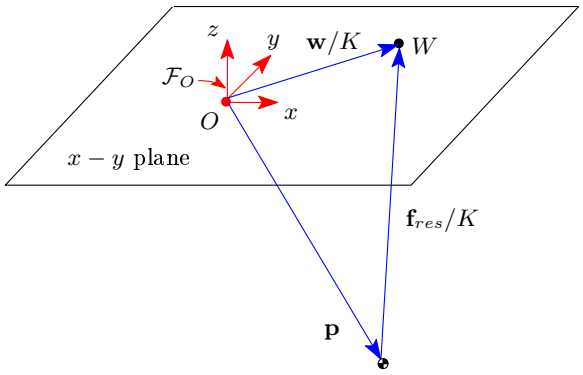

Figure 2.5 – Resultant cable force $\mathbf{f}_{res}$ points toward W, which is located in the $x-y$ plane.

In practice, trajectories that extend above $\{B_j\}_1^3$ impose many significant restrictions on CSPR design. Therefore, only trajectories for which $z < 0$ are considered below, thus ensuring that the mechanism remains *suspended*. Trajectories above $\{B_j\}_1^3$ were achieved in (Zhang and Shang, 2016; Zhang et al., 2017) for a point-mass CSPR.

Under this assumption, the linearized version of (2.6) describes an undamped harmonic oscillator, with the resultant cable force defined by combining (2.8) and (2.9) to obtain

$$\begin{aligned}\mathbf{f}_{res} &= -\sum_{j=1}^{3} k_j(\mathbf{p}-\mathbf{b}_j)\\ &= -K\mathbf{p}+\mathbf{w}.\end{aligned}$$

This force always points toward the fixed point W, which is the point in the $x-y$ plane located at the tip of vector $\mathbf{w}/K$, as shown in Fig. 2.5. In particular, if $\mathbf{w}=\mathbf{0}$, $\mathbf{f}_{res}$ points in the direction opposite to vector $\mathbf{p}$, i.e., from P toward O. Therefore, during the natural trajectories (2.11), the resultant cable tension always points toward a fixed point.

2.3.3 Experimental Validation

A specific architecture given in Fig. 2.3 with its origin located at the centroid of the base attachment points, $\{B_j\}_1^3$, is applied to verify the scheme of the trajectory planning. The distance between the cable attachment points on the frame is $a = 1.2\,\text{m}$ and the mass of the end-effector is $m = 0.129\,\text{kg}$. Three servo-controlled winches are used to control the length of the cables. A series of trajectories designed in the preceding sections is demonstrated in a multimedia extension.

The points $\{B_j\}_1^3$ form an equilateral triangle with circumradius $R = a/\sqrt{3}$ and are located at the same height, i.e., in a horizontal plane. The vectors $\{\mathbf{b}_j\}_1^3$ are

$$\mathbf{b}_j = R\,[\cos\theta_j, \sin\theta_j, 0]^T, \quad \theta_j = \frac{2\pi(j-1)}{3}. \tag{2.16}$$

Numerical values for these vectors are provided in Table 2.1.

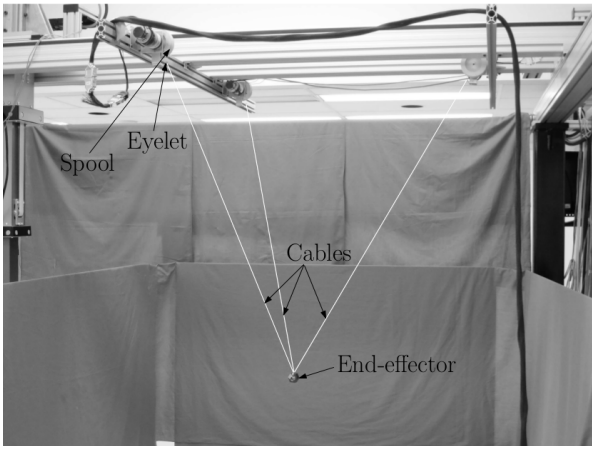

Figure 2.6 – Prototype of a three-DOF point-mass CSPR.

Table 2.1 – Cable attachment point vectors for the base.

j	$\mathbf{b}_j^T$ [m]			
1	[	0.693	0.0	0]
2	[	-0.346	0.6	0]
3	[	-0.346	-0.6	0]

Substituting (2.16) into the first two rows of (2.7), one obtains two linear equations in the $\{k_j\}_1^3$. Combining these two equations with (2.9), the $\{k_j\}_1^3$ can be obtained, namely

$$\begin{aligned} k_1 &= \frac{m\omega_n^2}{3R}(2x_s + R) > 0, \\ k_2 &= \frac{m\omega_n^2}{3R}(R - x_s + \sqrt{3}y_s) > 0, \\ k_3 &= \frac{m\omega_n^2}{3R}(R - x_s - \sqrt{3}y_s) > 0. \end{aligned} \tag{2.17}$$

From the above expressions, it is observed that the $\{k_j\}_1^3$ are constant and that they can be calculated when x_s and y_s are given. Also they provide conditions to keep the $\{k_j\}_1^3$ constant and positive. These conditions define a region that is exactly the static workspace of the robot (Riechel and Ebert-Uphoff, 2004). Moreover, when trajectories of the real robot are designed as in (2.11) with parameters $\mathbf{p}_s$ located in the static workspace, it can be guaranteed that the tensions in the cables will remain positive because the tensions in the springs of the corresponding free-vibrating system are always positive and the two sets of tensions are dynamically equivalent.

Furthermore, it should be pointed out here that $\mathbf{c}$ and $\mathbf{s}$ in (2.12), which refer to desired motion shape, can be chosen arbitrarily (they are not bounded) which thereby reveals that the dynamic workspace of the robot is not bounded. Examples are shown in (Gosselin, 2013) where

simple harmonic trajectories are designed, including vertical oscillations, circular trajectories in horizontal and vertical planes. When natural frequencies (referred to as special frequencies in (Gosselin, 2013)) are applied, the cable tensions are always positive for any amplitude of motion. The above derivation provides a mathematical explanation of the remarkable phenomenon observed in (Gosselin, 2013), namely that during the whole trajectories operating with natural frequencies, the nonlinear dynamic system is in fact linear. Also, results obtained in this chapter generalize the trajectories. Indeed, according to (2.11), more trajectories can be generated by properly selecting the parameters.

In order to validate the trajectory planning scheme proposed, examples of periodic trajectories are developed according to (2.11) for the robot whose parameters are given in Table 2.1.

Horizontal Line

A horizontal line with the parameters chosen in (2.11) as $\mathbf{p}_s = [0, 0, z_s]^T$, $\mathbf{c} = [0, 0, 0]^T$, and $\mathbf{s} = [\mu_{xs}, 0, 0]^T$, is represented as

$$x = \mu_{xs} \sin \omega_n t, \quad y = 0, \quad z = z_s,$$

where μ_{xs} is one half of the total horizontal range of motion, z_s is the position of the horizontal trajectory with respect to the z axis, ω_n is the natural frequency of the periodic motion and t is the time. When $\mu_{xs} = 0.8$ m, $z_s = -1.2$ m, the frequency is therefore $\omega_n = \sqrt{-g/z_s} = 2.8592$ rad/s, $k_1 = k_2 = k_3 = 0.3515$ N/m. The cable tensions remain positive and continuous along the entire trajectory, as illustrated in Fig. 2.7.

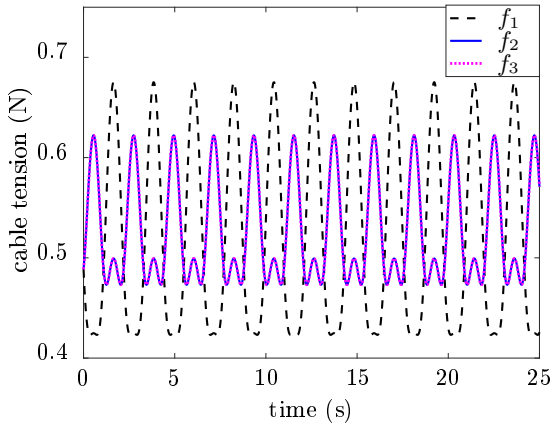

Figure 2.7 – Cable tension for the horizontal line trajectory.

Horizontal Circle

A horizontal circle, centred on the static equilibrium point $(0, 0, z_s)$ lying on the z axis, is designed by choosing the parameters in (2.11) with $\mathbf{p}_s = [0, 0, z_s]^T$, $\mathbf{c} = [\mu, 0, 0]^T$, and $\mathbf{s} = [0, \mu, 0]^T$, which is

$$x = \mu \cos \omega_n t, \quad y = \mu \sin \omega_n t, \quad z = z_s,$$

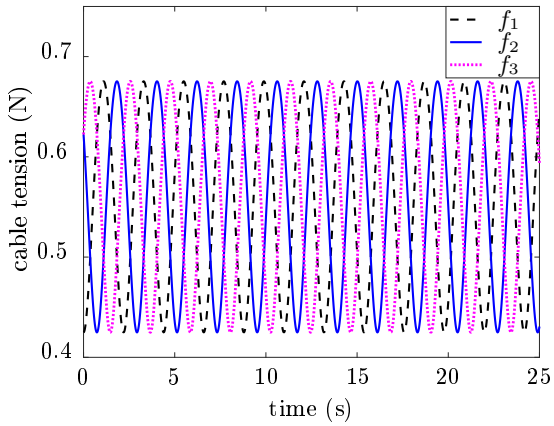

Figure 2.8 – Cable tension for the horizontal circle trajectory.

where μ is the radius of the circle, z_s is the position of the horizontal trajectory with respect to the z axis, ω_n is the natural frequency of the periodic motion and t is the time. When $\mu = 0.8$ m, $z_s = -1.2$ m, the frequency is therefore $\omega_n = \sqrt{-g/z_s} = 2.8592$ rad/s, $k_1 = k_2 = k_3 = 0.3515$ N/m. The $\{k_j\}_1^3$ are the same as those during the horizontal line since they are only related to $\mathbf{p}_s$. This circular trajectory is verified to be feasible with all the three cables in tension as illustrated in Fig. 2.8.

Ellipse with Elevation on the z Axis

An ellipse with elevation on z axis, shown in Fig. 2.9, is designed with the parameters in (2.11) yielding $\mathbf{p}_s = [0, 0, z_s]^T$, $\mathbf{c} = [\mu_{xc}, 0, 0]^T$, and $\mathbf{s} = [0, \mu_{ys}, \mu_{zs}]^T$, which is represented as

$$x = \mu_{xc} \cos \omega_n t, \quad y = \mu_{ys} \sin \omega_n t, \quad z = z_s + \mu_{zs} \sin \omega_n t,$$

where z_s is the position of the horizontal trajectory with respect to the z axis, ω_n is the frequency of the periodic motion and t is the time, μ_{xc}, μ_{ys} and μ_{zs} are the amplitude of oscillations on the x, y and z axes, respectively. When $\mu_{xc} = 0.9$ m, $\mu_{ys} = 0.4$ m, $\mu_{zs} = 0.6$ m,

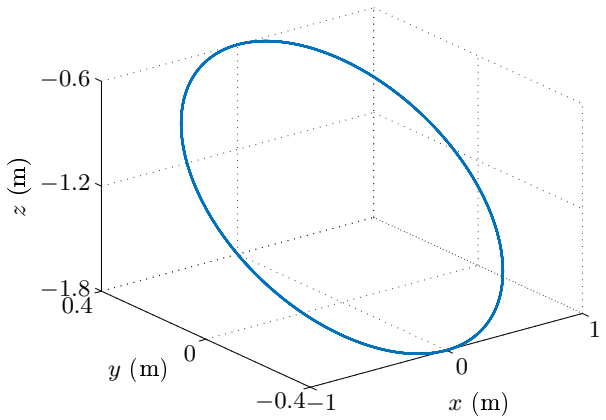

Figure 2.9 – Illustration of the ellipse trajectory with elevation on z axis.

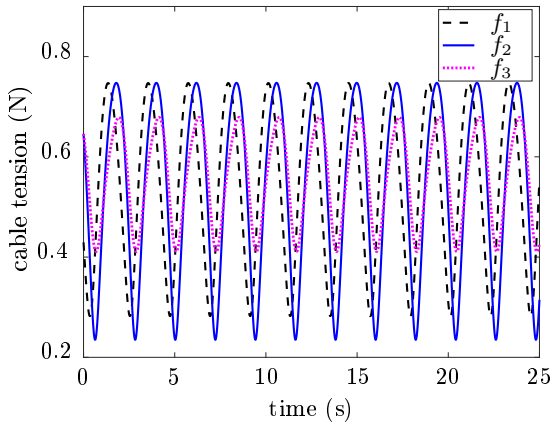

Figure 2.10 – Cable tension for the ellipse trajectory with elevation on z axis.

$z_s = -1.2$ m, the frequency is therefore $\omega_n = \sqrt{-g/z_s} = 2.8592$ rad/s, $k_1 = k_2 = k_3 = 0.3515$ N/m. Again, cable tensions illustrated in Fig. 2.10 are positive, which verifies that this ellipse trajectory is feasible.

2.4 Conclusion

This chapter addresses a method for the synthesis of dynamic periodic trajectory generation for CSPRs with point mass. Based on the dynamics of the robot, natural frequencies of a passive mechanical system obtained by replacing the actuator-cable units with linear springs are first obtained. Natural periodic trajectories are derived by the integration of the linear dynamic equations. These trajectories have no theoretical bounds for the amplitude. A specific architecture is introduced and example trajectories are performed. An experimental validation of the trajectories is also demonstrated in the accompanying video.

2.5 Supplementary Data

Extension1-chapter2-periodic-3DOF.mp4—The supplementary video file shows the experimental prototype following several trajectories, including a horizontal linear trajectory, a horizontal circular trajectory, and an ellipse with elevation on the z axis.

Chapter 3

Dynamic Periodic Trajectory Planning of Three-DOF Planar CSPRs

3.1 Introduction

The concept of equivalent passive mechanical system developed in the preceding chapter is general and is used in the periodic trajectory planning of three-DOF planar CSPRs. The cable-actuator units of the robot are replaced with linear extension springs of constant stiffness and with zero free length. This allows the transformation of the dynamic equations into linear differential equations with constant coefficients for the positioning part, while the orientation equation becomes a pendulum-like differential equation for which accurate solutions can be found in the literature. The integration of the differential equations is shown to yield families of translational trajectories and natural frequencies. Combining the results obtained with translational trajectories and rotational trajectories, natural trajectories including pure translation motions and motions including translation and variable rotations are generated.

Because of the initial equivalence of the passive system on which the proposed method is based, the stiffness of the equivalent spring is constant and hence always positive, which ensures that all cables remain under tension. In Section 3.2, the kinematic and dynamic models of the mechanism are presented and the vibration model of an equivalent passive system is introduced as a tool to help analyze the mechanism. Section 3.3 introduces the conditions that define natural trajectories associated with constant-stiffness equivalent springs. In Section 3.4, the trajectories obtained in Section 3.3 are applied to a specific robot architecture.

3.2 Mechanics of Three-DOF Planar CSPRs

In this section, the equations that govern the kinematics and dynamics of three-DOF Planar CSPRs are first formulated. Then, the dynamic equations of an equivalent freely vibrating

undamped system are derived. Finally, the differential equations of motion of this equivalent system are developed.

3.2.1 Robot Architecture

A general planar three-DOF CSPR is represented schematically in Fig. 3.1, with the symbols denoted in the introduction of the thesis, unless specified otherwise. It consists of a moving platform to which three cables are attached. These cables can generate moments with respect to the centre of mass of the platform and thereby provide rotation. At the other end, the cables are connected to and driven by three actuated spools mounted on a fixed frame. The robot has three actuators and three degrees of freedom and is therefore fully actuated. By controlling the extension of the cables, the position and the orientation of the platform can be controlled. Below, indices j should be assumed to go from 1 to 3 and a plural form of an item h_j is denoted $\{h_j\}_1^3$.

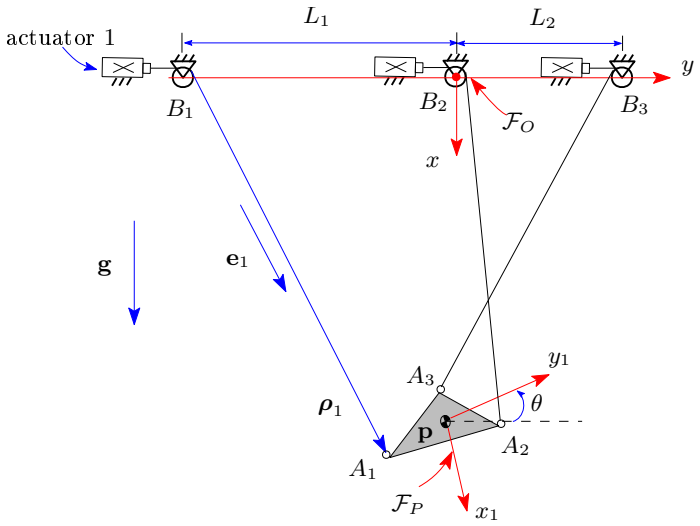

Figure 3.1 – Schematic diagram of a general planar three-DOF CSPR.

3.2.2 Kinematic and Dynamic Modelling

As shown in Fig. 3.1, the fixed frame $\mathcal{F}_O$ is defined on the base of the robot. The origin of the coordinates O coincides with the spool output point B_2. The y axis is defined along the straight line connecting the spools $\{B_j\}_1^3$ which are located at the same height. Therefore, the y axis is horizontal and the x axis is vertical pointing downwards. Then, vectors $\{\mathbf{b}_j\}_1^3$ can be expressed as

$$\mathbf{b_1} = [0, -L_1]^T, \quad \mathbf{b_2} = [0, 0]^T, \quad \mathbf{b_3} = [0, L_2]^T. \tag{3.1}$$

A moving reference frame $\mathcal{F}_P$ is located on the platform. The origin of the coordinates P is located at the centre of mass of the end-effector. The x_1 axis is perpendicular to the line of

two attachments A_1A_2 and is pointing downwards while the y_1 axis is orthogonal to the x_1 axis as shown in Fig. 3.1. Then, vectors $\{\mathbf{a}_j\}_1^3$ are

$$\mathbf{a}_1 = [n_1, l_1]^T, \quad \mathbf{a}_2 = [n_1, l_2]^T, \quad \mathbf{a_3} = [n_2, l_3]^T. \tag{3.2}$$

The orientation of the platform is noted θ, the angle measured from the y axis to the y_1 axis. It is assumed that the platform can become vertical with respect to the fixed frame but that it cannot flip, namely

$$-\frac{\pi}{2} \leq \theta \leq \frac{\pi}{2}. \tag{3.3}$$

Moreover, it is assumed that the platform operates below the base attachment points $\{B_j\}_1^3$, i.e., that it remains *suspended*.

The inverse kinematics can be written as

$$\boldsymbol{\rho}_j = \mathbf{p} + \mathbf{Q}\mathbf{a}_j - \mathbf{b}_j.$$

Then, the dynamic model is built using the Newton-Euler approach which yields

$$\sum_{j=1}^{3} \left(\frac{-f_j}{\rho_j} \boldsymbol{\rho}_j \right) + m\mathbf{g} = m\ddot{\mathbf{p}}, \tag{3.4}$$

$$\sum_{j=1}^{3} (\mathbf{Q}\mathbf{a}_j)^T \mathbf{E} \left(\frac{f_j}{\rho_j} \boldsymbol{\rho}_j \right) = I\ddot{\theta}, \tag{3.5}$$

where

$$\mathbf{E} = \begin{bmatrix} 0 & -1 \\ 1 & 0 \end{bmatrix},$$

I is the moment of inertia of the platform with respect to its centre of mass, and $\ddot{\theta}$ is the angular acceleration of the platform.

Equations (3.4) and (3.5) can be written in matrix form as

$$\mathbf{M}\mathbf{k} = \boldsymbol{\gamma}, \tag{3.6}$$

where

$$\boldsymbol{\gamma} = \begin{bmatrix} m(\mathbf{g} - \ddot{\mathbf{p}}) \\ I\ddot{\boldsymbol{\theta}} \end{bmatrix},$$

$$\mathbf{k} = \begin{bmatrix} k_1 & k_2 & k_3 \end{bmatrix}^T, \quad k_j = \tfrac{f_j}{\rho_j} > 0$$

and

$$\mathbf{M} = \begin{bmatrix} \boldsymbol{\rho}_1 & \boldsymbol{\rho}_2 & \boldsymbol{\rho}_3 \\ (\mathbf{Q}\mathbf{a}_1)^T \mathbf{E}\boldsymbol{\rho}_1 & (\mathbf{Q}\mathbf{a}_2)^T \mathbf{E}\boldsymbol{\rho}_2 & (\mathbf{Q}\mathbf{a}_3)^T \mathbf{E}\boldsymbol{\rho}_3 \end{bmatrix}.$$

The vector of actual cable tension $\mathbf{f}$ is then written as

$$\mathbf{f} = \begin{bmatrix} k_1\rho_1 & k_2\rho_2 & k_3\rho_3 \end{bmatrix}^T. \tag{3.7}$$

3.2.3 Vibration Model of a Passive Equivalent System

From a free vibration point of view, a planar three-DOF CSPR can be replaced by an undamped mass-spring system, as illustrated in Fig. 3.2. Referring to the principle used in (3.4) and (3.5), the dynamic equations of the system of Fig. 3.2 can be rewritten in the following form

$$\begin{aligned} m\ddot{\mathbf{p}} &= \mathbf{f}_{res} + m\mathbf{g} \\ &= -\sum_{j=1}^{3} k_j \left(\mathbf{p} + \mathbf{Q}\mathbf{a}_j - \mathbf{b}_j\right) + m\mathbf{g}, \end{aligned} \tag{3.8}$$

and

$$I\ddot{\theta} = -\mathbf{p}^T \mathbf{E} \sum_{j=1}^{3} k_j \mathbf{Q}\mathbf{a}_j - \sum_{j=1}^{3} k_j \left(\mathbf{Q}\mathbf{a}_j\right)^T \mathbf{E}\mathbf{b}_j, \tag{3.9}$$

where $\mathbf{f}_{res}$ is the resultant cable force, $k_j = f_j/\rho_j$ is the stiffness of the jth equivalent spring with zero free length. When $\rho_j = 0$, the jth equivalent spring is at free length position. For feasible trajectories during which cables are taut, the $\{k_j\}_1^3$ are non-negative since they represent ratios between cable tensions and cable lengths. Moreover, $\sum_{j=1}^{3} k_j$ is the total stiffness of the three equivalent springs.

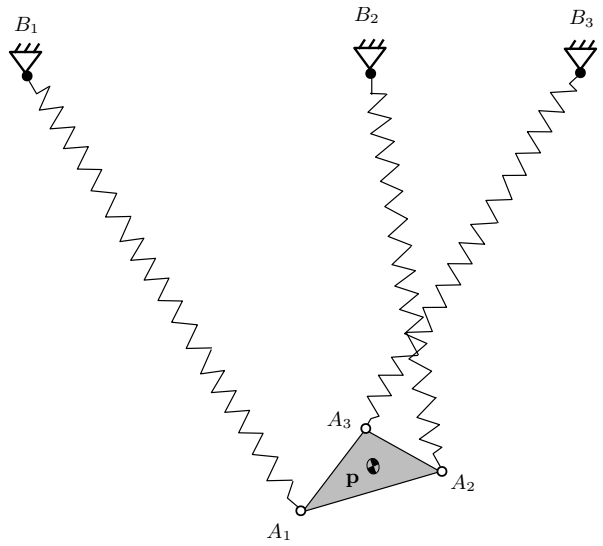

Figure 3.2 – A virtual equivalent mass-spring system of a general planar three-DOF CSPR.

It is observed that if the translational component and rotational component of the trajectories are coupled such that

$$\sum_{j=1}^{3} k_j \mathbf{Q}\mathbf{a}_j = H\mathbf{p}, \tag{3.10}$$

with H being a scalar factor, which implies that vector $\sum_{j=1}^{3} k_j \mathbf{Q}\mathbf{a}_j$ is aligned with vector $\mathbf{p}$.

Then the dynamic equations (3.8) and (3.9) can be greatly simplified, namely

$$m\ddot{\mathbf{p}} + K\mathbf{p} - \left(\sum_{j=1}^{3} k_j \mathbf{b}_j + m\mathbf{g}\right) = \mathbf{0}, \tag{3.11}$$

and

$$I\ddot{\theta} + A\cos\theta + B\sin\theta = 0, \tag{3.12}$$

where

$$K = \sum_{j=1}^{3} k_j + H, \tag{3.13}$$

$$\sum_{j=1}^{3} k_j \mathbf{b}_j + m\mathbf{g} = \begin{bmatrix} mg \\ -(k_1 L_1 - k_3 L_2) \end{bmatrix}, \tag{3.14}$$

and

$$A = k_1 n_1 L_1 - k_3 n_2 L_2, \quad B = -k_1 l_1 L_1 + k_3 l_3 L_2,$$

H is seen as the stiffness of a virtual spring, which is not associated with a particular cable but arises to respect the moment-component coupling in (3.10).

3.3 Trajectory Planning

The cable-actuator units of the robot are replaced with linear extension springs of constant stiffnesses and with zero free length. As a result, the translational component of the platform corresponds to a simple harmonic motion while its rotational component becomes a free, undamped simple pendulum. Natural frequencies arise and natural translational trajectories are integrated from the differential equations that govern the linear translational component of the trajectories. Natural rotational trajectories integrated from the rotational component of the trajectories are found in the literature. These natural trajectories have no theoretical bounds on the amplitude and the resultant cable tension assumed to be attached on the platform centre of mass always points toward a fixed point.

3.3.1 Translational Component

The translational component (3.11) is first considered. It becomes a linear differential equation with constant coefficients, namely

$$\ddot{\mathbf{p}} + \omega_n^2 \mathbf{p} - (\mathbf{v} + \mathbf{g}) = \mathbf{0}, \tag{3.15}$$

and translational trajectories can be easily obtained by integrating the differential equation (3.11), that is

$$\mathbf{p} = \mathbf{p}_s + \mathbf{p}_d, \tag{3.16}$$

where

$$\omega_n^2 = K/m, \tag{3.17}$$

$$\mathbf{v} = \mathbf{w}/m = \textstyle\sum_{j=1}^{3} k_j \mathbf{b}_j/m, \tag{3.18}$$

$$\mathbf{p}_d = \mathbf{c}\cos\omega_n t + \mathbf{s}\sin\omega_n t, \tag{3.19}$$

$$\mathbf{p}_s = \begin{bmatrix} x_s \\ y_s \end{bmatrix} = \begin{bmatrix} g/\omega_n^2 \\ -(k_1 L_1 - k_3 L_2)/\omega_n^2 \end{bmatrix}, \tag{3.20}$$

and

$$\mathbf{c} = \begin{bmatrix} \mu_{xc} & \mu_{yc} \end{bmatrix}^T, \quad \mathbf{s} = \begin{bmatrix} \mu_{xs} & \mu_{ys} \end{bmatrix}^T. \tag{3.21}$$

When vector $\mathbf{p}_s$ is chosen, the natural frequency of the linear system is determined. Indeed, the first component of (3.20) yields

$$\omega_n = \sqrt{\frac{g}{x_s}}, \tag{3.22}$$

where $x_s > 0$ is the central static equilibrium position on the x axis, and constant. Since *unbounded* parameters μ_{xc} and μ_{xs} determine the amplitude of the motion, it implies that the end-effector can go *above* the cable attachment points $\{B_j\}_1^3$. In fact, for the three-DOF planar mechanism considered herein, such trajectories are not possible as they would result in cable interference. Therefore, only trajectories for which $x > 0$ are considered below, ensuring that the mechanism remains *suspended*.

Moreover, the linearized version of the translational component (3.15) describes an undamped harmonic oscillator, with the resultant cable force defined as

$$\begin{aligned} \mathbf{f}_{res} &= -\sum_{j=1}^{3} k_j \left(\mathbf{p} + \mathbf{Q}\mathbf{a}_j - \mathbf{b}_j\right) \\ &= -\left(\sum_{j=1}^{3} k_j + H\right)\mathbf{p} + \sum_{j=1}^{3} k_j \mathbf{b}_j \\ &= -K\mathbf{p} + \mathbf{w}. \end{aligned}$$

This force assumed to be attached on the platform centre of mass always points to the fixed point W, which is the point on the y axis located at the tip of vector $\mathbf{w}/K$, as shown in Fig. 3.3. In particular, if $\mathbf{w} = \mathbf{0}$, $\mathbf{f}_{res}$ points in the direction opposite to vector $\mathbf{p}$, i.e., from P toward O. Therefore, during the natural trajectories (3.16), the resultant cable tension always points toward a fixed point.

3.3.2 Rotational Component

Consider now the rotational component (3.12). It can be transformed into the dynamic equation of a free, undamped simple pendulum when A and B are constant since the cosine and

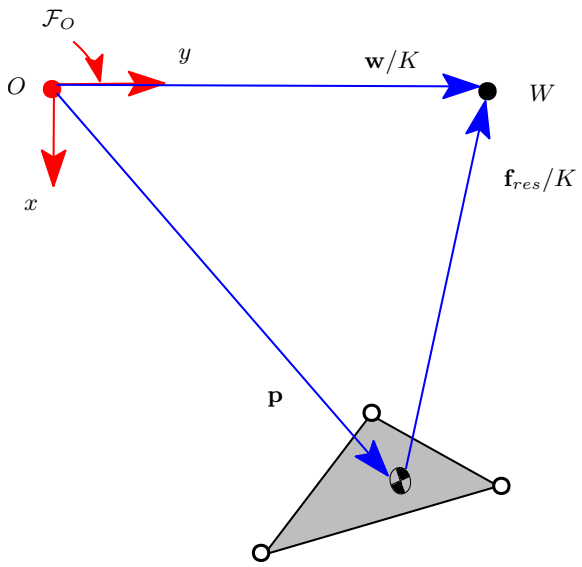

Figure 3.3 – Resultant cable force $\mathbf{f}_{res}$ points toward W, which is located on the y axis.

sine functions can be combined to be one sine function, as

$$\ddot{\Theta} + \omega_1^2 \sin\Theta = 0, \tag{3.23}$$

where

$$\omega_1^2 = \frac{\sqrt{A^2 + B^2}}{I} \tag{3.24}$$

and $\Theta = \theta + \delta$ with constant $\delta = \text{atan2}(A, B)$. As long as Θ is determined, the rotation angle θ can be obtained.

For small values of the oscillation amplitude, it is possible to linearise the rotational component dynamic equation (3.23)

$$\ddot{\Theta} + \omega_1^2 \Theta = 0.$$

This simple harmonic equation can be easily solved as

$$\Theta = \Theta_0 \sin\omega_1 t,$$

where Θ_0 is the amplitude of the oscillations and ω_1 is the frequency.

However, when the angular displacement amplitude is large enough ($0 \leq \Theta_0 \leq \pi/2$), the equation of motion must remain in its nonlinear form. Exact solutions for the nonlinear differential equation have been obtained in (Davis, 1962) with the following initial conditions $\Theta(0) = 0$, $\dot{\Theta}(0) \neq 0$ as

$$\Theta = 2\arcsin\left[\sin\frac{\Theta_0}{2}\text{sn}\left(\omega_1 t, \sin^2\frac{\Theta_0}{2}\right)\right], \tag{3.25}$$

and also in (Beléndez et al., 2007) for a platform rotating from $\Theta(0) = \Theta_0$, $\dot{\Theta}(0) = 0$ as

$$\Theta = 2\arcsin\left[\sin\frac{\Theta_0}{2}\text{sn}\left(\mathcal{K}\left(\sin^2\frac{\Theta_0}{2}\right) - \omega_1 t, \sin^2\frac{\Theta_0}{2}\right)\right], \tag{3.26}$$

where sn represents one of Jacobi's elliptic functions which are inverses of the incomplete elliptic integral of the first kind.

The corresponding oscillation frequency is obtained as (Davis, 1962; Beléndez et al., 2007; Marion, 2013; Veronesi, 1971)

$$\omega_r = \omega_1 \frac{\pi}{2\mathcal{K}\left(\sin^2 \frac{\Theta_0}{2}\right)}, \tag{3.27}$$

where $\mathcal{K}\left(\sin^2 \frac{\Theta_0}{2}\right)$ is the complete elliptic integral of the first kind, that is

$$\mathcal{K}\left(\sin^2 \frac{\Theta_0}{2}\right) = \int_0^{\pi/2} \frac{\mathrm{d}\Theta}{\sqrt{1 - \sin^2 \frac{\Theta_0}{2} \sin^2 \Theta}}.$$

Therefore, for a specific architecture and trajectories which satisfy the coupling condition of translation and rotation given in (3.10), constant $\{k_j\}_1^3$ and H can be determined when the vector $\mathbf{p}_s$ and the rotational frequency of the platform ω_r are given.

3.4 Examples

In order to demonstrate the proposed trajectory planning scheme, a specific architecture is used. Natural trajectories are designed, during which

$$\sum_{j=1}^{3} k_j \mathbf{Q}\mathbf{a}_j = \mathbf{Q} \sum_{j=1}^{3} k_j \mathbf{a}_j = \mathbf{0},$$

namely, parameter $H = 0$ according to (3.10) and

$$\begin{bmatrix} \mathbf{a}_1 & \mathbf{a}_2 & \mathbf{a}_3 \end{bmatrix} \begin{bmatrix} k_1 \\ k_2 \\ k_3 \end{bmatrix} = \begin{bmatrix} 0 \\ 0 \end{bmatrix}. \tag{3.28}$$

The latter equation implies that the polygon connecting the attachment points on the platform includes the centre of mass since all $\{k_j\}_1^3$ must be positive. Moreover, conditions that can yield these motions are obtained and used to determine cable tensions. Example trajectories are demonstrated in the following for a specific architecture.

3.4.1 Specific Architecture

A specific architecture shown in Fig. 3.4 is used. Two of the cables are attached to the ends of the platform with $\mathbf{a}_1 = -\mathbf{a}_2$. The third cable is attached at the centre of mass of the platform, that is $\mathbf{a}_3 = \mathbf{0}$. Therefore, according to (3.28), one has

$$k_1 = k_2. \tag{3.29}$$

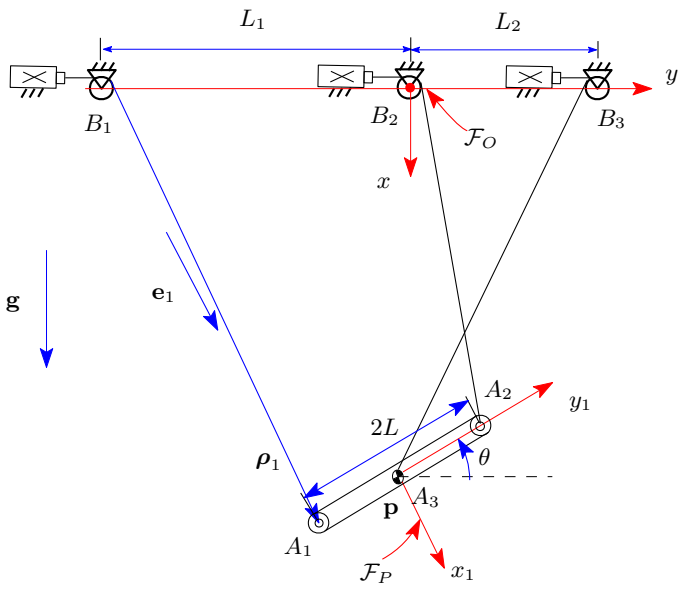

Figure 3.4 – Schematic diagram of a specific planar three-DOF cable-suspended robot.

Referring to the specific architecture, the rotational component of the dynamic equation (3.23) becomes, with $\delta = 0$ and $\Theta = \theta$,

$$\ddot{\theta} + \omega_1^2 \sin\theta = 0, \tag{3.30}$$

where

$$\omega_1^2 = \frac{k_1 L L_1}{I} \tag{3.31}$$

with k_1 a positive constant.

The substitution of (3.17) and (3.29) into the second row of (3.20) then leads to

$$k_3 = \frac{2y_s + L_1}{L_2 - y_s} k_1 > 0, \tag{3.32}$$

which yields

$$-L_1/2 < y_s < L_2. \tag{3.33}$$

Moreover, from (3.22), it is clear that one must have

$$x_s > 0. \tag{3.34}$$

Equations (3.33) and (3.34) define the feasible range of values for x_s and y_s for the natural periodic trajectories studied here.

Therefore, any trajectory satisfying the solution given in (3.25), (3.26) and (3.16) as well as the constraints for $\mathbf{p}_s$ given in (3.33) and (3.34) is guaranteed to correspond to positive tensions, throughout the trajectory. Several families of periodic translational trajectories designed in the form of (3.16) can be produced as long as the $\{k_j\}_1^3$ are positive. Vectors $\mathbf{c}$ and $\mathbf{s}$ can be chosen to be desired shape of motions.

Then, $\{k_j\}_1^3$ can be determined from the corresponding conditions that can yield the natural trajectories. Substituting (3.32) into (3.17) and solving for k_1, one then obtains an expression of k_1 as a function of the motion frequency, namely

$$k_1 = \frac{L_2 - y_s}{2L_2 + L_1}\omega_n^2. \tag{3.35}$$

Using (3.22), the latter equation can also be written as

$$k_1 = \frac{(L_2 - y_s)g}{(2L_2 + L_1)x_s}. \tag{3.36}$$

Finally, the orientation part of the trajectory can be planned. To this end, (3.35) and (3.31) are substituted into (3.27), which yields

$$\omega_r^2 = J\omega_n^2, \tag{3.37}$$

with

$$J = \frac{(L_2 - y_s)\, LL_1\pi^2}{(2L_2 + L_1)\, 4I\mathcal{K}^2 \left(\sin^2 \frac{\theta_0}{2}\right)}. \tag{3.38}$$

When $\mathbf{p}_s$ is given, J becomes a function of θ_0 and parameters of the mechanism. For a certain mechanism and a chosen value of J, θ_0 can be determined using (3.38). Choosing a value of J corresponds to determining the ratio between the frequency of the translational component and the rotational component. Alternatively, one can select a value of θ_0 (the amplitude of the rotational motion) and determine J using (3.38). Once ω_r has been determined, the trajectory can be planned as written in (3.25) and (3.26).

It is pointed out that trajectories that can be written in the form of (3.16), (3.25) and (3.26) possess $k_1 = k_2$ as a positive definite constant and k_3 as constant for the architecture shown in Fig. 3.1. $k_3 > 0$ can be satisfied and guaranteed by choosing certain y_s as shown in (3.33). Moreover, for pure translation with $\theta = 0$, (3.30) is easily satisfied.

3.4.2 Example Trajectories

Trajectories with $\mathbf{p}_s = [x_s, 0]^T$ that translate and rotate with the same frequency are taken as an example in the following, that is $J = 1$. As mentioned above, $k_1 = k_2$ is positive and constant, and k_3 is constant. Additionally, since $y_s = 0$ is within the interval given in (3.33), $k_3 > 0$ is also guaranteed. Although in the case of pure rotation, the rotational frequency ω_r can be any positive value, ω_r is chosen to be equal to the translational frequency given in (3.22).

Substituting $I = 1/12mL^2$ and $y_s = 0$ into (3.38), one then has

$$J = \frac{3\pi^2}{m\,(2L/L_1 + L/L_2)\, K^2 \left(\sin^2 \frac{\theta_0}{2}\right)} = 1. \tag{3.39}$$

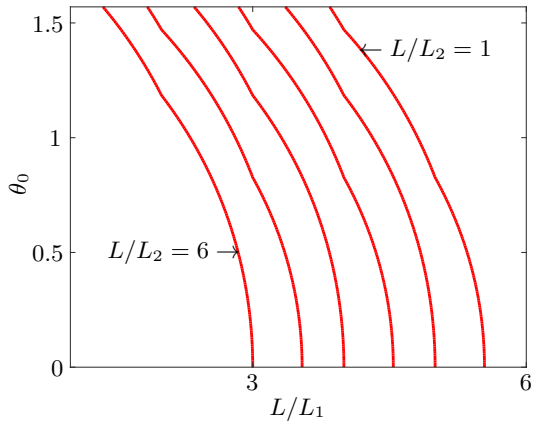

Figure 3.5 – Amplitude θ_0 as a function of L/L_1 for different values of L/L_2.

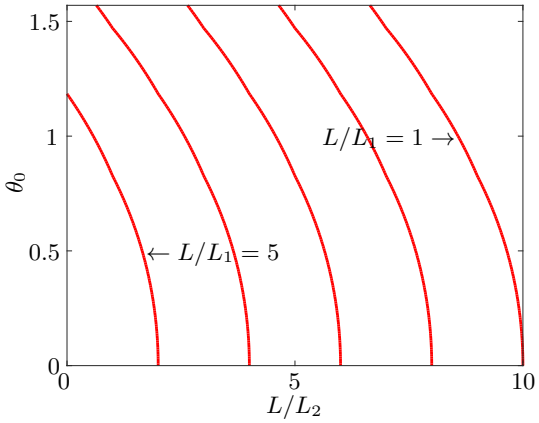

Figure 3.6 – Amplitude θ_0 as a function of L/L_2 for different values of L/L_1.

Since condition (3.39) involves angle amplitude θ_0 and L/L_1 as well as L/L_2, feasible trajectories can be produced by adjusting the architecture. In Fig. 3.5 and Fig. 3.6, L/L_2 and L/L_1 are respectively incremented by steps of 1. From these two figures, it can be concluded that a proper and easy-to-built architecture is one in which L_1 and L_2 do not have large differences. In this case, most proper solutions are such that $L > L_1$ and $L > L_2$, i.e., the length of base attachments is shorter than the platform which has some advantages when building a prototype having a relatively small footprint. Once an architecture is chosen, there is only one solution for θ_0 in the case that the combined translational trajectory with $\mathbf{p}_s = [x_s, 0]^T$ has the same frequency for translation and for rotation.

As an example, $L_1 = L/4$, $L_2 = L/2$ is taken. The corresponding $\theta_0 = 1.1844$ is obtained from (3.39) with the assumption that $m = 1\,\text{kg}$. Based on this architecture, different trajectories are analyzed in the following by choosing $\mathbf{c}$, $\mathbf{s}$ and x_s.

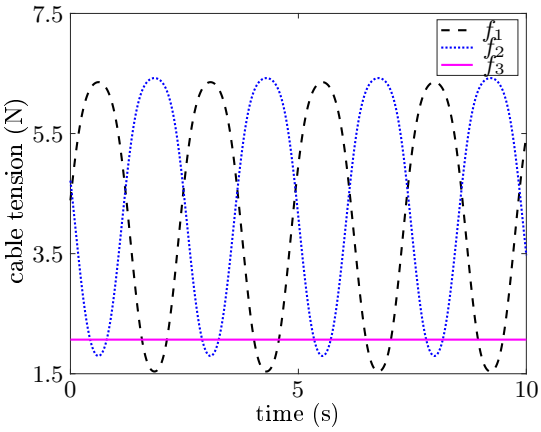

Figure 3.7 – Cable tensions for the pure rotation.

Pure Rotation

Pure rotation around the centre of mass of the platform is first considered. The point is chosen along the vertical x axis as shown in (3.16) with $\mathbf{c} = \mathbf{s} = \mathbf{0}$. That is

$$x = x_s, \quad y = 0, \quad x_0 > 0, \tag{3.40}$$

where x_s is the position coordinate of the centre of mass of the platform with respect to the y axis. The rotation is given in (3.25). Therefore, the platform rotates around $(x_0, 0)$ from 0 to θ_0. When $x_s = 1.5\,\text{m}$, the frequency is $\omega_n = \sqrt{g/x_s} = 2.5573$ rad/s and $k_1 = k_2 = 2.616\,\text{N/m}$, $k_3 = 1.308\,\text{N/m}$ are obtained numerically from (3.35) and (3.32). The corresponding cable tension $\{f_j\}_1^3$ are illustrated in Fig. 3.7. From this figure, it is observed that all cable tensions are positive. Since cable 3 is attached to the centre of mass of the platform, no direct moment can be produced by this cable with respect to the centre of mass of the platform and the cable tension remains constant during the whole trajectory. Cable 1 and cable 2 generate moments and thereby provide rotation.

Horizontal Oscillations with Combined Rotations

Periodic horizontal motion along a direction parallel to the y axis is defined in (3.16) with $\mathbf{c} = \mathbf{0}$, $\mathbf{s} = [0, \mu]^T$. That is

$$x = x_s, \quad y = \mu \sin \omega_n t, \quad x_s > 0, \quad \mu > 0, \tag{3.41}$$

where x_s is the position of the horizontal trajectory with respect to the y axis, μ is one half of the total horizontal range of motion, ω_n is the frequency of the periodic motion and t is the time. Combined with the rotational trajectory shown in (3.25), the robot is programmed to translate and rotate with the same frequency, from 0 to their maximum amplitudes. Moreover,

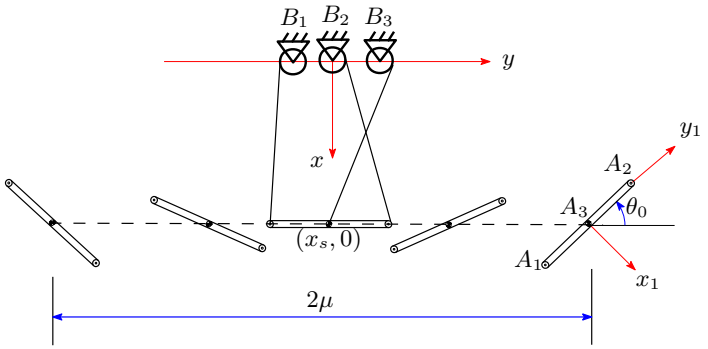

Figure 3.8 – Horizontal oscillations with combined rotations.

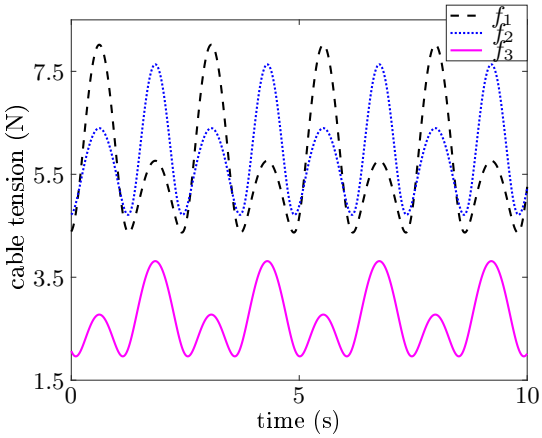

Figure 3.9 – Cable tensions for the horizontal oscillations with combined rotations.

the trajectory can operate beyond the static workspace. The corresponding motion is depicted in Fig. 3.8.

When $x_s = 1.5\,\text{m}$, $\mu = 2\,\text{m}$, the frequency is $\omega_n = \sqrt{g/x_s} = 2.5573$ rad/s and (3.35) and (3.32) can be used to obtain $k_1 = k_2 = 2.616\,\text{N/m}$, $k_3 = 1.308\,\text{N/m}$. The $\{k_j\}_1^3$ are the same as in the pure rotation since they are only related to $\mathbf{p}_s$. The cable tensions $\{f_j\}_1^3$ are illustrated in Fig. 3.9. From this figure, all cable tensions are positive during the whole trajectory.

Circular Motion with Combined Rotations

Circular motion centred on a point $(x_s,\, 0)$ lying on the x axis is designed using (3.16) with $\mathbf{c} = [\mu, 0]^T$ and $\mathbf{s} = [0, \mu]^T$. That is

$$x = x_s + \mu\cos\omega_n t, \quad y = \mu\sin\omega_n t, \quad x_0 > \mu > 0, \tag{3.42}$$

where μ is the radius of the circle, ω_n is the frequency of the periodic motion and t is the time. Combined with the rotational trajectory shown in (3.25), the robot is programmed to translate and rotate at the same time with the same frequency. The corresponding motion is

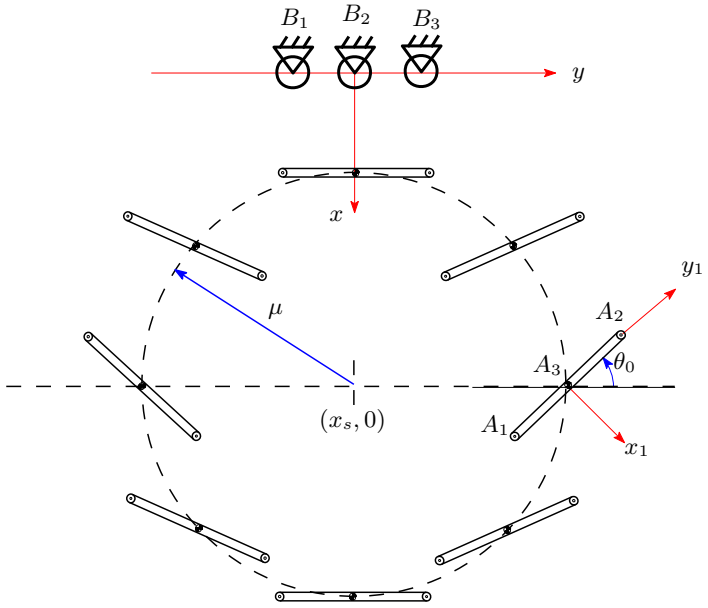

Figure 3.10 – Circular motion with combined rotations.

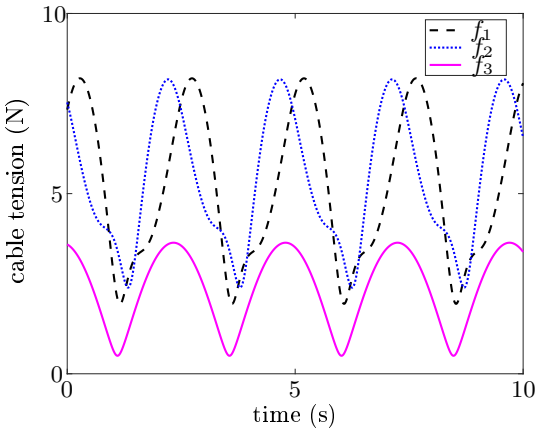

Figure 3.11 – Cable tensions for the circular motion with combined rotations.

depicted in Fig. 3.10.

When $x_s = 1.5\,\text{m}$, $\mu = 1.2\,\text{m}$, the frequency is $\omega_n = \sqrt{g/x_s} = 2.5573$ rad/s and (3.35) and (3.32) yield $k_1 = k_2 = 2.616\,\text{N/m}$, $k_3 = 1.308\,\text{N/m}$. The cable tensions $\{f_j\}_1^3$ are illustrated in Fig. 3.11. From this figure, it can be observed that all cable tensions are positive during the trajectory.

3.5 Conclusion

This chapter proposes a trajectory planning technique for three-DOF planar CSPRs. An equivalent passive mechanical system is introduced. Under certain circumstance, translational trajectories in global periodic parametric form are solved from corresponding linear differential

equations with constant coefficients. The rotational equation becomes akin to the dynamic equation of a nonlinear simple pendulum for which accurate solutions exist in the literature and are applied here. Natural trajectories corresponding to the results of the integration of the differential equations under some conditions are feasible. These trajectories have positive and constant ratios between cable tensions and cable lengths. The pure translations obtained are in agreement with the special cases previously identified in the literature.

A specific architecture is used to demonstrate the trajectory planning scheme. Examples of pure rotation and combined motions including translation and rotation that can be performed with the same frequency are analysed to demonstrate the results.

Chapter 4

Dynamic Periodic Trajectory Planning of Six-DOF CSPRs

4.1 Introduction

In the preceding chapters, a passive mechanical system that is dynamically equivalent to the CSPR is introduced to provide insight and facilitate the design of a set of periodic trajectories that can extend beyond the robot's static workspace. Natural trajectories with constant spring stiffnesses are obtained, which have no bounds on the amplitude. Oscillation in different directions can be used to produce linear, circular, and elliptical trajectories. However, these trajectories are unique with some restrictions. Variable stiffness trajectories which are much less restrictive on the type of motion that can be performed are not addressed and rotational trajectory planning in three-dimension is still a challenge.

In this chapter, linear trajectories are produced for fully actuated six-DOF CSPRs based on the analytical integration of the dynamic equations. Natural frequencies of the equivalent linear system are obtained and a generalization of the natural dynamic trajectories is accomplished by the integration of the linear system of differential equations. Cable tension constraints are imposed directly, rather than by substituting trajectories into the dynamic equations. In Section 4.2, the kinematic and dynamic models of the mechanism are presented and the vibration model of an equivalent passive system is introduced as a tool to help analyze the mechanism. Section 4.3 introduces the trajectory planning process of obtaining periodic trajectories by integrating the linear dynamic model. The associated natural frequencies are revealed. These trajectories include natural trajectories associated with constant-stiffness equivalent springs and extended linear trajectories associated with variable-stiffness equivalent springs. In Section 4.4, the trajectories obtained in Section 4.3 are applied to a specific robot architecture. Finally, an experimental prototype is used to validate the proposed technique, as shown in the supplementary video file.

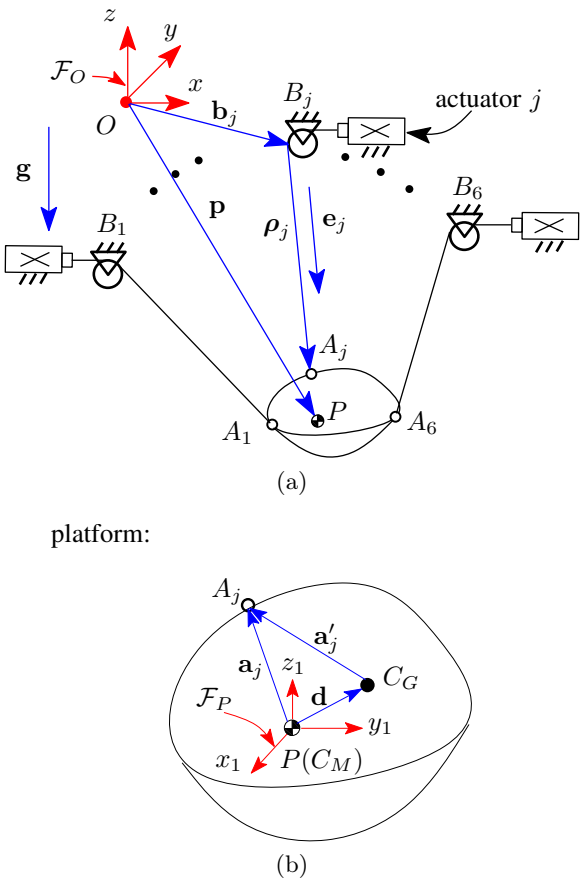

Figure 4.1 – Geometric parameters of a six-DOF cable-suspended parallel robot (CSPR).

4.2 Mechanics of Six-DOF CSPRs

In this section, the equations that govern the kinematics and dynamics of six-DOF CSPRs are first formulated. Then, the dynamic equations of an equivalent freely vibrating undamped system are derived. Finally, the differential equations of motion of this equivalent system are developed.

4.2.1 Robot Architecture

A general six-DOF CSPR is represented schematically in Fig. 4.1, with the symbols denoted in the introduction of the thesis, unless specified otherwise. Below, indices j should be assumed to go from 1 to 6 and a plural form of an item h_j is denoted $\{h_j\}_1^6$. Six actuated spools mounted on a fixed structure are used to control the extension of the cables. The robot has six actuators and six degrees of freedom and is therefore fully actuated, capable of controlling both the position and orientation of the platform. However, since cable transmission is unilateral and cables can become slack, the platform is not fully constrained.

4.2.2 Kinematic and Dynamic Modelling

A fixed reference frame $\mathcal{F}_O$ with origin O is defined on the base of the robot, as illustrated in Fig. 4.1. The z axis of the fixed reference frame points upwards, opposite to the direction of gravity. A moving reference frame $\mathcal{F}_P$ is located on the platform, with its origin P located at the centre of mass of the robot C_M. Point C_G is the geometric centre of the attachment points $\{A_j\}_1^6$ on the platform. The vector $\mathbf{d}$ connects C_M to point C_G and vector $\mathbf{a}'_j$ connects C_G to point A_j.

The inverse kinematic equations can be written as

$$\boldsymbol{\rho}_j = \mathbf{p} + \mathbf{Q}\mathbf{a}_j - \mathbf{b}_j, \tag{4.1}$$

and ρ_j is the effective cable length, given by

$$\rho_j = \sqrt{(\mathbf{p} + \mathbf{Q}\mathbf{a}_j - \mathbf{b}_j)^T(\mathbf{p} + \mathbf{Q}\mathbf{a}_j - \mathbf{b}_j)}.$$

The dynamic model of the platform is built using the Newton-Euler approach, which yields

$$\sum_{j=1}^{6}\left(\frac{-f_j}{\rho_j}\boldsymbol{\rho}_j\right) + m\mathbf{g} = m\ddot{\mathbf{p}}, \tag{4.2}$$

$$\sum_{j=1}^{6}(\mathbf{Q}\mathbf{a}_j) \times \left(-\frac{f_j}{\rho_j}\boldsymbol{\rho}_j\right) = \mathbf{I}\dot{\boldsymbol{\omega}} + \boldsymbol{\omega} \times (\mathbf{I}\boldsymbol{\omega}), \tag{4.3}$$

where $\mathbf{g} = [0, 0, -g]^T$ is the vector of gravitational acceleration, $\mathbf{I}$ is the inertial tensor of the platform around C_M with respect to the moving frame, namely

$$\mathbf{I} = \begin{bmatrix} I_{xx} & -I_{xy} & -I_{xz} \\ -I_{xy} & I_{yy} & -I_{yz} \\ -I_{xz} & -I_{yz} & I_{zz} \end{bmatrix}.$$

Equations (4.2) and (4.3) can be written in matrix form as

$$\mathbf{M}\mathbf{k} = \boldsymbol{\gamma}, \tag{4.4}$$

where

$$\boldsymbol{\gamma} = \begin{bmatrix} m(\mathbf{g} - \ddot{\mathbf{p}}) \\ \mathbf{I}\dot{\boldsymbol{\omega}} + \boldsymbol{\omega} \times \mathbf{I}\boldsymbol{\omega} \end{bmatrix}, \tag{4.5}$$

$$\mathbf{k} = \begin{bmatrix} k_1 & k_2 & k_3 & k_4 & k_5 & k_6 \end{bmatrix}^T, \quad k_j = \frac{f_j}{\rho_j}, \tag{4.6}$$

and

$$\mathbf{M} = \begin{bmatrix} \boldsymbol{\rho}_1 & \cdots & \boldsymbol{\rho}_6 \\ (\boldsymbol{\rho}_1 \times \mathbf{Q}\mathbf{a}_1) & \cdots & (\boldsymbol{\rho}_6 \times \mathbf{Q}\mathbf{a}_6) \end{bmatrix}, \tag{4.7}$$

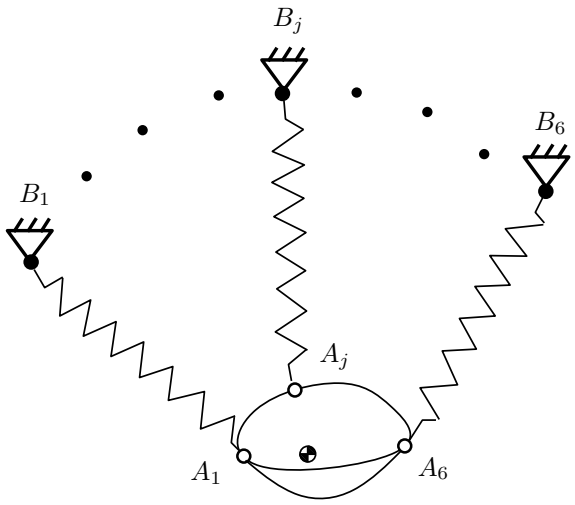

Figure 4.2 – A virtual equivalent mass-spring system for a six-DOF CSPR.

where $\mathbf{k}$ is the vector of cable tension-to-length ratios, whose components must all remain positive to ensure that the cables remain taut. The vector $\mathbf{f}$ of cable tensions is then written as

$$\mathbf{f} = \begin{bmatrix} k_1\rho_1 & k_2\rho_2 & k_3\rho_3 & k_4\rho_4 & k_5\rho_5 & k_6\rho_6 \end{bmatrix}^T. \tag{4.8}$$

4.2.3 Vibration Model of a Passive Equivalent System

A CSPR can be treated as a set of undamped mass-springs to gain insight into its behaviour and facilitate trajectory planning. Indeed, each of the actuator-cable modules can be replaced by a corresponding spring of stiffness k_j with zero free length and therefore the complete system can be modelled as a platform suspended by six springs, as illustrated in Fig. 4.2.

Applying (4.1), (4.2), (4.3) and (4.6), the dynamic equations for the system of Fig. 4.2 can be written as

$$\begin{aligned} m\ddot{\mathbf{p}} &= \mathbf{f}_{res} + m\mathbf{g} \\ &= -\sum_{j=1}^{6} k_j(\mathbf{p} + \mathbf{Q}\mathbf{a}_j - \mathbf{b}_j) + m\mathbf{g}, \end{aligned} \tag{4.9}$$

and

$$\begin{aligned} \mathbf{I}\dot{\boldsymbol{\omega}} + \boldsymbol{\omega} \times (\mathbf{I}\boldsymbol{\omega}) &= \sum_{j=1}^{6} k_j(\mathbf{p} + \mathbf{Q}\mathbf{a}_j - \mathbf{b}_j) \times \mathbf{Q}\mathbf{a}_j \\ &= \sum_{j=1}^{6} k_j(\mathbf{p} - \mathbf{b}_j) \times \mathbf{Q}\mathbf{a}_j, \end{aligned} \tag{4.10}$$

where $\mathbf{f}_{res}$ is the resultant cable force, k_j is the stiffness of the jth equivalent spring (referred to simply as the stiffness below), which has zero free length. In other words, the force in the jth spring is zero if ρ_j is equal to zero.

The purpose of this passive model is to guide trajectory planning for the active robot. Indeed, if natural free-motion trajectories of the passive system can be found, it can be guaranteed that these trajectories can be performed by the active robot while maintaining the cables in tension, as long as the actuator torque and velocity limits are respected.

4.3 Trajectory Planning

The dynamic model developed in Section 4.2 can be used to simulate the robot behaviour along any trajectory. It is observed that if the translational and rotational components of the trajectories are coupled such that

$$\sum_{j=1}^{6} k_j \mathbf{Q}\mathbf{a}_j = H\mathbf{p}, \tag{4.11}$$

with H being a scalar factor, which implies that vector $\sum_{j=1}^{6} k_j \mathbf{Q}\mathbf{a}_j$ is aligned with vector $\mathbf{p}$, the dynamic equation (4.10) becomes

$$\mathbf{I}\dot{\boldsymbol{\omega}} + \boldsymbol{\omega} \times (\mathbf{I}\boldsymbol{\omega}) = \sum_{j=1}^{6} k_j \mathbf{b}_j \times \mathbf{Q}\mathbf{a}_j \tag{4.12}$$

since

$$\sum_{j=1}^{6} k_j \mathbf{p} \times \mathbf{Q}\mathbf{a}_j = \mathbf{p} \times \sum_{j=1}^{6} k_j \mathbf{Q}\mathbf{a}_j = \mathbf{0}. \tag{4.13}$$

In addition, substituting (4.11) into (4.9), the translational component of the dynamic equations can be written as

$$m\ddot{\mathbf{p}} + \left(\sum_{j=1}^{6} k_j + H \right) \mathbf{p} - \mathbf{w} - m\mathbf{g} = \mathbf{0}, \tag{4.14}$$

where

$$\mathbf{w} = \sum_{j=1}^{6} k_j \mathbf{b}_j, \tag{4.15}$$

H is seen as the stiffness of a virtual spring, which is not associated with a particular cable but arises to respect the moment-component coupling in (4.11).

If the cable attachment points $\{B_j\}_1^6$ are in a plane at the same height and the origin of fixed frame $\mathcal{F}_O$ lies in this plane, the z-component of each vector $\mathbf{b}_j$ is zero. The last component of (4.14) can then be written as

$$K = \sum_{j=1}^{6} k_j + H = \frac{-m\,(g + \ddot{z})}{z}. \tag{4.16}$$

Furthermore, K is constant when z undergoes simple harmonic motion, according to

$$z = z_s + z_d, \tag{4.17}$$

with

$$z_s = -g/\omega_n^2, \quad z_d = \mu_{zc} \cos \omega_n t + \mu_{zs} \sin \omega_n t, \tag{4.18}$$

where $z_s < 0$ is the central static equilibrium position on the z axis, and constant, *unbounded* parameters μ_{zc} and μ_{zs} determine the amplitude of the motion, implying that the end-effector can go *above* the cable attachment points $\{B_j\}_1^6$.

In practice, trajectories that extend above $\{B_j\}_1^6$ impose many significant restrictions on CSPR design. In fact, for the six-DOF mechanism considered herein, such trajectories are not possible as they would result in cable interference. Therefore, only trajectories for which $z < 0$ are considered below, ensuring that the mechanism remains *suspended*.

Substituting (4.17) into the right-hand side of (4.16) yields

$$K = m\omega_n^2. \tag{4.19}$$

Under these circumstances, the nonlinear differential equations (4.14) simplify to linear differential equations, namely

$$m\ddot{\mathbf{p}} + m\omega_n^2 \mathbf{p} - \mathbf{w} - m\mathbf{g} = \mathbf{0}. \tag{4.20}$$

Physically, (4.20) describes an undamped harmonic oscillator, with the resultant cable force defined by combining (4.9), (4.11), (4.15), and (4.16) to obtain

$$\begin{aligned} \mathbf{f}_{res} &= -\sum_{j=1}^{6} k_j (\mathbf{p} + \mathbf{Q}\mathbf{a}_j - \mathbf{b}_j) \\ &= -\left(\sum_{j=1}^{6} k_j + H \right) \mathbf{p} + \mathbf{w} \\ &= -K\mathbf{p} + \mathbf{w}. \end{aligned}$$

This force assumed to be attached on the platform centre of mass always points to point W, which is the point in the $x-y$ plane located at the tip of vector $\mathbf{w}/K$, as shown in Fig. 4.3. In particular, if $\mathbf{w} = \mathbf{0}$, $\mathbf{f}_{res}$ points in the direction opposite to vector $\mathbf{p}$, i.e., from P toward O.

The process of the trajectory planning is as follows. Rotational component is first designed, while satisfying conditions (4.12) and (4.13) from which the relationship between $\{k_j\}_1^6$ can be obtained, referring to a specific architecture. The substitution of this relationship into (4.11) yields the scalar H. Then, combining with the conditions (4.16) and (4.19), which gives

$$\sum_{j=1}^{6} k_j + H = m\omega_n^2, \tag{4.21}$$

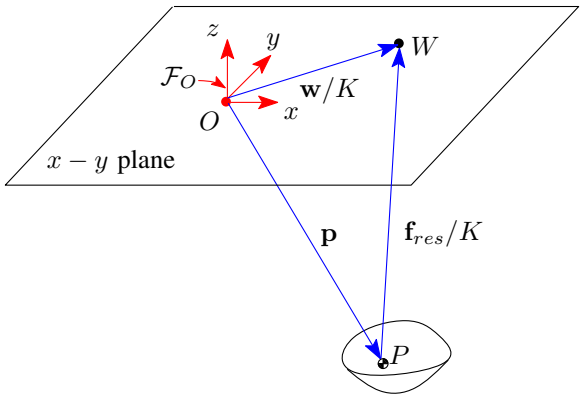

Figure 4.3 – Resultant cable force $\mathbf{f}_{res}$ points toward W, which is located in the $x-y$ plane.

the $\{k_j\}_1^6$ can be determined and the corresponding constraints for guaranteeing them to be positive can also be obtained. With the determined $\{k_j\}_1^6$, the vector $\mathbf{w}$ given in (4.15) can be determined. Therefore, the translational component can be obtained by analytically integrating the dynamic equation (4.20). In the following, pure translation and combined motions are designed by using this trajectory planning scheme.

4.3.1 Pure Translation

For pure translational trajectories, the fixed and moving frames are always in the same orientation, i.e., $\mathbf{Q} = \mathbf{1}$, the 3×3 identity matrix, and one has

$$\mathbf{I}\dot{\boldsymbol{\omega}} + \boldsymbol{\omega} \times (\mathbf{I}\boldsymbol{\omega}) = \mathbf{0}.$$

To provide insight into the fundamental properties of six-DOF CSPRs, natural trajectories are designed. These trajectories are based on the equivalent passive mechanical system with springs of *constant* stiffness $\{k_j\}_1^6$. If such motions are then followed by the robot, it can be guaranteed that the cable tensions will be positive at all times because the spring forces of the passive free vibrating system are positive at all times.

In order to produce pure translations, conditions (4.12) and (4.13) are required to be satisfied. For pure translation, equation (4.12) becomes

$$\sum_{j=1}^{6} k_j \mathbf{b}_j \times \mathbf{a}_j = \mathbf{0}. \tag{4.22}$$

Consider (4.13) now. Since each vector $\mathbf{a}_j$ is constant and constant spring stiffnesses $\{k_j\}_1^6$ are used for natural frequencies, (4.13) yields two conditions. One is that

$$\sum_{j=1}^{6} k_j \mathbf{a}_j = \mathbf{0}, \tag{4.23}$$

which implies that $H = 0$. Alternatively, $\mathbf{p}$ could be aligned with the constant vector $\sum_{j=1}^{6} k_j \mathbf{a}_j$, but this would only allow for trajectories which oscillate along the direction of

this vector. Equation (4.23) also implies that the convex hull defined by the attachment points on the platform includes the centre of mass, since each spring stiffness k_j must be positive. According to (4.21) with $H = 0$, (4.22), and (4.23), $\{k_j\}_1^6$ can be obtained. The determination of $\{k_j\}_1^6$ can also be found in the following equivalent process when the passive system is in static equilibrium. With (4.23), (4.9) and (4.10) in static equilibrium simplify to

$$\sum_{j=1}^{6} k_j \mathbf{b}_j + m\mathbf{g} = K\mathbf{p}_s, \tag{4.24}$$

$$-\sum_{j=1}^{6} k_j \mathbf{b}_j \times \mathbf{a}_j = \mathbf{0}, \tag{4.25}$$

where K is the *constant* total stiffness, given by

$$K = \sum_{j=1}^{6} k_j. \tag{4.26}$$

According to (4.24), (4.25), and (4.26), $\{k_j\}_1^6$ can be obtained for a specific architecture.

The substitution of the determined $\{k_j\}_1^6$ into (4.15) yields a constant vector $\mathbf{w}$, since each $\mathbf{b}_j$ is a constant vector. Then, (4.20) becomes a system of three linear differential equations with constant coefficients, given by

$$\ddot{\mathbf{p}} + \omega_n^2 \mathbf{p} - (\mathbf{v} + \mathbf{g}) = \mathbf{0}, \tag{4.27}$$

where $\mathbf{v} = [v_1, v_2, 0]^T = \mathbf{w}/m$ is constant. The last component of vector $\mathbf{v}$ is zero if the z-component of each vector $\mathbf{b}_j$ is zero, i.e., if points $\{B_j\}_1^6$ and O are in the same horizontal plane. Therefore, the translational component of the trajectories can be obtained by analytically integrating (4.27) to obtain

$$\mathbf{p} = \mathbf{p}_s + \mathbf{p}_d \tag{4.28}$$

with

$$\mathbf{p}_s = [x_s, y_s, z_s]^T = \mathbf{p}_{s1} + \mathbf{p}_{s2} \tag{4.29}$$

where

$$\mathbf{p}_{s1} = \left[0, 0, -\frac{g}{\omega_n^2}\right]^T, \quad \mathbf{p}_{s2} = \left[\frac{v_1}{\omega_n^2}, \frac{v_2}{\omega_n^2}, 0\right]^T,$$

and

$$\mathbf{p}_d = \mathbf{c}\cos\omega_n t + \mathbf{s}\sin\omega_n t, \tag{4.30}$$

where the natural frequency is

$$\omega_n = \sqrt{\frac{K}{m}}, \tag{4.31}$$

$\mathbf{c} = [\mu_{xc}, \mu_{yc}, \mu_{zc}]^T$, and $\mathbf{s} = [\mu_{xs}, \mu_{ys}, \mu_{zs}]^T$. Geometrically speaking, $\mathbf{p}_s$ represents the central static equilibrium position, which have to be located in the robot's static workspace, and $\mathbf{c}$ and $\mathbf{s}$ are design parameters that determine the shape of the motion.

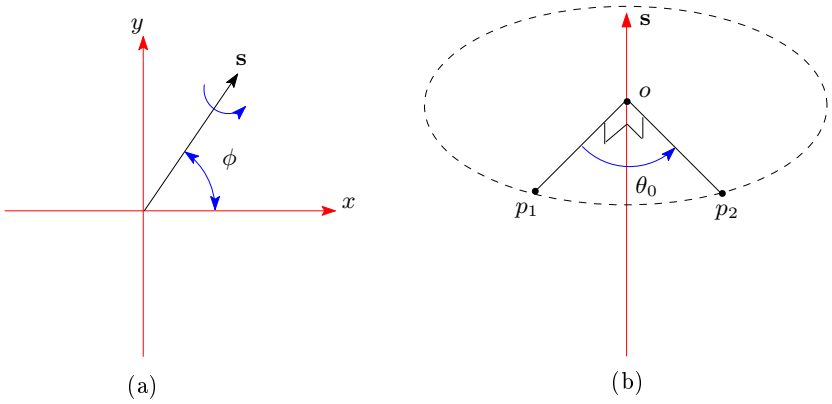

Figure 4.4 – The vector of axis of rotation **s**.

Under these conditions, when $\mathbf{p}_d$ is defined according to (4.30) and $\mathbf{p}_s$ is located in the static workspace, it can be guaranteed that the tensions in the cables will remain positive because the equivalent spring stiffnesses are always positive. During these trajectories, when (4.23) is applied, the resultant cable force becomes

$$\mathbf{f}_{res} = -\sum_{j=1}^{6} k_{sj}(\mathbf{p} - \mathbf{b}_j) = -\sum_{j=1}^{6} k_{sj}\mathbf{p} + \mathbf{w}. \tag{4.32}$$

4.3.2 Combined Motions

Natural trajectories provide considerable insight into the behaviour of the mechanism and can be described with a relatively simple mathematical formulation. However, these trajectories are unique and very restrictive. To permit trajectories with fewer restrictions, extended linear trajectories corresponding to the linear system (4.20) with *variable* spring stiffnesses are developed by applying a similar approach to that used for natural trajectories. In the following, rotational component is first designed and corresponding translational component is then obtained from the dynamic equations. These trajectories are associated with variable-stiffness springs.

The rotational motion is described using the tilt-and-torsion (T&T) angle convention, which is a suitable approach for parallel mechanisms (Bonev et al., 2002). In this convention, ϕ represents the azimuth angle, while θ is the tilt angle and σ is the torsion angle. The rotational component is designed such that the torsion angle θ is set to zero to avoid cable tangling and the tilt angle σ is prescribed to be constant, according to

$$\begin{aligned} &\phi = \omega_n t - \pi/2, \quad \dot{\phi} = \omega_n, \quad \ddot{\phi} = 0 \\ &\sigma = \dot{\sigma} = \ddot{\sigma} = 0, \\ &\theta = \theta_0, \quad \dot{\theta} = \ddot{\theta} = 0, \end{aligned} \tag{4.33}$$

which are depicted in Fig. 4.4. The unit vector $\mathbf{s} = [\cos\phi, \sin\phi, 0]^T$ represents the axis of

rotation and the rotation matrix corresponding to a rotation of angle $\theta = \theta_0$ around $\mathbf{s}$ is given as

$$\mathbf{Q} = \mathbf{s}\mathbf{s}^T + \cos\theta_0(\mathbf{1} - \mathbf{s}\mathbf{s}^T) + \sin\theta_0\mathbf{S}, \tag{4.34}$$

where $\mathbf{S}$ is the cross-product matrix of the vector $\mathbf{s}$. Upon expansion, one has

$$\mathbf{Q} = \begin{bmatrix} c_\phi^2 + c_0 s_\phi^2 & c_\phi s_\phi(1 - c_0) & s_0 s_\phi \\ c_\phi s_\phi(1 - c_0) & s_\phi^2 + c_0 c_\phi^2 & -s_0 c_\phi \\ -s_0 s_\phi & s_0 c_\phi & c_0 \end{bmatrix},$$

where $c_0 = \cos\theta_0$, $s_0 = \sin\theta_0$, $c_\phi = \cos\phi$, and $s_\phi = \sin\phi$.

The cross-product matrix $\boldsymbol{\Omega}$ of the vector $\boldsymbol{\omega}_O = \begin{bmatrix} \omega_{1O} & \omega_{2O} & \omega_{3O} \end{bmatrix}^T$ which is the angular velocity of the platform with respect to the fixed frame, can be obtained as

$$\boldsymbol{\Omega} = \dot{\mathbf{Q}}\mathbf{Q}^T = \begin{bmatrix} 0 & -\omega_{3O} & \omega_{2O} \\ \omega_{3O} & 0 & -\omega_{1O} \\ -\omega_{2O} & \omega_{1O} & 0 \end{bmatrix}. \tag{4.35}$$

According to the rotational component designed in (4.33), the angular velocity $\boldsymbol{\omega}$ can then be obtained as

$$\boldsymbol{\omega} = \mathbf{Q}^T\boldsymbol{\omega}_O = \omega_n \begin{bmatrix} -\sin\theta_0 \sin\phi \\ \sin\theta_0 \cos\phi \\ -1 + \cos\theta_0 \end{bmatrix}, \tag{4.36}$$

which determines the angular acceleration $\dot{\boldsymbol{\omega}}$ as

$$\dot{\boldsymbol{\omega}} = -\omega_n^2 \sin\theta_0 \mathbf{s}. \tag{4.37}$$

Therefore, with the assumption that $I_{xy} = I_{xz} = I_{yz} = 0$ and $I_{xx} = I_{yy}$, the external moment on C_M can be obtained as

$$\mathbf{I}\dot{\boldsymbol{\omega}} + \boldsymbol{\omega} \times (\mathbf{I}\boldsymbol{\omega}) = c_w \mathbf{s} \tag{4.38}$$

where

$$c_w = \omega_n^2 \sin\theta_0 c_I, \quad c_I = -I_{zz}(1 - \cos\theta_0) - I_{xx}\cos\theta_0. \tag{4.39}$$

The constraints imposed on the elements of inertial tensor imply that if equipment such as a scanning/video system is mounted on the platform, it must be carefully located and/or counterbalanced.

For the linear system (4.20), $\mathbf{p}$ has a similar form as (4.28) but with $\mathbf{p}_s = \mathbf{p}_{s1} = [0, 0, -g/\omega_n^2]^T$ while adding a particular solution $\mathbf{p}_w$ associated with vector $\mathbf{w}$, namely

$$\mathbf{p} = \mathbf{p}_s + \mathbf{p}_d + \mathbf{p}_w. \tag{4.40}$$

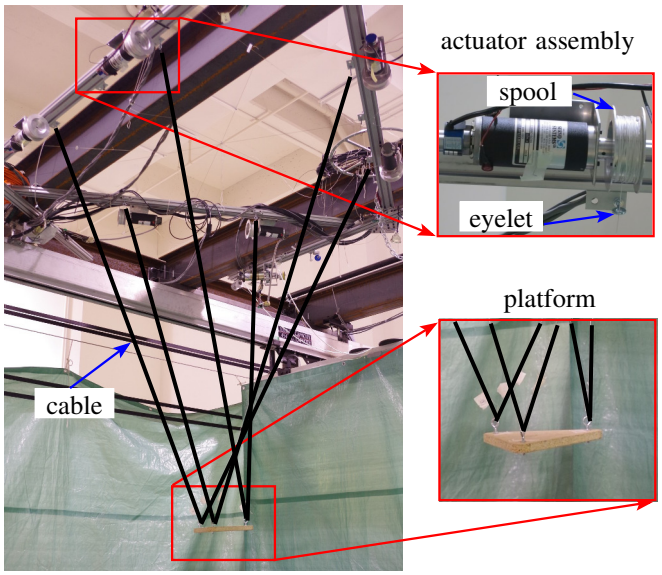

Figure 4.5 – Six-DOF CSPR prototype.

4.4 Experimental Validation

The experimental prototype shown in Fig. 4.5 is used to validate the proposed technique. Natural trajectories with constant stiffness springs $\{k_j\}_1^6$ are planned first, for which the amplitude is not bounded. Then, trajectories associated with variable but positive stiffnesses $\{k_j\}_1^6$ are designed, which are formed by integrating the linear system (4.20).

The main benefit of the proposed approach is the ability to plan trajectories that extend beyond the static workspace of the robot. Although this workspace cannot be intuitively represented when orientation and position vary at the same time, it obviously lies within the hexagonal-prism-shaped volume formed when projecting the fixed-frame cable attachment points downward. In the supplementary video file, one edge of the static workspace is clearly shown by slowly commanding the robot to move in one horizontal direction, until a cable starts to sag. Later in the video, while following dynamic trajectories, the cables are clearly all taut when the platform is beyond this point. Therefore, the dynamic trajectories clearly exit the hexagonal-prism-shaped volume, so they must also exit the static workspace. In fact, the platform could have gone much further outside the static workspace had it not been for a few obstacles nearby.

4.4.1 Architecture of the Prototype

The architecture of the prototype is illustrated in Fig. 4.6. This geometry was proposed in (Gosselin and Bouchard, 2010), based on an optimization of the feasible static workspace. Spools $\{B_j\}_1^6$ are evenly placed on a circle of radius $R = 0.68\,\mathrm{m}$. Cables are connected by pairs to the moving platform, to three attachment points that form an equilateral triangle

circumscribed by a circle of radius $r = 0.1\,\text{m}$. The centre of mass C_M is located at a distance d below the geometric centre of the platform attachment points C_G, i.e., $\mathbf{d} = [0, 0, d]^T$. The mass of the platform is $m = 0.316\,\text{kg}$. The cable attachment point vectors are given by

$$\mathbf{b}_j = R \begin{bmatrix} \cos\beta_{bj} & \sin\beta_{bj} & 0 \end{bmatrix}^T, \tag{4.41}$$

with $\beta_{bj} = \frac{(j-1)\pi}{3} + \frac{\pi}{6}$ and

$$\mathbf{a}_j = \begin{bmatrix} r\cos\beta_{aj} & r\sin\beta_{aj} & d \end{bmatrix}^T, \tag{4.42}$$

with $\beta_{aj} = -\frac{2(j-1)\pi}{3} + \frac{\pi}{2}$. Numerical values for these vectors are provided in Table 4.1 with $d = 0$.

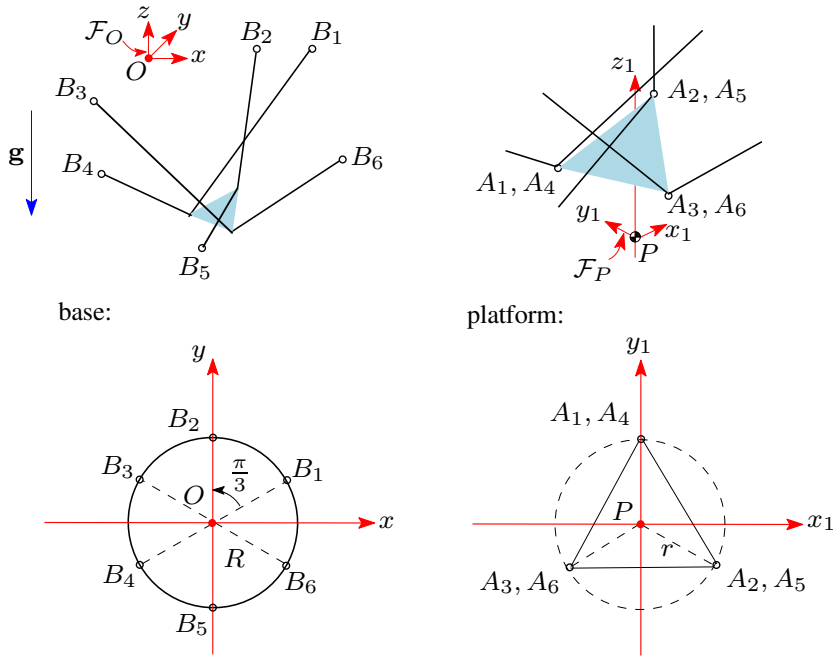

Figure 4.6 – Geometry of the cable attachment points for the six-DOF CSPR prototype.

Table 4.1 – The cable attachment points.

j	$\mathbf{b}_j^T$ [m]	$\mathbf{a}_j^T$ [m]
1	[0.589 0.34 0]	[0.000 0.10 0]
2	[0.000 0.68 0]	[0.087 -0.05 0]
3	[-0.589 0.34 0]	[-0.087 -0.05 0]
4	[-0.589 -0.34 0]	[0.000 0.10 0]
5	[0.000 -0.68 0]	[0.087 -0.05 0]
6	[0.589 -0.34 0]	[-0.087 -0.05 0]

In order to demonstrate the proposed trajectory planning scheme, Trajectories are designed, during which

$$\sum_{j=1}^{6} k_j \mathbf{Q}\mathbf{a}_j = \mathbf{Q}\sum_{j=1}^{6} k_j \mathbf{a}_j = \mathbf{0} \tag{4.43}$$

namely, parameter $H = 0$ according to (4.11). The latter equation implies that the convex hull defined by the attachment points on the platform includes the centre of mass, since each spring stiffness k_j must be positive. With the vectors $\{\mathbf{a}_j\}_1^6$ given in (4.42), one finds $d = 0$, which is a necessary condition for accomplishing these trajectories. Moreover, conditions that can yield these motions are obtained and used to determine cable tensions. Example trajectories are demonstrated in the following for a specific architecture.

Transitional trajectories proposed in (Gosselin, 2013) are applied to start from the state of rest and blend into the periodic trajectories. Using the algorithms presented in (Perreault et al., 2010), it is guaranteed that no interference will occur among the cables or between the cables and the platform during the motion.

4.4.2 Natural Pure Translation

As described in Section 4.3, trajectories can be designed based on (4.13) and (4.12) which are sufficient conditions for pure translational trajectories, and which are dependent with (4.15). If φ_j is defined as the angle between vector $\mathbf{Q}\mathbf{a}_j$ and vector $\mathbf{b}_j$, $\{\varphi_j\}_1^6$ represent the equation

$$\varphi_j + \varphi_{j+3} = \pi, \quad j = 1, 2, 3$$

due to the symmetric arrangement of the cable attachment points. This leads in turn to

$$\mathbf{b}_j \times \mathbf{Q}\mathbf{a}_j + \mathbf{b}_{j+3} \times \mathbf{Q}\mathbf{a}_{j+3} = \mathbf{0}.$$

Then, cable stiffnesses $\{k_j\}_1^6$ are chosen to be

$$k_1 = k_4, \quad k_2 = k_5, \quad k_3 = k_6, \tag{4.44}$$

to respect condition (4.12). With $\{\mathbf{b}_j\}_1^6$ defined according to (4.41), one has $\mathbf{w} = \mathbf{0}$ according to (4.15). Additionally, for this *symmetric* mechanism, the resultant cable force assumed to be attached on the centre of mass of the platform always points to the origin of the fixed frame O during the trajectories designed in Section 4.3. The motion of the platform is governed by the linear dynamic equations (4.27).

For the specific architecture of the experimental prototype, positive constant stiffnesses $\{k_j\}_1^6$ can be readily obtained from the constraints that define these trajectories, as shown below for the cases of natural pure translation.

Natural pure translation is simple harmonic motion, defined in (4.28). Substituting the spring stiffnesses defined in (4.44) and vectors $\{\mathbf{a}_j\}_1^6$ given in (4.42) with $d = 0$ into (4.23), k_j equals

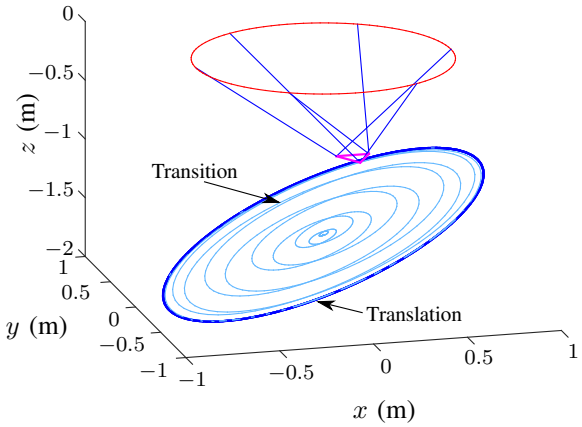

Figure 4.7 – Representation of the constant-orientation ellipse, including transitions.

to each other. When this result is combined with the expressions for the natural frequencies given in (4.21), $\{k_j\}_1^6$ are found to be

$$k_1 = k_2 = k_3 = k_4 = k_5 = k_6 = m\omega_n^2/6.$$

It is readily seen that $\{k_j\}_1^6$ are always positive and constant. Additionally, the trajectory amplitude is unbounded, defined according to $\mathbf{c}$ and $\mathbf{s}$ in (4.30).

An example of elliptical translational motion is now provided. Elliptical translational linear trajectories are defined as

$$\begin{aligned} x &= \mu_1 \cos\alpha \cos\omega_n t - \mu_2 \sin\alpha \sin\omega_n t, \\ y &= \mu_1 \sin\alpha \cos\omega_n t + \mu_2 \cos\alpha \sin\omega_n t, \\ z &= z_s + \mu_{zc} \cos\omega_n t, \end{aligned} \tag{4.45}$$

where α is the angle between the x-axis and the major axis of the ellipse, z_s is the elevation of the horizontal elliptical trajectory, μ_1 is the major semi-axis, μ_2 is the minor semi-axis, μ_{zc} is the amplitude of z oscillations, ω_n is the natural frequency of translation, and t is time. This trajectory satisfies (4.28) with $\mathbf{p}_s = [0, 0, z_s]^T$, $\mathbf{c} = [\mu_1 \cos\alpha, \mu_1 \sin\alpha, \mu_{zc}]^T$, and $\mathbf{s} = [-\mu_2 \sin\alpha, \mu_2 \cos\alpha, 0]^T$.

The following parameters are chosen: $\alpha = \pi/6$, $z_s = -1.5\,\text{m}$, $\mu_1 = 1\,\text{m}$, $\mu_2 = 0.6\,\text{m}$, $\mu_{zc} = 0.4\,\text{m}$, $d = 0.035\,\text{m}$. The frequency is therefore $\omega_n = \sqrt{-g/z_s} = 2.5573\,\text{rad/s}$. The resulting motion is illustrated schematically in Fig. 4.7, including the transition phase. The cable tensions remain positive and continuous along the entire trajectory, as shown in Fig. 4.8.

4.4.3 Combined Linear Trajectories

In order to produce the rotational component designed in Section 4.3, conditions (4.12), (4.38), and (4.43) are applied to obtain the relationship between $\{k_j\}_1^6$. Based on (4.12) and (4.38),

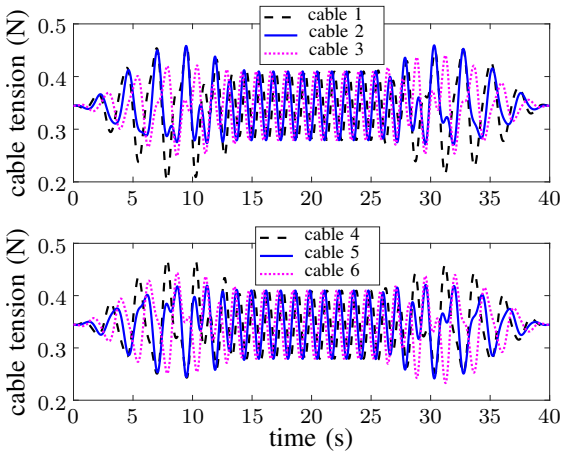

Figure 4.8 – Cable tensions during the constant-orientation ellipse, including transitions.

one has

$$k_1 = k_4 + k_{10}, \quad k_2 = k_5 + k_{20}, \quad k_3 = k_6 + k_{30}, \tag{4.46}$$

where

$$\begin{aligned} k_{10} &= \frac{2\omega_n^2 c_I(\cos 2\phi - \sqrt{3}\sin 2\phi)}{3Rr}, \\ k_{20} &= \frac{-2\omega_n^2 c_I(\cos 2\phi + \sqrt{3}\sin 2\phi)}{3Rr}, \\ k_{30} &= \frac{-4\omega_n^2 c_I \cos 2\phi}{3Rr}. \end{aligned} \tag{4.47}$$

In addition, according to (4.43), one also has

$$k_1 = k_3 - k_4 + k_6, \quad k_2 = k_3 - k_5 + k_6, \tag{4.48}$$

Combining (4.46) and (4.48), $\{k_j\}_1^6$ become functions of k_6, namely

$$\mathbf{k} = k_6 + \frac{1}{2}\begin{bmatrix} k_{30} + k_{10} \\ k_{30} + k_{20} \\ 2k_{30} \\ k_{30} - k_{10} \\ k_{30} - k_{20} \\ 0 \end{bmatrix} \tag{4.49}$$

Substituting (4.49) and $H = 0$ into (4.21), one then has

$$m\omega_n^2 = \sum_{j=1}^{6} k_j = 6k_6 + \frac{-4\omega_n^2 c_I \cos 2\phi}{Rr}, \tag{4.50}$$

which yields

$$k_6 = \frac{1}{6}\left(m\omega_n^2 + \frac{4\omega_n^2 c_I \cos 2\phi}{Rr}\right). \tag{4.51}$$

Therefore, $\{k_j\}_1^6$ can be determined by substituting (4.51) into (4.49), namely

$$\mathbf{k} = \frac{1}{6}m\omega_n^2 - \frac{2}{3Rr}c_I\omega_n^2 \begin{bmatrix} -\cos(2\phi+\pi/3) \\ \cos(2\phi-\pi/3) \\ \cos 2\phi \\ \cos(2\phi+\pi/3) \\ -\cos(2\phi-\pi/3) \\ -\cos 2\phi \end{bmatrix}. \tag{4.52}$$

For the specific architecture as shown in Fig. 4.6, one has

$$I_{xx} = \frac{1}{4}mr^2, \quad I_{zz} = \frac{1}{2}mr^2.$$

The substitution of these values and (4.39) into the obtained $\{k_j\}_1^6$ yields

$$\mathbf{k} = \frac{1}{6}m\omega_n^2 + \frac{r}{6R}m\omega_n^2(2-\cos\theta_0) \begin{bmatrix} -\cos(2\phi+\pi/3) \\ \cos(2\phi-\pi/3) \\ \cos 2\phi \\ \cos(2\phi+\pi/3) \\ -\cos(2\phi-\pi/3) \\ -\cos 2\phi \end{bmatrix}. \tag{4.53}$$

Using the bounds of trigonometric functions, for any value of $\theta_0 \in (-\pi/2, \pi/2)$ and ϕ, the sufficient condition for each $k_j > 0$ is as follows

$$\frac{r}{R} < \frac{1}{3}, \tag{4.54}$$

which is always satisfied for the prototype applied here.

Then, substituting (4.52) into (4.15), one has

$$\mathbf{w} = \sum_{j=1}^{6} k_j \mathbf{b}_j = \frac{\omega_n^2 c_I}{r} \begin{bmatrix} -\sin 2\phi + \sqrt{3}\cos 2\phi \\ -\sqrt{3}\sin 2\phi - \cos 2\phi \\ 0 \end{bmatrix}. \tag{4.55}$$

According to the determined vector $\mathbf{w}$, $\mathbf{p}$ can be obtained by the integration of the linear system (4.20), which is given in (4.40), where

$$\begin{aligned} &\mathbf{p}_s = [0, 0, z_s]^T, \quad \mathbf{p}_d = \mathbf{c}\cos\omega_n t + \mathbf{s}\sin\omega_n t, \\ &\mathbf{p}_w = \mathbf{c}_p \cos 2\omega_n t + \mathbf{s}_p \sin 2\omega_n t \end{aligned} \tag{4.56}$$

with $\mathbf{c}$ and $\mathbf{s}$ are unbounded,

$$\mathbf{c}_p = \mu_p[\sqrt{3}, -1, 0]^T, \quad \mathbf{s}_p = \mu_p[-1, -\sqrt{3}, 0]^T, \quad \mu_p = \frac{c_I}{3mr}.$$

It is observed that μ_p is a constant that is related to the inertial tensor of the platform and a constant tilt angle θ_0. In other words, only $\mathbf{c}$ and $\mathbf{s}$ are free parameters and can be adjusted to obtain different shape of trajectories. In addition, $\mathbf{p}_w$ can be rewritten in the following form, which in fact is a function of a circle in the $x-y$ plane, namely

$$\mathbf{p}_w = 2\mu_p \begin{bmatrix} \cos(2\omega_n t + \pi/6) \\ -\sin(2\omega_n t + \pi/6) \\ 0 \end{bmatrix}. \tag{4.57}$$

Therefore, according to (4.54), the cables are always in tension during the combined linear trajectories with the rotational component defined in (4.33) and the translational component given in (4.56).

One example of a combined linear trajectory involves the platform translating in the $x-y$ plane while oscillating in the z direction and rotating at the same time, according to

$$\begin{aligned} x &= \mu \cos\omega_n t + 2\mu_p \cos(2\omega_n t + \pi/6), \\ y &= \mu \sin\omega_n t - 2\mu_p \sin(2\omega_n t + \pi/6), \\ z &= z_s + \mu_{zs} \sin\omega_n t, \end{aligned} \tag{4.58}$$

and

$$\phi = \omega_n t - \pi/2, \quad \theta = \theta_0, \quad \sigma = 0. \tag{4.59}$$

The positioning of the platform is designed according to (4.56) while choosing

$$\mathbf{c} = [\mu, 0, 0]^T, \quad \mathbf{s} = [\mu, 0, \mu_{zs}]^T.$$

Additionally, if the constraints

$$z_s < 0, \qquad z_s + \mu_{zs} < 0 \tag{4.60}$$

are imposed, the platform is guaranteed to remain below the $x-y$ plane, shown in Fig. 4.9, which contains all of the fixed cable attachment points.

The normal to the platform intersects the z axis at a location that oscillates in the same way as the z coordinate of the platform itself. This motion is represented schematically in Fig. 4.9, where it can be clearly seen that the intersection of the platform normal vector with the z axis is located at $z' = z + d_z$. in addition, vector $\mathbf{f}_{res}$ points toward point W which is located on a circle given in (4.57).

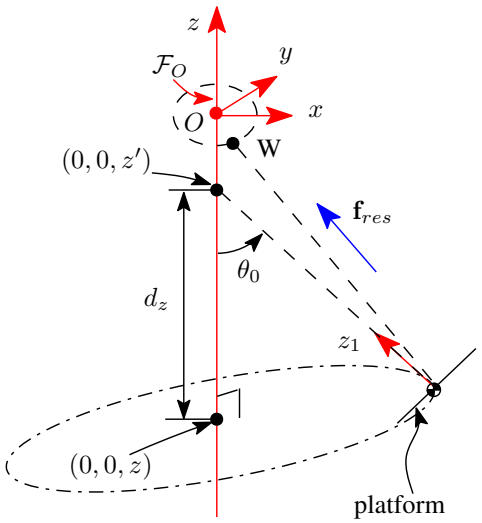

Figure 4.9 – Position of the intersection point between the vector normal to the platform and the z axis.

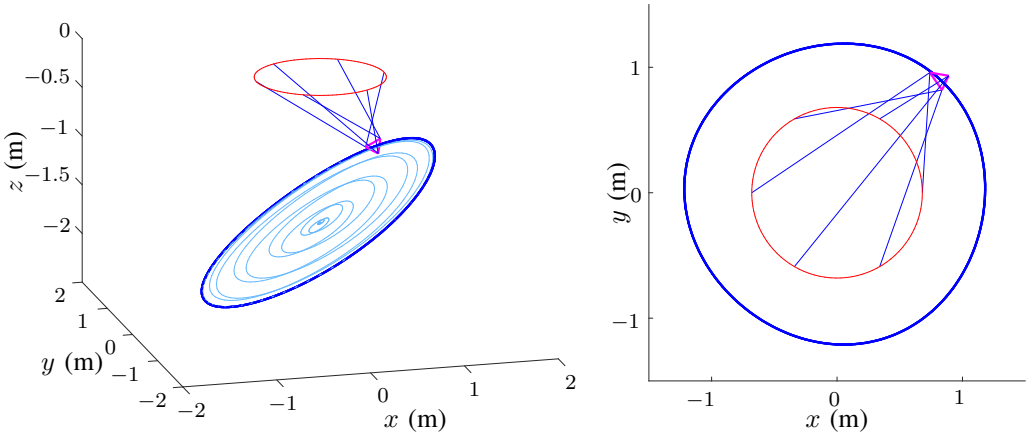

(a) 3D view. (b) Top view.

Figure 4.10 – Representation of the combined linear motion, including transitions.

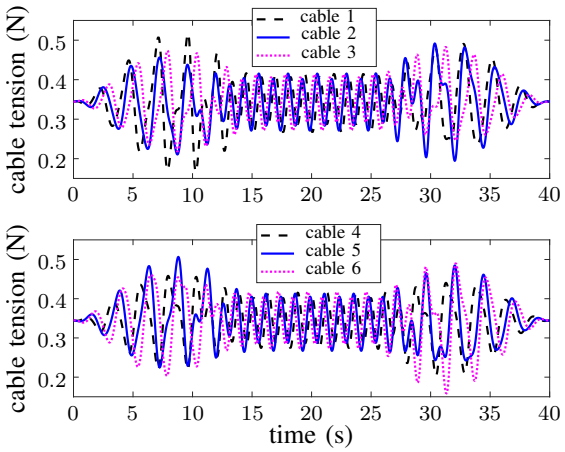

Figure 4.11 – Cable tensions during the combined linear trajectory.

To demonstrate a combined linear trajectory with variable spring stiffnesses, an example is provided, which uses the following parameters: $z_s = -1.2\,\mathrm{m}$, $\mu = 1.2\,\mathrm{m}$, $\theta_0 = \pi/4$, $\mu_{zs} = 0.72\,\mathrm{m}$. The natural frequency is $\omega_n = \sqrt{-g/z_s} = 2.8592\,\mathrm{rad/s}$. According to the specific architecture and the constant tilt angle θ_0, one has $\|\mu_p\| = 0.0187\,\mathrm{m}$. The resulting motion is illustrated schematically in Fig. 4.10, including the transition phase. The positioning of the platform is very similar to that shown in Fig. 4.7, the distinguishing features of the combined linear trajectories being that *the platform orientation is variable* and the projection of the translational component in the $x - y$ plane is approximate to a circle. This trajectory guarantees continuous and positive cable tensions, as is confirmed in Fig. 4.11.

4.5 Conclusion

In this chapter, the performance of dynamically feasible trajectories with six-DOF CSPRs is investigated by exploring the fundamental properties of CSPRs. An equivalent passive mechanical system is applied and a set of linear trajectories that can go beyond the static workspace are designed. One key insight is to divide the dynamic equations into two parts: (4.20), which is a differential equation that can be integrated to yield periodic trajectories; and (4.13), (4.12) and (4.15), which are used as constraints on (4.20), ensuring that cable tensions remain positive.

Several classes of linear trajectories are investigated for the six-DOF mechanism. The first involves pure translation. Natural trajectories that correspond to constant-stiffness springs for the equivalent passive mechanical system are investigated, for which there is no restriction on the amplitude of oscillations. Thirdly, variable-stiffness springs are explored to permit more general trajectories, such as oscillation in all three directions while also changing the platform orientation. For each type of trajectory, the positive-tension conditions are identified. An experimental prototype is used to demonstrate the trajectories, including transitions.

The main benefit of the proposed approach is that it can be used to plan dynamic trajectories that extend beyond the static workspace of the mechanism. Moreover, the basic trajectories introduced can be used as building blocks to synthesize more complex motion.

4.6 Supplementary Data

Extension2-chapter4-periodic-6DOF.mp4 —The supplementary video file shows the experimental prototype following several trajectories. Initially, the platform is moved slowly in a horizontal direction until one of the cables is clearly sagging, thereby showing the approximate edge of the static workspace. Then, trajectories involving both position and orientation control are shown.

Part II

Dynamic Point-to-Point Trajectory Planning

Chapter 5

Dynamic Point-to-Point Trajectory Planning of Three-DOF Point-Mass CSPRs

5.1 Introduction

Although periodic trajectories provide insight into the fundamental properties of CSPRs, point-to-point trajectories are often more appropriate in practice. Additionally, the techniques for periodic trajectory planning described in the preceding part of the thesis do not provide a systematic approach for identifying trajectory equation parameters that will ensure kinematic constraints that are respected at the endpoints.

In this chapter, a technique is proposed for planning trajectories beyond the static workspace of three-DOF point-mass CSPRs. A basis motion is also introduced, which is a general mathematical function that is adapted for each trajectory segment by selecting coefficients and other parameters that allow kinematic constraints to be respected. The technique ensures zero velocity at each of the target points and continuity of the accelerations. Based on the cable tension constraints, attainable regions can be determined to search for the next target point while feasible regions of intermediate points are generated in cases for which a given point cannot be directly attained. This approach is much more straightforward than previously used techniques presented in (Gosselin and Foucault, 2014; Jiang and Gosselin, 2016a).

The dynamic model of the robot is used for planning each trajectory segment, which ensures that cables always remain in tension. Section 5.3 describes the basis motion, while the novel trajectory-planning technique using this motion is introduced in Section 5.5. Section 5.5 provides example trajectories and experimental results for a specific architecture. Feasible regions are obtained to search for target points and intermediate points. Finally, a video of the implementation on a prototype is included in order to illustrate the results.

5.2 Mechanics of Three-DOF Point-Mass CSPRs

The equations that govern the kinematics and dynamics of a spatial three-DOF CSPR with a point mass are summarized, with a more detailed description provided in Chapter 2. This mechanism is again illustrated in Fig. 5.1, with the symbols denoted in the introduction of the thesis, unless specified otherwise. Below, indices j should be assumed to go from 1 to 3 and a plural form of an item h_j is denoted $\{h_j\}_1^3$.

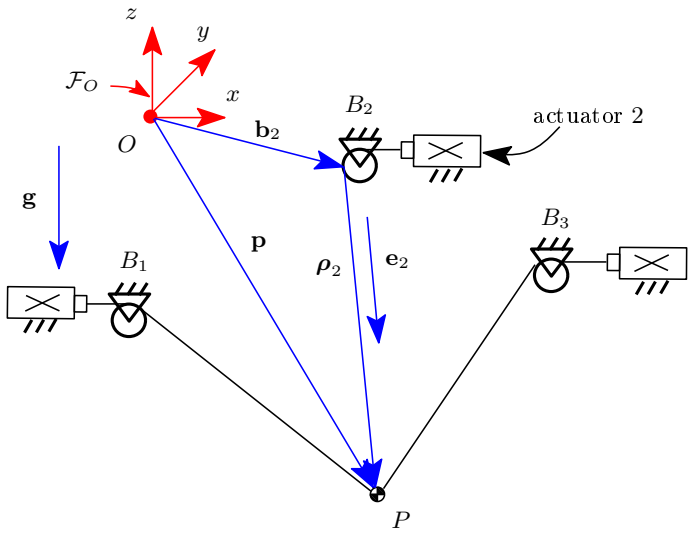

Figure 5.1 – Prototype of a spatial three-DOF CSPR with point mass.

The inverse kinematic equations can be written as

$$\rho_j = \sqrt{(\mathbf{p} - \mathbf{b}_j)^T(\mathbf{p} - \mathbf{b}_j)}, \quad j = 1, 2, 3 \tag{5.1}$$

and $\mathbf{e}_j$, the unit vector in the direction of the jth cable, is

$$\mathbf{e}_j = \frac{1}{\rho_j}(\mathbf{p} - \mathbf{b}_j). \tag{5.2}$$

The dynamic model is built by considering the force balance on the point-mass end-effector, which yields

$$\sum_{j=1}^{3} -k_j \boldsymbol{\rho}_j + m\mathbf{g} = m\ddot{\mathbf{p}}, \tag{5.3}$$

where $k_j = \frac{f_j}{\rho_j}$.

If the cable attachment points $\{B_j\}_1^3$ are in a plane at the same height and the origin of fixed frame $\mathcal{F}_O$ lies in this plane, the z-component of each vector $\mathbf{b}_j$ is zero, namely $\mathbf{b}_j = [b_{jx}, b_{jy}, 0]^T$. The last component of (5.3) can then be written as

$$\sum_{j=1}^{3} k_j = -\frac{m(\ddot{z} + g)}{z}. \tag{5.4}$$

With this assumption and considering (5.4), the dynamics of the mechanism (5.3) can be rearranged in the following matrix form which is well-suited for point-to-point trajectory planning as shown in Section 5.5.1, as

$$\mathbf{J}\mathbf{k} = m \begin{bmatrix} \ddot{\mathbf{c}} - \frac{(\ddot{z}+g)\mathbf{c}}{z} \\ -\frac{\ddot{z}+g}{z} \end{bmatrix} \tag{5.5}$$

where $\mathbf{c} = [x, y]^T$, $\mathbf{k} = [k_1, k_2, k_3]^T$ and

$$\mathbf{J} = \begin{bmatrix} b_{1x} & b_{2x} & b_{3x} \\ b_{1y} & b_{2y} & b_{3y} \\ 1 & 1 & 1 \end{bmatrix}.$$

Then, the inverse dynamics of the mechanism is obtained from (5.5) as

$$\begin{aligned} \mathbf{k} &= \frac{m\mathbf{J}^{-1}}{z} \begin{bmatrix} z\ddot{\mathbf{c}} - (\ddot{z}+g)\mathbf{c} \\ -(\ddot{z}+g) \end{bmatrix} \\ &= \frac{m\mathbf{v}}{-z\det(\mathbf{J})} \succ \mathbf{0} \end{aligned} \tag{5.6}$$

with

$$\mathbf{v} = \mathrm{Adj}(\mathbf{J}) \begin{bmatrix} (\ddot{z}+g)\mathbf{c} - z\ddot{\mathbf{c}} \\ \ddot{z}+g \end{bmatrix} \tag{5.7}$$

where $\succ$ stands for the componentwise inequality. The three inequality relations in (5.6) are the constraints to be satisfied in order to ensure that the cables remain under tension.

5.3 Basis Motion

A basis motion is designed, which consists of a general mathematical function that can be adapted for each trajectory segment, such that kinematic constraints are respected. This formulation leads to more systematic trajectory planning compared to previous techniques (Gosselin and Foucault, 2014; Jiang and Gosselin, 2016a). It is also well-suited for point-to-point operations, for which kinematic constraints need only be imposed *at the endpoints* and not along each trajectory segment. The basis motion can also be used to produce zero or non-zero acceleration at the end of each trajectory segment, independently in each coordinate direction.

A trajectory $u(t)$ in one dimension is represented by

$$u(t) = \begin{cases} \psi_1(t), & 0 \le t < T_1, \\ \psi_2(t), & T_1 \le t < T_1 + T_2, \\ \quad \vdots & \\ \psi_n(t), & \sum_{i=1}^{n-1} T_i \le t \le \sum_{i=1}^{n} T_i \end{cases} \tag{5.8}$$

where

$$\psi_i(t) = u_i + s_{1i}(t)(u_{i+1} - u_i) + s_{2i}(t)\ddot{\psi}_i(0) \tag{5.9}$$

is the basis motion along segment i, n is the total number of target points, constant $\ddot{\psi}_i(0)$ is the initial acceleration of the ith segment, u_i and u_{i+1} are the initial and final positions for the ith trajectory segment, $s_{1i}(t)$ and $s_{2i}(t)$ are time functions, and T_i is the total time required to complete segment i. In the context of a robot manipulator, u_i could represent a Cartesian position or orientation component, or a joint position. The benefit of using (5.9) is that it facilitates the incorporation of acceleration constraints, as opposed to a general linear trajectory

$$\psi_i(t) = u_i + s_{1i}(t)(u_{i+1} - u_i).$$

Taking the first and second derivatives of (5.9), the velocity and acceleration of $\psi_i(t)$ are obtained

$$\begin{aligned} \dot{\psi}_i(t) &= \dot{s}_{1i}(t)(u_{i+1} - u_i) + \dot{s}_{2i}(t)\ddot{\psi}_i(0), \\ \ddot{\psi}_i(t) &= \ddot{s}_{1i}(t)(u_{i+1} - u_i) + \ddot{s}_{2i}(t)\ddot{\psi}_i(0). \end{aligned} \tag{5.10}$$

Equations (5.9) and (5.10) can represent motions that have zero velocity at both end points and preserve continuity up to the acceleration level, when the constraints in Table 5.1 are respected.

Table 5.1 – Constraints on $s_{1i}(t)$ and $s_{2i}(t)$.

	$s_{1i}(t)$	$s_{2i}(t)$
Position	$s_{1i}(0) = 0,\ s_{1i}(T_i) = 1$	$s_{2i}(0) = s_{2i}(T_i) = 0$
Velocity	$\dot{s}_{1i}(0) = \dot{s}_{1i}(T_i) = 0$	$\dot{s}_{2i}(0) = \dot{s}_{2i}(T_i) = 0$
Acceleration	$\ddot{s}_{1i}(0) = 0$	$\ddot{s}_{2i}(0) = 1$

As shown in Table 5.1, five kinematic constraints are imposed on time function $s_{1i}(t)$ and five separate constraints are imposed on $s_{2i}(t)$. Any functions that can respect these constraints are valid, with two obvious choices being trigonometric and polynomial functions. In particular, cosine functions are a natural choice, since they provide a simple way of imposing zero velocity at the trajectory endpoints. Below, cosine functions are used to produce basis motions for two cases: when the initial acceleration $\ddot{\psi}_i(0)$ is zero, and when it is non-zero.

5.3.1 $\ddot{\psi}_i(0) = 0$

If zero acceleration is imposed at *both* the start and end of a trajectory segment, $\ddot{s}_{1i}(0) = \ddot{s}_{1i}(T_i) = 0$. For this type of motion, $\ddot{\psi}_i(0) = 0$ in (5.9), so $s_{2i}(t)$ does not affect the motion. The main advantage of imposing zero acceleration constraints at both endpoints is that each

segment becomes less affected by preceding segments, which facilitates the trajectory planning process. To achieve this motion, the function

$$s_{1i}(t) = A_i + B_i \cos(\omega_i t) + n_i \cos(3\omega_i t), \tag{5.11}$$

is selected, where the parameters A_{1i}, B_{1i}, n_{1i} and ω_i can be adjusted to meet the constraints. The segment period is given by $T_i = \pi/\omega_i$ so $s_{1i}(t)$ increases monotonically from 0 to 1 and the velocity is zero at both endpoints. Four constraints remain, though the two acceleration constraints are identical, since taking the second derivative of (5.11) leads to

$$\ddot{s}_{1i}(t) = -\omega_i^2(B_{1i} \cos(\omega_i t) + 9n_i \cos(3\omega_i t)), \tag{5.12}$$

and

$$\ddot{s}_{1i}(0) = \ddot{s}_{1i}(1) = -\omega_i^2(B_i + 9n_i) = 0. \tag{5.13}$$

The two acceleration constraints in (5.13) can be combined with the two position constraints $s_{1i}(0) = 0$ and $s_{1i}(T_i) = 1$ to produce

$$A_{1i} = \frac{1}{2}, \quad B_{1i} = -\frac{9}{16}, \quad n_{1i} = \frac{1}{16}$$

and thus $s_{1i}(t)$ is defined by

$$s_{1i}(t) = \frac{1}{2} - \frac{9}{16} \cos(\omega_i t) + \frac{1}{16} \cos(3\omega_i t). \tag{5.14}$$

5.3.2 $\ddot{\psi}_i(0) \neq 0$

The basis motion introduced in Section 5.3.1 with zero-acceleration endpoint constraints is suitable for the z component (direction of gravity). However, the robot cannot reach a point outside the static workspace with zero horizontal acceleration (in x and y). Therefore, for these directions, a second basis motion is introduced below, which maintains acceleration continuity but does not impose zero acceleration at the segment endpoints.

One of the simplest equations that can be used to accomplish this type of motion is

$$s_{1i}(t) = A_{1i} + B_{1i} \cos(\omega_i t) + n_{1i} \cos(2\omega_i t) \in [0, 1], \tag{5.15}$$

where the parameters A_{1i}, B_{1i}, n_{1i} and ω_i can be adjusted to meet the constraints given in Table 5.1. With $t \in [0, T_i]$ and if T_i is selected to be $T_i = \pi/\omega_i$, $s_{1i}(t)$ lies in the range $[0, 1]$ and the zero-velocity endpoint constraints are satisfied. Parameters A_{1i}, B_{1i}, and n_{1i} are used to satisfy the three remaining constraints listed in Table 5.1, while ω_i is left as a design parameter, to be used for selecting dynamically feasible trajectories, as described in Section 5.5.2.

Position constraints are satisfied by selecting

$$A_{1i} = \frac{1}{2} - n_{1i}, \quad B_{1i} = -\frac{1}{2}. \tag{5.16}$$

Then, taking the second derivative of (5.15), one has

$$\ddot{s}_{1i}(0) = -\omega_i^2(B_{1i} + 4n_{1i}) \tag{5.17}$$

so the zero-acceleration constraint is satisfied if $n_{1i} = 1/8$. The function $s_{1i}(t)$ is therefore given by

$$s_{1i}(t) = \frac{3}{8} - \frac{1}{2}\cos(\omega_i t) + \frac{1}{8}\cos(2\omega_i t). \tag{5.18}$$

Following the same procedure, $s_{2i}(t)$ is obtained as

$$s_{2i}(t) = \frac{1}{4\omega_i^2}\left(1 - \cos(2\omega_i t)\right). \tag{5.19}$$

A recursive relationship among the trajectory segments can be identified, since the initial acceleration for one segment must equal the final acceleration of the preceding segment, i.e.,

$$\ddot{\psi}_{i+1}(0) = \ddot{\psi}_i(T_i) = \omega_i^2(u_i - u_{i+1}) + \ddot{\psi}_i(0). \tag{5.20}$$

Substituting (5.20) into the trajectory designed in (5.9), one has

$$\psi_i(t) = (1 - s_{1i}(t) - s_{2i}(t)\omega_{i-1}^2)u_i + s_{1i}(t)u_{i+1} + s_{2i}(t)\omega_{i-1}^2 u_{i-1} + s_{2i}(t)\ddot{\psi}_{i-1}(0). \tag{5.21}$$

This recursive relationship is particularly useful when a target point u_{i+1} cannot be reached without violating dynamic constraints if a single trajectory segment starting from u_{i-1} is used. In this case, (5.21) can be used to help determine the range of allowed values for an intermediate position u_i that allows dynamic constraints to be respected.

Equation (5.20) can also be used for cases where the acceleration at the end of a trajectory must be specified, which is not one of the constraints listed in Table 5.1. For example, when the end-effector is returned to a rest position, the acceleration must be zero. If u_n represents the final position on the trajectory, the zero-acceleration constraint is imposed by setting $\ddot{\psi}_n(T_n) = 0$ and applying (5.20) with $n = i + 1$ to the final two trajectory segments to determine the second-to-last trajectory point

$$u_{n-1} = \frac{(h_{n-1}u_n - u_{n-2})\omega_{n-2}^2 - \ddot{\psi}_{n-2}(0)}{(h_{n-1} - 1)\omega_{n-2}^2}, \tag{5.22}$$

with

$$h_{n-1} = \frac{\omega_{n-1}^2}{\omega_{n-2}^2} \neq 1$$

where u_n, u_{n-2}, and $\ddot{\psi}_{n-2}(0)$ are all known, and h_{n-1} can be determined when ω_{n-2} and ω_{n-1} are specified. The case where $h_{n-1} = 1$, for which u_{n-1} does not affect the final acceleration,

can be avoided by properly selecting ω_{n-2} and ω_{n-1}. Summarizing these results, (5.9), (5.18) and (5.19) can be used to produce segments that ensure continuous acceleration along the entire trajectory, and also to ensure zero velocity and acceleration at the start and end of the trajectory.

The basis motions introduced in this section have several notable advantages compared to previously used techniques. Firstly, position, velocity, and acceleration constraints are satisfied directly by selecting appropriate coefficients for the basis functions, and the recursive relation (5.20) leads to a straightforward procedure for ensuring acceleration continuity. Previously used procedures for these tasks were more complex (Gosselin and Foucault, 2014; Jiang and Gosselin, 2016a). Furthermore, the basis motions can be applied to arbitrary segment endpoints, and can be applied to both the translational and rotational components of trajectories.

5.4 Point-to-Point Trajectory Planning

A point-to-point trajectory is defined by

$$\mathbf{p}(t) = \begin{cases} \boldsymbol{\varrho}_1(t), & 0 \le t < T_1, \\ \boldsymbol{\varrho}_2(t), & T_1 \le t < T_1 + T_2, \\ \quad \vdots & \\ \boldsymbol{\varrho}_n(t), & \sum_{i=1}^{n-1} T_i \le t \le \sum_{i=1}^{n} T_i \end{cases} \tag{5.23}$$

with the constraints that preserve trajectory continuity up to acceleration level for segment i given by

$$\begin{aligned} \boldsymbol{\varrho}_i(0) &= \mathbf{p}_i, \quad \boldsymbol{\varrho}_i(T_i) = \mathbf{p}_{i+1}, \\ \dot{\boldsymbol{\varrho}}_i(0) &= \dot{\boldsymbol{\varrho}}_i(T_i) = \mathbf{0}, \\ \ddot{\boldsymbol{\varrho}}_i(0) &= \ddot{\boldsymbol{\varrho}}_{i-1}(T_{i-1}), \end{aligned} \tag{5.24}$$

where $\mathbf{p}_i$ is a position vector of the ith target point and T_i is the time required to travel from $\mathbf{p}_i$ to $\mathbf{p}_{i+1}$.

For target points that lie beyond the static workspace, non-zero accelerations are required in the x and y directions. Therefore, to satisfy (5.24) in these directions, the basis function with non-zero acceleration at the target point is used, defined by (5.9), (5.18), and (5.19), namely

$$\begin{aligned} \mathbf{c}(t) &= \boldsymbol{\varsigma}_i(t), \quad i = 1, \ldots, n, \\ \boldsymbol{\varsigma}_i(t) &= \mathbf{c}_i + s_{1i}(t)(\mathbf{c}_{i+1} - \mathbf{c}_i) + s_{2i}(t)\ddot{\boldsymbol{\varsigma}}_i(0), \end{aligned} \tag{5.25}$$

where

$$\begin{aligned} s_{1i}(t) &= \frac{3}{8} - \frac{1}{2}\cos(\omega_i t) + \frac{1}{8}\cos(2\omega_i t), \\ s_{2i}(t) &= \frac{1}{4\omega_i^2}\left(1 - \cos(2\omega_i t)\right). \end{aligned}$$

Geometrically, the trajectory in the x–y plane defined in (5.25) can be interpreted in two parts: the first two terms give the desired direction of the motion, which is a straight line from $\mathbf{c}_i$ to $\mathbf{c}_{i+1}$ while the last term represents the deviation from this direction. Clearly, when $\ddot{\boldsymbol{\varsigma}}_i(0) = \mathbf{0}$, the projection of the trajectory in the x–y plane simply represents a straight line. Therefore, the first segment that starts from the state of rest and the last segment that goes back to the state of rest are both straight lines in the x–y plane.

The vectorized version of the recursive relation (5.20) is

$$\ddot{\boldsymbol{\varsigma}}_i(0) = \ddot{\boldsymbol{\varsigma}}_{i-1}(T_i) = \omega_{i-1}^2(\mathbf{c}_{i-1} - \mathbf{c}_i) + \ddot{\boldsymbol{\varsigma}}_{i-1}(0), \tag{5.26}$$

and the vectorized version of (5.22) for finding the intermediate point that allows the robot to return to a state of rest is

$$\mathbf{c}_{n-1} = \frac{\omega_{n-2}^2(h_{n-1}\mathbf{c}_n - \mathbf{c}_{n-2}) - \ddot{\boldsymbol{\varsigma}}_{n-2}(0)}{\omega_{n-2}^2(h_{n-1} - 1)}. \tag{5.27}$$

Additionally, the vectorized version of (5.21), which is the trajectory that is used to obtain intermediate points when $\mathbf{c}_{i+1}$ is prescribed, is

$$\boldsymbol{\varsigma}_i(t) = (1 - s_{1i}(t) - s_{2i}(t)\omega_{i-1}^2)\mathbf{c}_i + s_{1i}(t)\mathbf{c}_{i+1} + s_{2i}(t)\omega_{i-1}^2\mathbf{c}_{i-1} + s_{2i}(t)\ddot{\boldsymbol{\varsigma}}_{i-1}(0). \tag{5.28}$$

Vertical z trajectory segments are prescribed to have zero acceleration at the target points in order to generate natural smooth motion, as described below. The basis motion (5.14) is applied, such that

$$\begin{aligned} z(t) &= \xi_i(t), \quad i = 1, \ldots, n, \\ \xi_i(t) &= s_{1i}(t)(z_{i+1} - z_i), \end{aligned} \tag{5.29}$$

with

$$s_{1i}(t) = \frac{1}{2} - \frac{9}{16}\cos(\omega_i t) + \frac{1}{16}\cos(3\omega_i t).$$

This motion is symmetric from z_i to $E_i = (z_i + z_{i+1})/2$ and from E_i to z_{i+1}, with E_i being the equilibrium point, at which the velocity $\dot{z}$ reaches its maximum and the acceleration $\ddot{z}$ becomes zero. Therefore, in the z direction, the end-effector oscillates around its equilibrium position E_i for one half period during the basis motion, acting like a nonlinear pendulum with just barely enough energy for a full swing.

Equations (5.25) and (5.29) express all three translational directions as functions of the as-yet unspecified frequency ω_i, which can be used to produce many different trajectories that respect the kinematic constraints.

Heuristically, a system operated at or near its natural frequency can have a large amplitude of motion and thereby has a better chance to find feasible points in the point-to-point task. For

example, in (Zoso and Gosselin, 2012), the authors used an estimated natural frequency to achieve large amplitude in point-to-point motions. For fully actuated robots, since trajectories can be designed, it is reasonable to choose a natural frequency that is related to the trajectory. In Chapter 2, it was shown that the natural frequency of the passive system defined by replacing the cable-actuator units with springs is only related to the vertical coordinate of the equilibrium position z_s. According to the symmetry, the motion in the z direction is planned using the natural frequency of the passive system computed at its equilibrium position $z = E_i$ and thus the frequency to be used in (5.25) and (5.29) is chosen as

$$\omega_i = \sqrt{\frac{g}{-E_i}}. \tag{5.30}$$

This frequency is applied in the point-to-point motion to achieve a proper behaviour.

5.5 Experimental Validation

The prototype of a three-DOF CSPR with point-mass end-effector built in Chapter 2 is applied to verify experimentally the proposed trajectory planning scheme. One of the benefits of the proposed technique is the ability to connect target points located outside the static workspace of the robot. This prototype with the mass of the end-effector $m = 0.129\,\mathrm{kg}$ is again shown in Fig. 5.2. A point-to-point motion is demonstrated in a multimedia extension.

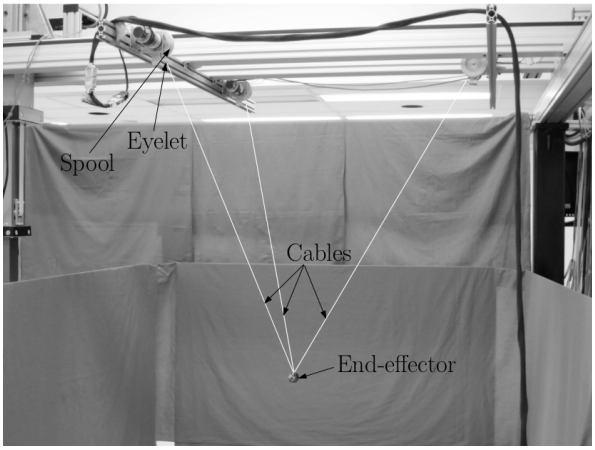

Figure 5.2 – Prototype of a three-DOF CSPR with point mass.

Spools $\{B_j\}_1^3$ form an equilateral triangle, a circle of radius $R = 0.693\,\mathrm{m}$. The vector $\mathbf{b}_j$, connecting the origin to cable attachment point B_j is

$$\mathbf{b}_j = R\,[\cos\theta_j, \sin\theta_j, 0]^T, \quad \theta_j = \frac{2\pi(j-1)}{3}. \tag{5.31}$$

Numerical values for these vectors are provided in Table 2.1. Then, substituting (5.31) into the matrix $\mathbf{J}$, the determinant $\det(\mathbf{J})$ is obtained as

$$\det(\mathbf{J}) = \frac{3R^2}{2}\sqrt{3}. \tag{5.32}$$

The end-effector is assumed to remain below the plane defined by the three attachment points $\{B_j\}_1^3$, i.e., $z < 0$. This assumption is used here and therefore it suffices to use the adjoint matrix in order to determine whether the tensions in the cables are positive. Then, the inequalities (5.6) are simplified as

$$\begin{aligned}\mathbf{v} &= \mathrm{Adj}(\mathbf{J}) \begin{bmatrix} (\ddot{z}+g)\mathbf{c} - z\ddot{\mathbf{c}} \\ \ddot{z}+g \end{bmatrix} \\ &= \begin{bmatrix} \mathbf{N} & \mathbf{u} \end{bmatrix} \begin{bmatrix} (\ddot{z}+g)\mathbf{c} - z\ddot{\mathbf{c}} \\ \ddot{z}+g \end{bmatrix} \\ &= \mathbf{N}((\ddot{z}+g)\mathbf{c} - z\ddot{\mathbf{c}}) + \mathbf{u}(\ddot{z}+g) \succ \mathbf{0},\end{aligned} \tag{5.33}$$

where

$$\mathbf{N} = \frac{1}{3R} \begin{bmatrix} -2 & 0 \\ 1 & -\sqrt{3} \\ 1 & \sqrt{3} \end{bmatrix}, \quad \mathbf{u} = \frac{1}{3} \begin{bmatrix} 1 & 1 & 1 \end{bmatrix}^T. \tag{5.34}$$

are blocks of the adjoint matrix $\mathrm{Adj}(\mathbf{J})$. Therefore, the inequalities in (5.33) are the constraints to be satisfied in order to ensure that the cables remain under tension.

The trajectory segment connecting consecutive points is designed to have a zero instantaneous velocity at its end points as well as to ensure continuity of the accelerations. The defined basis motion, which respects the constraints of starting from the state of rest and can also be used to return to the state of rest at the end of the point sequence, is applied in the point-to-point task. Additionally, it can be conjectured that using the natural frequencies of the linear passive system in the planning of point-to-point motion will facilitate the generation of feasible trajectories. Therefore, the natural frequencies discovered in Chapter 2 are applied to have a proper behaviour. Attainable regions are obtained to search for target points. Feasible regions of intermediate points are generated in cases for which a given point cannot be directly attained.

5.5.1 Attainable Regions and Feasible Regions

Attainable regions of target points and feasible regions of intermediate points for a specific architecture are generated according to the cable tension constraints given in (5.6).

Substituting (5.34), trajectories defined in (5.25) and its second derivatives into inequalities (5.33) yields

$$\mathbf{v} = \mathbf{N}\left(H\mathbf{c}_{i+1} + I\mathbf{c}_i + \boldsymbol{\beta}\right) + \mathbf{u}(g+\ddot{z}) \succ \mathbf{0} \tag{5.35}$$

with

$$\begin{aligned} &H = s_{1i}(t)(g+\ddot{z}) - \ddot{s}_{1i}(t)z, \quad I = (g+\ddot{z})\zeta - z\ddot{\zeta}, \\ &\boldsymbol{\beta} = (s_{2i}(t)(g+\ddot{z}) - \ddot{s}_{2i}(t)z)(\mathbf{c}_{i-1}\omega_{i-1}^2 + \ddot{\boldsymbol{\varsigma}}_{i-1}(0)), \\ &\zeta = 1 - s_{1i}(t) - s_{2i}(t)\omega_{i-1}^2, \end{aligned}$$

where z and $\ddot{z}$ can be written as functions of z_i and z_{i+1} defined in (5.29) and where $\succ$ stands for the componentwise inequality. It is observed that the boundaries of the tension constraints $f_j = 0$ represented in (5.35) with $v_j = 0$, are linear functions of $\mathbf{c}_{i+1}$ and $\mathbf{c}_i$. In the case that $\mathbf{c}_{i+1}$ is unknown, the approach taken here is to prescribe z_{i+1}, i.e., the elevation of the next point to be reached and to determine the attainable region in the (x_{i+1}, y_{i+1}) plane for the prescribed z coordinate, namely z_{i+1}, while satisfying the positive tension constraints.

In order to obtain the attainable region effectively, it is useful to have an intuitive understanding of how the boundaries (the jth-cable tension $f_j = 0$, $j = 1, 2, 3$ by setting (5.35) to be zero) evolve along a given trajectory. At each discretized time and for a prescribed elevation z_{i+1}, an equilateral triangle can be formed, which is an attainable region for (x_{i+1}, y_{i+1}). Indeed, it can be noted from matrix $\mathbf{N}$ that straight line $f_1 = 0$ is always parallel to the y axis while straight lines $f_2 = 0$ and $f_3 = 0$ have constant slopes of $\sqrt{3}/3$ and -$\sqrt{3}/3$, respectively. As shown in Fig. 5.3, the intercepts of the lines defined by setting $f_j = 0$ on the x and y axes are x_{1in}, y_{2in} and y_{3in} while $\mathbf{p}_{i+1}$ represents the centroid of the triangle and the triangles flip in the case of a change of sign of H. The variation of the intercepts characterizes the behaviour of the straight lines associated with $f_j = 0$. At the beginning of the trajectory, $H = 0$ and the intercepts are infinite. As time goes on, for example $H > 0$, the intercepts move closer to each other until maximum values of x_{1in} and y_{2in} as well as a minimum value of y_{3in} are reached. It should be mentioned that these extreme values may not occur at the same time. However, whenever one such condition is reached, the corresponding boundary straight line goes back to infinity. As the sign of H changes, another situation for which $H = 0$ occurs and the intercepts flip at the same time and move closer to each other until the minimum values of x_{1in} and y_{2in} as well as a maximum value of y_{3in} are reached. Throughout the whole trajectory, the attainable region is a combination of all the equilateral triangles defined at each time step. In practice, this can be easily obtained by determining the extreme values of the intercepts. If the sign of H does not change, the region is a minimum equilateral triangle. Otherwise, it is an intersection of the minimum equilateral triangles corresponding to $H > 0$ and $H < 0$ and the resulting region may not be a triangle.

Equation (5.35) can also be used to determine the position of an intermediate point to be inserted between two prescribed points, for instance when point $(i + 1)$ cannot be reached directly from point i. Indeed, the above reasoning can be applied to $\mathbf{c}_i$ when $\mathbf{c}_{i+1}$ is prescribed by considering the sign of I instead of H because (5.35) is a linear function of $\mathbf{c}_i$. Hence, it is possible to determine feasible zones for point i when point $(i + 1)$ is prescribed. This region is similar, as shown in Fig. 5.3.

5.5.2 Experimental Example

It is observed that point-to-point trajectory planning can be greatly simplified when the special frequency of (5.30) is applied. For example, points are located on a horizontal plane, namely

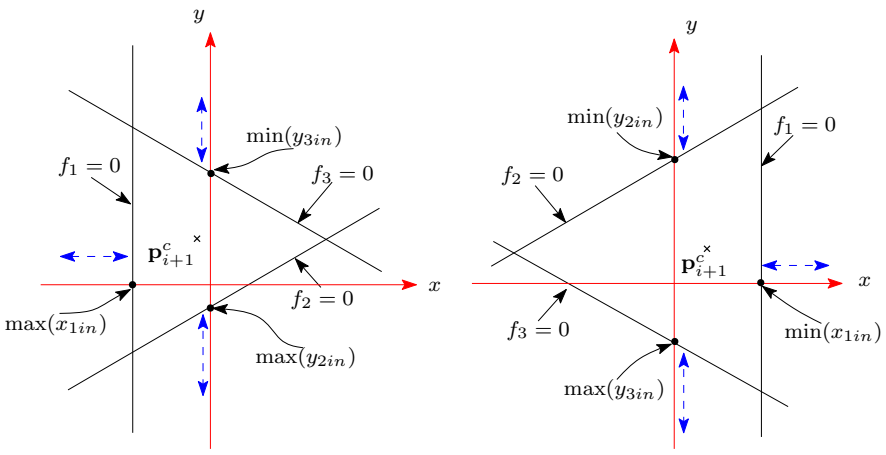

(a) $H < 0$. (b) $H > 0$.

Figure 5.3 – Attainable region for point $i + 1$.

$z = z_s$. After symbolic equation re-arrangement, the feasible region for point $(i + 1)$ is a constant equilateral triangle with its circumradius r as

$$r = \frac{4R}{3} \tag{5.36}$$

and its centre, $\mathbf{p}^c_{i+1} = [x^c_{i+1}, y^c_{i+1}, z_s]^T$, as

$$x^c_{i+1} = -x_i + \frac{2x_1}{3}, \quad y^c_{i+1} = -y_i + \frac{2y_1}{3}. \tag{5.37}$$

where $[x_1, y_1, z_s]^T$, the starting point, have to be located in the region satisfying the inequalities given in (2.17) or within the static workspace.

According to (5.36) and (5.37), the size and position of the attainable region of point $(i + 1)$ can be obtained. Thus, this region can be easily depicted without calculating the cable force inequalities for each point i. Moreover, from (5.37), the centre of the attainable region is symmetric to point i about point $[\frac{2x_1}{3}, \frac{2y_1}{3}, z_s]^T$.

Then, the natural frequency given in (5.30) is applied to all segments of a general trajectory which was tested on the prototype. The trajectory is described as a set of target points in Fig. 5.4. The robot is requested to start from point 1 located on the central axis of the static workspace ($x = y = 0\,\text{m}$, $z = -1.2\,\text{m}$), to proceed to target points (2 to 9) in sequence and finally come back to point 1.

It can be clearly seen from Fig. 5.4 that the robot goes beyond its static workspace. The target points form a star-like shape as shown in Fig. 5.4b, the top view of the trajectory. An intermediate point marked by a star is applied to help the robot to go back to the starting point 1. Moreover, in Fig. 5.4a, since the acceleration in the z direction is prescribed to be zero at the target points, the trajectory segments tend to curve in order to produce soft landings at these points.

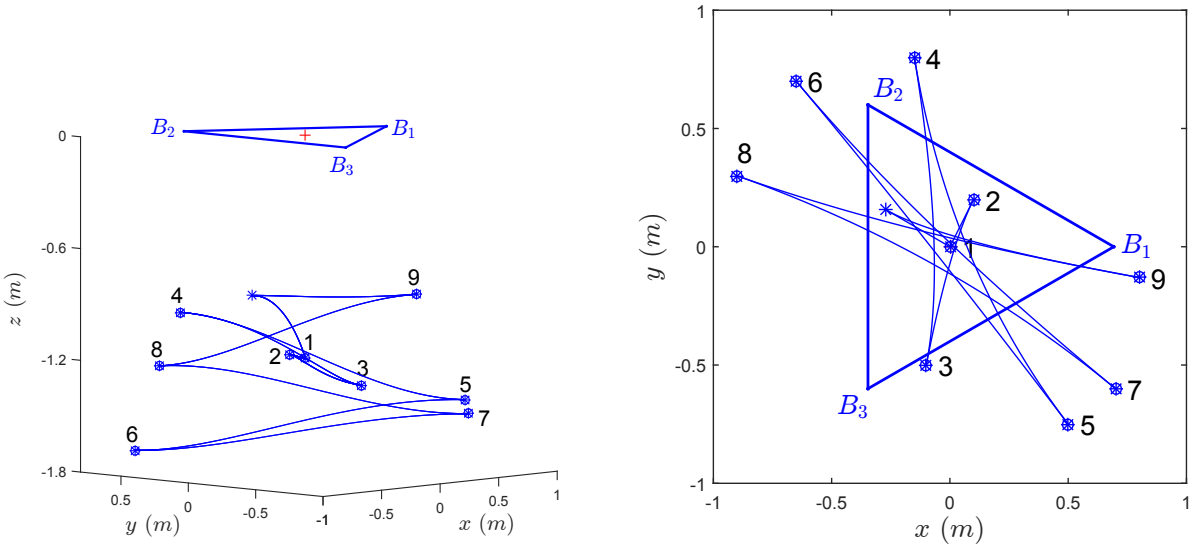

(a) 3D view.

(b) Top view.

Figure 5.4 – Example of a general trajectory.

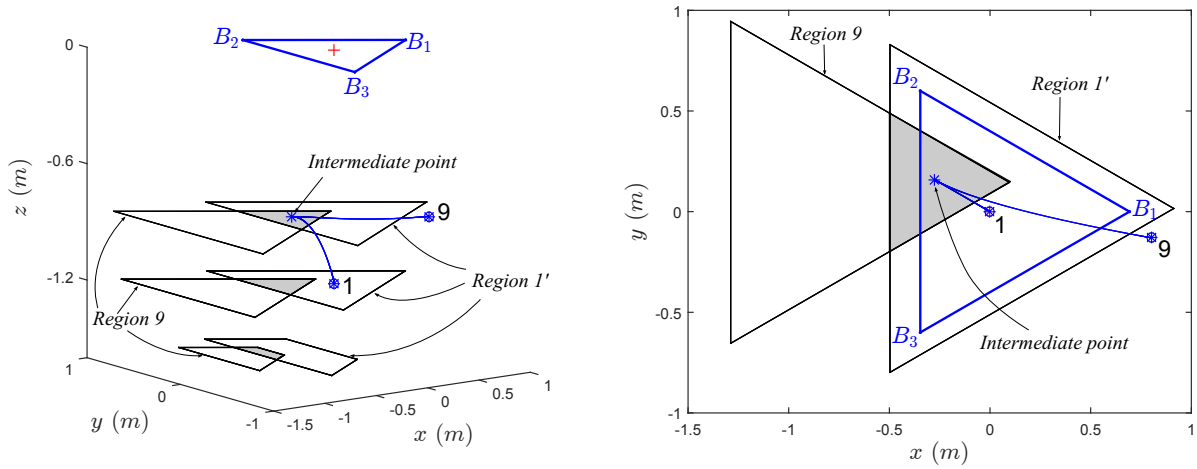

(a) 3D view.

(b) Top view of the $z = -0.855$ m plane.

Figure 5.5 – Returning to the steady final point for a general trajectory.

In Fig. 5.5, the process of returning to the steady final point by adding an intermediate point is demonstrated. Region $1'$ represents the set of points from which point 1 can be attained. This region is obtained using (5.35), in which $\mathbf{c}_{i+1}$ is prescribed. The region obtained is represented in Fig. 5.5a for some arbitrary selected values of z. Region 9 represents the region that can be attained from point 9. It is observed that point 1 is not located in region 9, which means that an intermediate point is necessary. The intermediate point must be located in the intersection of region $1'$ and region 9, as illustrated in Fig. 5.5b, for a chosen value of z.

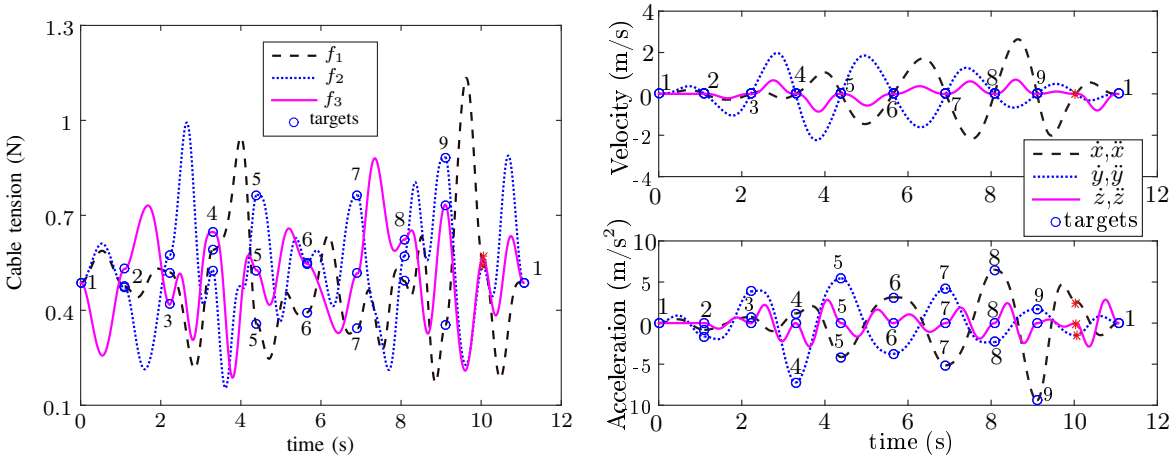

(a) Cable tensions.

(b) Velocities and accelerations.

Figure 5.6 – Cable tensions, Cartesian velocities and accelerations of the general trajectory.

Figure 5.6a shows the results of cable tensions for the example trajectory. It is clear that the cable tensions are continuous and always positive. In Fig. 5.6b, the velocity and acceleration components of the end-effector throughout the sequence of points are illustrated. As prescribed by constructing the trigonometric trajectories, the velocity components are continuous and become zero at the target points. The condition of the continuity of acceleration is met since the components of acceleration are continuous.

5.6 Conclusion

This chapter addresses the dynamic point-to-point trajectory generation for three-DOF CSPRs. The trajectory segments connecting consecutive points are designed to have a zero instantaneous velocity at their end points and must match the initial and final constraints as well as ensure the continuity of the accelerations. Based on the properties of the robot, generic trajectory expressions using a basis formulation and based on proper time function of trigonometric formulations are proposed for the real robot. Using the cable tension constraints, attainable regions are obtained to determine the set of feasible target points. Feasible regions of intermediate points between two consecutive points are also obtained in cases that a given point cannot be directly attained.

An example trajectory is performed by applying the technique proposed to determine the feasible regions. An experimental validation of the trajectory is also demonstrated in the accompanying video. The experiment shows that the expressions based on trigonometric functions used in the point-to-point trajectory planning are feasible, stable and robust.

5.7 Supplementary Data

Extension3-chapter5-point-to-point-3DOF.mp4 —The supplementary video file shows the experimental prototype following a dynamic point-to-point trajectory.

Chapter 6

Dynamic Point-to-Point Trajectory Planning of Six-DOF CSPRs

6.1 Introduction

Most of the CSPR trajectory planning techniques available in the literature for CSPRs are designed for *translational* motion. However, the tilt-and-torsion representation of orientations, along with an analytical method that involves linearizing the dynamic equations were applied in Chapter 4 to produce periodic trajectories with variable orientation. Nevertheless, the rotational component of the trajectories designed in Chapter 4 cannot start and end with zero angular velocity, which is a requirement for many applications and for which a robust representation must be used for interpolation between orientations.

In this chapter, the technique proposed in Chapter 5 is applied for planning trajectories beyond the static workspace of a six-DOF CSPR, using unit quaternion to define the rotational component and the basis motion introduced in Chapter 5. A trajectory to be followed is divided into segments, with each segment being designed to have zero translational and rotational velocity at its endpoints; transitions between segments have translational and rotational acceleration continuity.

The dynamic model of the robot is used for planning the translational and rotational component of each trajectory segment, which ensures that cables always remain in tension. In Section 6.2, the quaternion-based kinematic and dynamic models of the mechanism are obtained. Point-to-point trajectories are designed using basis motion and unit quaternions in Section 6.3. Section 6.4 uses the specific robot architecture introduced in Chapter 4, along with the experimental prototype used to validate the proposed technique, as shown in the supplementary video file.

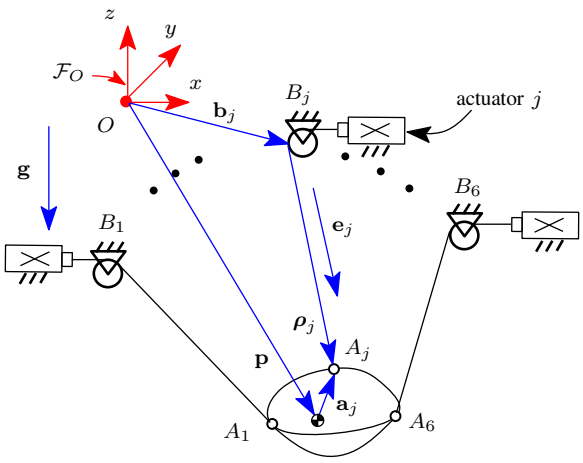

Figure 6.1 – Geometric parameters of a six-DOF cable-suspended parallel robot.

6.2 Mechanics of Six-DOF CSPRs

In this section, the equations that govern the kinematics and dynamics of six-DOF CSPRs are summarized, with a more detailed description provided in Chapter 4. The unit quaternion is integrated with the rotational kinematics by introducing the relation between the time derivatives of quaternion parameters and the angular velocity and acceleration of the end-effector. Additionally, algebraic properties of quaternions related to this work are recalled.

6.2.1 Kinematic and Dynamic Modelling

The general spatial six-DOF CSPR introduced in Chapter 4 is again represented schematically in Fig. 6.1, with the parameters denoted in the introduction of the thesis, unless specified otherwise. Below, indices j should be assumed to go from 1 to 6 and a plural form of an item h_j is denoted $\{h_j\}_1^6$.

The inverse kinematic equations can be written as

$$\boldsymbol{\rho}_j = \mathbf{p} + \mathbf{Q}\mathbf{a}_j - \mathbf{b}_j, \tag{6.1}$$

and the dynamic model of the platform is built using the Newton-Euler approach, which yields

$$\sum_{j=1}^{6} \left(\frac{-f_j}{\rho_j} \boldsymbol{\rho}_j \right) + m\mathbf{g} = m\ddot{\mathbf{p}}, \tag{6.2}$$

$$\sum_{j=1}^{6} (\mathbf{Q}\mathbf{a}_j) \times \left(-\frac{f_j}{\rho_j} \boldsymbol{\rho}_j \right) = \mathbf{I}\dot{\boldsymbol{\omega}} + \boldsymbol{\omega} \times (\mathbf{I}\boldsymbol{\omega}), \tag{6.3}$$

Equations (6.2) and (6.3) can be written in matrix form and the inverse dynamics are obtained as

$$\mathbf{k} = \mathbf{M}^{-1}\boldsymbol{\gamma}, \tag{6.4}$$

where

$$\boldsymbol{\gamma} = \begin{bmatrix} m(\mathbf{g} - \ddot{\mathbf{p}}) \\ \mathbf{I}\dot{\boldsymbol{\omega}} + \boldsymbol{\omega} \times (\mathbf{I}\boldsymbol{\omega}) \end{bmatrix}, \tag{6.5}$$

$$\mathbf{k} = \begin{bmatrix} k_1 & k_2 & k_3 & k_4 & k_5 & k_6 \end{bmatrix}^T, \quad k_j = \frac{f_j}{\rho_j} \tag{6.6}$$

and

$$\mathbf{M} = \begin{bmatrix} \boldsymbol{\rho}_1 & \cdots & \boldsymbol{\rho}_6 \\ (\boldsymbol{\rho}_1 \times \mathbf{Q}\mathbf{a}_1) & \cdots & (\boldsymbol{\rho}_6 \times \mathbf{Q}\mathbf{a}_6) \end{bmatrix}, \tag{6.7}$$

Then, the vector $\mathbf{f}$ of cable tensions is then written as

$$\mathbf{f} = \begin{bmatrix} k_1\rho_1 & k_2\rho_2 & k_3\rho_3 & k_4\rho_4 & k_5\rho_5 & k_6\rho_6 \end{bmatrix}^T. \tag{6.8}$$

6.2.2 The Unit Quaternion and its Derivatives

A unit quaternion is frequently used for rotational trajectory planning in computer graphics, animation, and robotics because it is a nonsingular representation that facilitates interpolation between orientations.

A unit quaternion $\mathbf{q}$, which represents a rotation around a unit axis $\mathbf{n}$ by an angle θ, is written as (Baruh, 1999)

$$\mathbf{q} = [\eta, \boldsymbol{\epsilon}^T]^T \tag{6.9}$$

where

$$\eta = \cos\frac{\theta}{2}, \quad \boldsymbol{\epsilon} = [\epsilon_1, \epsilon_2, \epsilon_3]^T = \mathbf{n}\sin\frac{\theta}{2}, \quad \|\mathbf{q}\| = 1.$$

The two antipodal points $\mathbf{q}$ and $-\mathbf{q}$ represent the same rotation, since a rotation through the angle θ about the axis $\mathbf{n}$ can also be expressed as a rotation through the angle $-\theta$ about the axis $-\mathbf{n}$.

Due to degeneracy when approaching the identity quaternion $\mathbf{q} = [1, 0, 0, 0]^T$, care should be taken when extracting rotation axis and angle from (6.9). The rotation angle θ and rotation axis $\mathbf{n}$ can be obtained according to

$$\theta = 2\,\mathrm{atan2}(\|\boldsymbol{\epsilon}\|, \eta), \quad \mathbf{n} = \frac{\boldsymbol{\epsilon}}{\|\boldsymbol{\epsilon}\|}.$$

When $\theta = 0$, $\mathbf{n}$ can be freely chosen amongst any unit vector in $\mathbb{R}^3$.

A unit quaternion can be used to rotate a vector $\mathbf{w} \in \mathbb{R}^3$ to $\mathbf{w}' \in \mathbb{R}^3$ according to

$$\begin{bmatrix} 0 \\ \mathbf{w}' \end{bmatrix} = \mathbf{q} \begin{bmatrix} 0 \\ \mathbf{w} \end{bmatrix} \mathbf{q}^*, \tag{6.10}$$

where $\mathbf{q}^*$ is the conjugate of $\mathbf{q}$, defined as

$$\mathbf{q}^* = [\eta, -\boldsymbol{\epsilon}^T]^T. \tag{6.11}$$

The rotation matrix that corresponds to a rotation achieved by quaternion multiplication is

$$\mathbf{Q}(\eta, \boldsymbol{\epsilon}) = (\eta^2 - \boldsymbol{\epsilon}^T\boldsymbol{\epsilon})\mathbf{1} + 2\eta\mathbf{S}(\boldsymbol{\epsilon}) + 2\boldsymbol{\epsilon}\boldsymbol{\epsilon}^T, \tag{6.12}$$

where $\mathbf{1}$ is the 3×3 identity matrix and $\mathbf{S}(\boldsymbol{\epsilon})$ is the cross-product matrix of $\boldsymbol{\epsilon}$ (Campa and Camarillo, 2008).

The quaternion time derivative $\dot{\mathbf{q}} = [\dot{\eta}, \dot{\boldsymbol{\epsilon}}^T]^T$ and the angular velocity of the rigid body $\boldsymbol{\omega}$ with respect to the moving frame are related through (Diebel, 2006)

$$\dot{\mathbf{q}} = \frac{1}{2}\mathbf{E}(\mathbf{q})\boldsymbol{\omega}, \tag{6.13}$$

where

$$\mathbf{E}(\mathbf{q}) = \begin{bmatrix} -\boldsymbol{\epsilon}^T \\ \eta\mathbf{1} + \mathbf{S}(\boldsymbol{\epsilon}) \end{bmatrix} \tag{6.14}$$

is the Jacobian matrix, which satisfies the properties

$$\mathbf{E}^T(\mathbf{q})\mathbf{E}(\mathbf{q}) = \mathbf{1}, \quad \mathbf{E}^T(\mathbf{q})\mathbf{q} = \mathbf{0}. \tag{6.15}$$

Consequently, (6.13) can be solved to obtain the angular velocity

$$\boldsymbol{\omega} = 2\mathbf{E}^T(\mathbf{q})\dot{\mathbf{q}}, \tag{6.16}$$

and the angular acceleration

$$\dot{\boldsymbol{\omega}} = 2\mathbf{E}^T(\mathbf{q})\ddot{\mathbf{q}} \tag{6.17}$$

since $\dot{\mathbf{E}}^T(\mathbf{q})\dot{\mathbf{q}} = \mathbf{0}$. Using these values for $\boldsymbol{\omega}$ and $\dot{\boldsymbol{\omega}}$, along with $\mathbf{Q}$ given in (6.12), the inverse dynamics equation (6.4) can be expressed in terms of quaternions.

Below, some basic properties of quaternions are provided; additional details can be found in (Dam et al., 1998). The multiplication of two unit quaternions $\mathbf{q}_1$ and $\mathbf{q}_2$ is defined as

$$\mathbf{q}_1\mathbf{q}_2 = \begin{bmatrix} \eta_1\eta_2 - \boldsymbol{\epsilon}_1^T\boldsymbol{\epsilon}_2 \\ \eta_1\boldsymbol{\epsilon}_2 + \eta_2\boldsymbol{\epsilon}_1 + \mathbf{S}(\boldsymbol{\epsilon}_1)\boldsymbol{\epsilon}_2 \end{bmatrix}. \tag{6.18}$$

Rotational motion is achieved in three steps: (1) the logarithmic map $\ln(\cdot)$ is used to bring the quaternions corresponding to the initial and final pose from $SO(3)$ to $\mathbb{R}^3$, where $SO(3)$ is the group of all rotations about the origin of $\mathbb{R}^3$; (2) interpolation is performed in $\mathbb{R}^3$; (3) the interpolated curve is brought back to $SO(3)$ using the exponential map $\exp(\cdot)$ (Dam et al., 1998; Diebel, 2006). The natural logarithm of a unit quaternion $\mathbf{q}$ is defined as

$$\ln(\mathbf{q}) = \left[0, \mathbf{n}^T\frac{\theta}{2}\right]^T \tag{6.19}$$

and its exponential function maps $\ln(\mathbf{q})$ back to $\mathbf{q}$, since

$$\mathbf{q} = \exp(\ln(\mathbf{q})) = \sum_{i=0}^{\infty}\left(\mathbf{n}\frac{\theta}{2}\right)^i = \left[\cos\frac{\theta}{2}, \mathbf{n}^T\sin\frac{\theta}{2}\right]^T. \tag{6.20}$$

A unit quaternion raised to a real-valued exponent α is also a unit quaternion, since

$$\mathbf{q}^{\alpha} = \exp(\alpha \ln \mathbf{q}) = \left[\cos\left(\frac{\alpha\theta}{2}\right), \mathbf{n}^T \sin\left(\frac{\alpha\theta}{2}\right)\right]^T. \tag{6.21}$$

Finally, a few differential calculus rules are

$$\begin{aligned} &\frac{d}{dt}\mathbf{q}^{v(t)} = \mathbf{q}^{v(t)} \ln(\mathbf{q}) \frac{d}{dt} v(t), \\ &\frac{d}{dt}(\mathbf{q}_1(t)\mathbf{q}_2(t)) = \frac{d\mathbf{q}_1(t)}{dt}\mathbf{q}_2(t) + \mathbf{q}_1(t)\frac{d\mathbf{q}_2(t)}{dt}. \end{aligned} \tag{6.22}$$

These quaternion properties will later be used to show that certain interpolation curves are differentiable.

6.3 Point-to-Point Trajectory Planning

The trajectory planning task is divided into translational and rotational components. Linear interpolation in $\mathbb{R}^3$ is used for the translational component and spherical linear interpolation (SLERP) is used with the unit quaternion representation in $SO(3)$ for the rotational component. The continuous-acceleration basis motion (5.18), (5.19) is used for the x and y directions and the zero-endpoint acceleration motion (5.14) is used for z and the rotational directions, for the reasons discussed in Chapter 5.

Translational Component

The translational component is defined by

$$\mathbf{p}(t) = \begin{cases} \boldsymbol{\varrho}_1(t), & 0 \le t < T_1, \\ \boldsymbol{\varrho}_2(t), & T_1 \le t < T_1 + T_2, \\ \quad \vdots & \\ \boldsymbol{\varrho}_n(t), & \sum_{i=1}^{n-1} T_i \le t \le \sum_{i=1}^{n} T_i \end{cases} \tag{6.23}$$

with the constraints that preserve trajectory continuity up to acceleration level for segment i given by

$$\begin{aligned} &\boldsymbol{\varrho}_i(0) = \mathbf{p}_i, \quad \boldsymbol{\varrho}_i(T_i) = \mathbf{p}_{i+1}, \\ &\dot{\boldsymbol{\varrho}}_i(0) = \dot{\boldsymbol{\varrho}}_i(T_i) = \mathbf{0}, \\ &\ddot{\boldsymbol{\varrho}}_i(0) = \ddot{\boldsymbol{\varrho}}_{i-1}(T_{i-1}), \end{aligned} \tag{6.24}$$

where $\mathbf{p}_i$ is a position vector of the ith target point and T_i is the time required to travel from $\mathbf{p}_i$ to $\mathbf{p}_{i+1}$.

For target points that lie beyond the static workspace, non-zero accelerations are required in the x and y directions. Therefore, to satisfy (6.24) in these directions, the basis function

developed in Section. 5.3.2 is used, defined by (5.9), (5.18), and (5.19), namely

$$\begin{aligned} \mathbf{c}(t) &= \boldsymbol{\varsigma}_i(t), \quad i = 1, \ldots, n, \\ \boldsymbol{\varsigma}_i(t) &= \mathbf{c}_i + s_{1i}(t)(\mathbf{c}_{i+1} - \mathbf{c}_i) + s_{2i}(t)\ddot{\boldsymbol{\varsigma}}_i(0), \end{aligned} \tag{6.25}$$

where $\mathbf{c} = [x, y]^T$ and

$$\begin{aligned} s_{1i}(t) &= \frac{3}{8} - \frac{1}{2}\cos(\omega_i t) + \frac{1}{8}\cos(2\omega_i t), \\ s_{2i}(t) &= \frac{1}{4\omega_i^2}\left(1 - \cos(2\omega_i t)\right). \end{aligned}$$

Geometrically, the trajectory in the x–y plane defined in (6.25) can be interpreted in two parts: the first two terms give the desired direction of the motion, which is a straight line from $\mathbf{c}_i$ to $\mathbf{c}_{i+1}$ while the last term represents the deviation from this direction. Clearly, when $\ddot{\boldsymbol{\varsigma}}_i(0) = \mathbf{0}$, the projection of the trajectory in the x–y plane is simply a straight line. Therefore, the first segment that starts from the state of rest and the last segment that goes back to the state of rest are both straight lines in the x–y plane.

The vectorized version of the recursive relation (5.20) is

$$\ddot{\boldsymbol{\varsigma}}_i(0) = \ddot{\boldsymbol{\varsigma}}_{i-1}(T_i) = \omega_{i-1}^2(\mathbf{c}_{i-1} - \mathbf{c}_i) + \ddot{\boldsymbol{\varsigma}}_{i-1}(0), \tag{6.26}$$

and the vectorized version of (5.22) for finding the intermediate point that allows the robot to return to a state of rest is

$$\mathbf{c}_{n-1} = \frac{\omega_{n-2}^2(h_{n-1}\mathbf{c}_n - \mathbf{c}_{n-2}) - \ddot{\boldsymbol{\varsigma}}_{n-2}(0)}{\omega_{n-2}^2(h_{n-1} - 1)}. \tag{6.27}$$

Additionally, the vectorized version of (5.21), which is the trajectory that is used to obtain intermediate points when $\mathbf{c}_{i+1}$ is prescribed, is

$$\boldsymbol{\varsigma}_i(t) = (1 - s_{1i}(t) - s_{2i}(t)\omega_{i-1}^2)\mathbf{c}_i + s_{1i}(t)\mathbf{c}_{i+1} + s_{2i}(t)\omega_{i-1}^2\mathbf{c}_{i-1} + s_{2i}(t)\ddot{\boldsymbol{\varsigma}}_{i-1}(0). \tag{6.28}$$

Vertical z trajectory segments are prescribed to have zero acceleration at the target points in order to generate natural smooth motion, as described below. The basis motion (5.14) is applied, with

$$\begin{aligned} z(t) &= \xi_i(t), \quad i = 1, \ldots, n, \\ \xi_i(t) &= s_{1i}(t)(z_{i+1} - z_i), \end{aligned} \tag{6.29}$$

and $s_{1i}(t)$ given by (5.14).

This motion is symmetric from z_i to $E_i = (z_i + z_{i+1})/2$ and from E_i to z_{i+1}, with E_i being the equilibrium point, at which the velocity $\dot{z}$ reaches its maximum and the acceleration $\ddot{z}$ becomes zero. Therefore, in the z direction, the end-effector oscillates around its equilibrium

position E_i for one half-period during the basis motion, acting like a nonlinear pendulum with just barely enough energy for a full swing.

Equations (6.25) and (6.29) express all three translational directions as functions of the as-yet unspecified frequency ω_i, which can be used to produce many different trajectories that respect the kinematic constraints. Here, ω_i is chosen to be the *natural frequency* of the system, which allows for a large amplitude of motion and thus provides a better chance for finding feasible points for the point-to-point task, as discussed in (Zoso and Gosselin, 2012). For CSPRs, the natural frequency is related only to the vertical position of the end-effector, which is shown in Chapter 4 through the development of an equivalent passive mass-spring system. For the z motion described by (6.29), the natural frequency at the average vertical position E_i is selected, i.e.,

$$\omega_i = \sqrt{\frac{g}{-E_i}}. \tag{6.30}$$

Rotational Component

The rotational component of the trajectory is also prescribed to have zero acceleration at the segment endpoints to achieve a natural smooth motion that is less affected by other trajectory segments. The rotational component is defined by

$$\mathbf{q}(t) = \begin{cases} \boldsymbol{\zeta}_1(t), & 0 \leq t < T_1, \\ \boldsymbol{\zeta}_2(t), & T_1 \leq t < T_1 + T_2, \\ \quad \vdots & \\ \boldsymbol{\zeta}_n(t), & \sum_{i=1}^{n-1} T_i \leq t \leq \sum_{i=1}^{n} T_i \end{cases} \tag{6.31}$$

with the constraints in quaternion form for each trajectory segment i being

$$\begin{aligned} &\boldsymbol{\zeta}_i(0) = \mathbf{q}_i, \quad \boldsymbol{\zeta}_i(T_i) = \mathbf{q}_{i+1}, \\ &\dot{\boldsymbol{\zeta}}_i(0) = \dot{\boldsymbol{\zeta}}_i(T_i) = \mathbf{0}, \\ &\ddot{\boldsymbol{\zeta}}_i(0) = \ddot{\boldsymbol{\zeta}}_{i-1}(T_{i-1}) = \mathbf{0}. \end{aligned} \tag{6.32}$$

The rotational component is symmetric from $\mathbf{q}_i$ to the mid-point $\mathbf{q}_{i,m} = (\mathbf{q}_i + \mathbf{q}_{i+1})/2$, and from $\mathbf{q}_{i,m}$ to $\mathbf{q}_{i+1}$. Moreover, when the robot reaches $\mathbf{q} = \mathbf{q}_{i,m}$, $\dot{\mathbf{q}}$ reaches its maximum and $\ddot{\mathbf{q}}$ becomes zero. As in the vertical z direction, the rotational components act like nonlinear pendulums with barely enough energy for full swings.

There are an infinite number of paths to transition from $\mathbf{q}_i$ to $\mathbf{q}_{i+1}$. The straightest and shortest such path is a great circle arc along the surface of S^3, which is the unit 3-sphere in four-dimensional Euclidean space. This path can be found using spherical linear interpolation (SLERP), which was first introduced to produce *constant angular velocity* trajectories in (Shoemake, 1985), and has since become widely used in the computer graphics industry (Dam et al., 1998). As depicted in Fig. 6.2, the geometric SLERP formula between $\mathbf{q}_i$ and

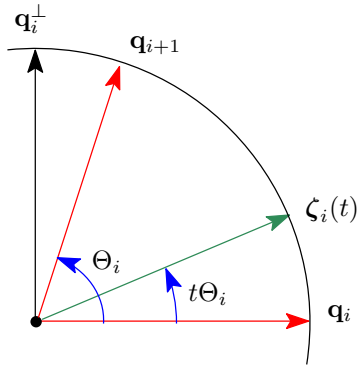

Figure 6.2 – Spherical linear interpolation (SLERP) between two quaternions.

$\mathbf{q}_{i+1}$ and representing the shortest path, is

$$\boldsymbol{\zeta}_i(t) = \frac{\sin[(1-t)\Theta_i]}{\sin\Theta_i}\mathbf{q}_i + \frac{\sin(t\Theta_i)}{\sin\Theta_i}\mathbf{q}_{i+1}, \tag{6.33}$$

with

$$\Theta_i = \frac{\theta_{i,i+1}}{2} \in \left[-\frac{\pi}{2}, \frac{\pi}{2}\right]$$

where $\theta_{i,i+1}$ is the rotation angle for trajectory segment i using quaternions, as defined in (6.9).

An equivalent SLERP formulation is given by

$$\boldsymbol{\zeta}_i(t) = \mathbf{q}_i \exp(t \ln(\mathbf{q}_i^* \mathbf{q}_{i+1})) = \mathbf{q}_i(\mathbf{q}_i^* \mathbf{q}_{i+1})^t. \tag{6.34}$$

Since $\mathbf{q}_i$ and $\mathbf{q}_{i+1}$ are segment endpoint orientations that are not time dependent, the derivative of (6.34) with respect to t, is

$$\dot{\boldsymbol{\zeta}}_i(t) = \boldsymbol{\varphi}_i \boldsymbol{\zeta}_i(t), \tag{6.35}$$

where $\boldsymbol{\varphi}_i = \ln(\mathbf{q}_i^* \mathbf{q}_{i+1})$ yields half the uniform angular velocity vector. Applying (6.11), (6.18) and (6.19), one has

$$\boldsymbol{\varphi}_i = \left[0, \mathbf{n}_{i,i+1}^T \Theta_i\right]^T, \tag{6.36}$$

where $\mathbf{n}_{i,i+1}$ is the rotation axis of the unit quaternion $\mathbf{q}_i^* \mathbf{q}_{i+1}$. This trajectory requires instantaneous acceleration to $\dot{\boldsymbol{\zeta}}_i$ so it cannot be applied directly to a physical system. A modified SLERP is therefore proposed with the linear time function t replaced by higher-order differential functions that can preserve position, velocity, and acceleration continuity. For the basis motion designed in (5.14), the modified SLERP is

$$\boldsymbol{\zeta}_i(t) = \mathbf{q}_i \exp(s_{1i}(t)\boldsymbol{\varphi}_i) \tag{6.37}$$

with

$$s_{1i}(t) = \frac{1}{2} - \frac{9}{16}\cos(\omega_i t) + \frac{1}{16}\cos(3\omega_i t).$$

This motion satisfies the constraints in (6.32) and preserves the geodesic path property. In addition, according to (6.21) and (6.36), one has

$$\exp(s_{1i}(t)\boldsymbol{\varphi}_i) = \left[\cos\left(s_{1i}(t)\Theta_i\right), \mathbf{n}_{i,i+1}^T \sin\left(s_{1i}(t)\Theta_i\right)\right]^T. \tag{6.38}$$

Since (6.38) represents a unit quaternion, (6.18) can be used along with (6.37) to calculate $\boldsymbol{\zeta}_i(t)$. Therefore, the rotational component of the trajectory $\boldsymbol{\zeta}_i(t)$ given in (6.37) can be determined by multiplying $\mathbf{q}_i$ and (6.38) using the multiplication rule for quaternions (6.18). Then, noting that $\boldsymbol{\varphi}_i$ is constant, (6.22) is used to find the quaternion time derivatives.

$$\dot{\boldsymbol{\zeta}}_i(t) = \mathbf{q}_i\boldsymbol{\varphi}_i\dot{s}_i(t)\exp(\boldsymbol{\varphi}_i s_i(t)) = \boldsymbol{\zeta}_i(t)\boldsymbol{\varphi}_i\dot{s}_i(t) \tag{6.39}$$

and

$$\ddot{\boldsymbol{\zeta}}_i(t) = \dot{\boldsymbol{\zeta}}_i(t)\boldsymbol{\varphi}_i\dot{s}_i(t) + \boldsymbol{\zeta}_i(t)\boldsymbol{\varphi}_i\ddot{s}_i(t). \tag{6.40}$$

When $\boldsymbol{\zeta}_i(t)$ and its time derivatives are combined with the corresponding rotation matrix (6.12), the angular velocity (6.16) and angular acceleration (6.17) can be determined and thus the inverse dynamics equation (6.4) in the form of quaternion parameters can be obtained.

6.4 Experimental Validation

The six-DOF CSPR prototype built in Chapter 4 is applied and is again shown in Fig. 6.3 for the validation of the proposed trajectory planning technique. One of the main benefits of this technique is the ability to connect target points located *beyond* the static workspace of the robot.

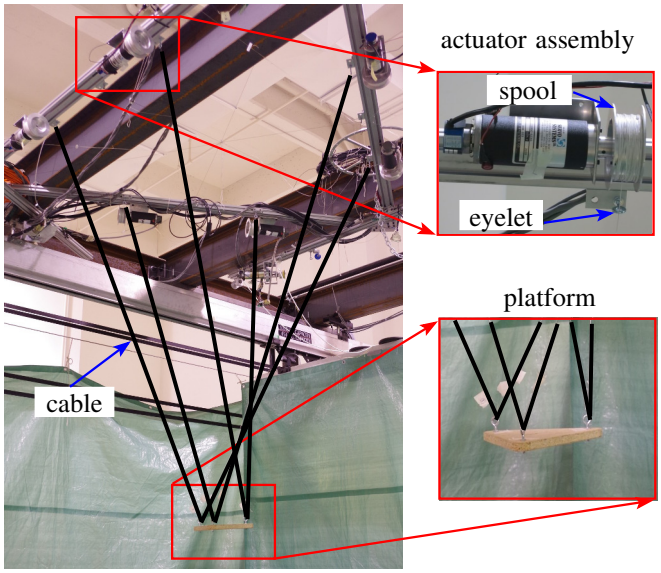

Figure 6.3 – The six-DOF cable-suspended parallel robot prototype.

6.4.1 Geometry of the Prototype

The geometry of the prototype is summarized in the following. Spools $\{B_j\}_1^6$ are evenly distributed on a circle of radius $R = 0.68\,\text{m}$. Cables are connected by pairs to the moving platform, with three attachment points forming an equilateral triangle circumscribed by a circle of radius $r = 0.1\,\text{m}$. The centre of mass C_M is located at a distance d below the geometric centre of the platform attachment points C_G. The mass of the platform is $m = 0.316\,\text{kg}$. The cable attachment vectors, shown in Fig. 6.1, are therefore given by

$$\mathbf{b}_j = R \begin{bmatrix} \cos\beta_{bj} & \sin\beta_{bj} & 0 \end{bmatrix}^T, \tag{6.41}$$

with $\beta_{bj} = \frac{j\pi}{3} - \frac{\pi}{6}$ and

$$\mathbf{a}_j = \begin{bmatrix} r\cos\beta_{aj} & r\sin\beta_{aj} & d \end{bmatrix}^T, \tag{6.42}$$

with $\beta_{aj} = -\frac{2(j-1)\pi}{3} + \frac{\pi}{2}$. Numerical values for these vectors are provided in Tables 4.1 with $d = 0.035$ m.

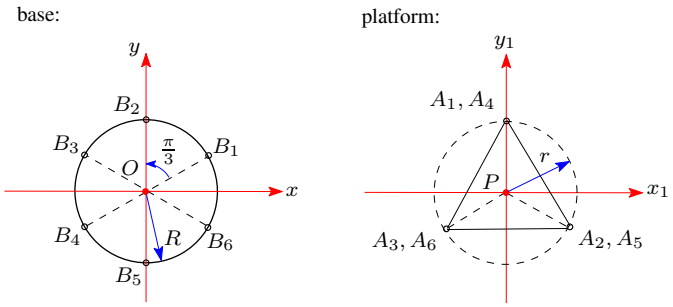

Figure 6.4 – Geometry of the cable attachment points for the six-DOF CSPR prototype.

6.4.2 Experimental Example

An experimental example is provided to demonstrate the trajectory planning scheme proposed above. Cable tension constraints are used to determine the set of feasible target points for each successive trajectory segment. Feasible regions of intermediate points between two consecutive points are obtained for cases where a desired target point cannot be directly attained. A 19-point trajectory is selected that clearly shows the end-effector moving far beyond the edge of the static workspace and also exhibits large changes in orientation.

The feasibility of each trajectory segment is confirmed by verifying that all six cables remain in tension along the entire segment. Substituting the trajectory components defined in (6.25), (6.29) and (6.37) and the recursive relation (6.26) into the inverse dynamics (6.4) yields six inequalities that depend on the pose of two consecutive target points and the trajectory functions between these points, i.e.,

$$\mathbf{k} = \mathbf{k}(\mathbf{p}_i, \mathbf{p}_{i+1}, \mathbf{q}_i, \mathbf{q}_{i+1}, \nu_i(t), s_{2i}(t)) \succ \mathbf{0} \tag{6.43}$$

where $\nu_i(t)$ includes $s_{1i}(t)$ in (5.14) for the vertical component $z(t)$ and rotational component $\mathbf{q}(t)$, as well as $s_{1i}(t)$ in (5.18) for the x and y directions, and $\succ$ stands for the componentwise inequality. The six inequality relations in (6.43) are applied to define a feasible region for point $i+1$ for a trajectory segment starting at point i. Essentially, this process involves finding values of $\mathbf{p}_{i+1}$ and $\mathbf{q}_{i+1}$ that respect a minimum tension requirement for all six cables along the entire trajectory segment.

When point $i+1$ cannot be directly reached from point i, i.e., when no feasible values for $\mathbf{p}_{i+1}$ and $\mathbf{q}_{i+1}$ can be found that respect (6.43), the recursive relation (6.28) is used to search for an intermediate point i. Equation (6.28) can be combined with (6.43) to produce the inequality relations

$$\mathbf{k} = \mathbf{k}(\mathbf{p}_{i-1}, \mathbf{p}_{i+1}, \mathbf{q}_{i-1}, \mathbf{q}_{i+1}, \nu_i(t), s_{2i}(t)) \succ \mathbf{0}, \tag{6.44}$$

which are independent of the point i coordinates $\mathbf{p}_i$ and $\mathbf{q}_i$. Again, the inequalities (6.44) yield a feasible region for i that respects the minimum cable tension constraints. In the experimental example, the final two points on the trajectory are used to demonstrate this intermediate point-finding procedure.

The translational component of the trajectory, defined in (6.25) and (6.29), is applied to connect the set of target points shown in Fig. 6.5. The robot starts at point 1 located at $\mathbf{p} = [0, 0, -1.5]^T$ m, and proceeds to pass through points 2 to 19 in sequence before finally returning to point 1. Each point in the sequence is chosen to be within the feasible region defined by (6.43), and the ratio of maximum-to-minimum tension among the cables is minimized along the entire trajectory to reduce the chance of losing cable tension due to experimental and control error.

It can be clearly observed in Fig. 6.5 that the end-effector reaches points outside its static workspace. The target points form a star-like shape when viewed from above, as shown in Fig. 6.5c. Moreover, since the acceleration in the z direction is prescribed to be zero at the target points, the trajectory segments are shaped in S.

The platform orientation is represented using the T&T angle convention, which provides an intuitive and compact visualization for the orientation of a parallel robot (Bonev et al., 2002). In this convention, the azimuth angle is ϕ, tilt angle is θ, and torsion angle is σ. The torsion angle σ is set to zero at target points because a CSPR can generally perform little torsional motion before cable interferences occur. Under this assumption, the vector representing the axis of rotation is

$$\mathbf{n}_i = \begin{bmatrix} \cos\phi_i & \sin\phi_i & 0 \end{bmatrix}^T \tag{6.45}$$

and the corresponding unit quaternion $\mathbf{q}_i$ is given by (6.9). The fourth component of the unit quaternion ϵ_3 is therefore zero at the target points and remains zero along the trajectory segments when using the spherical linear interpolation defined in (6.33). Furthermore, since

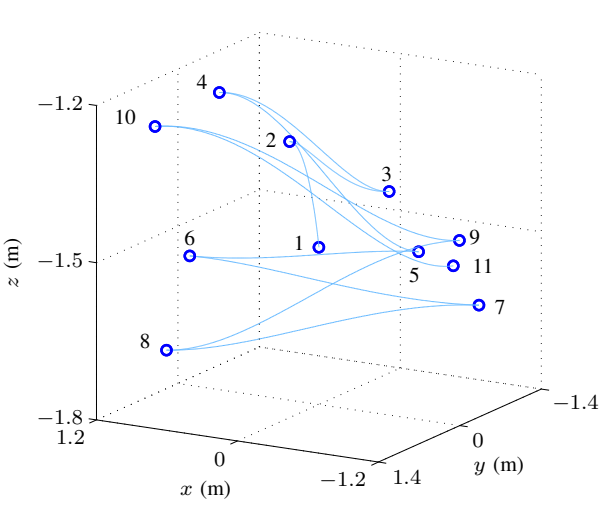

(a) 3D view (point 1 to point 11).

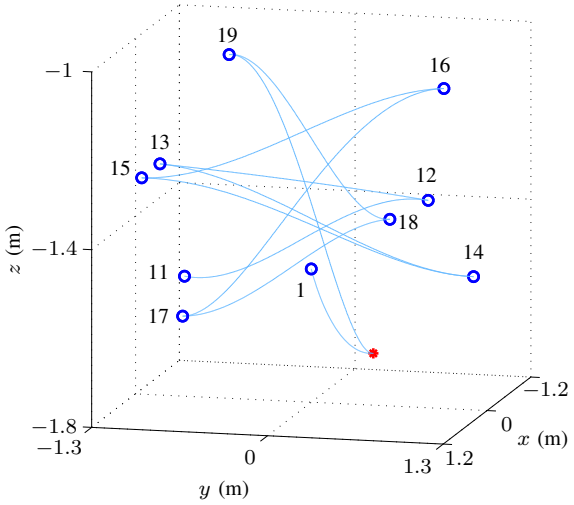

(b) 3D view (point 11 to end point).

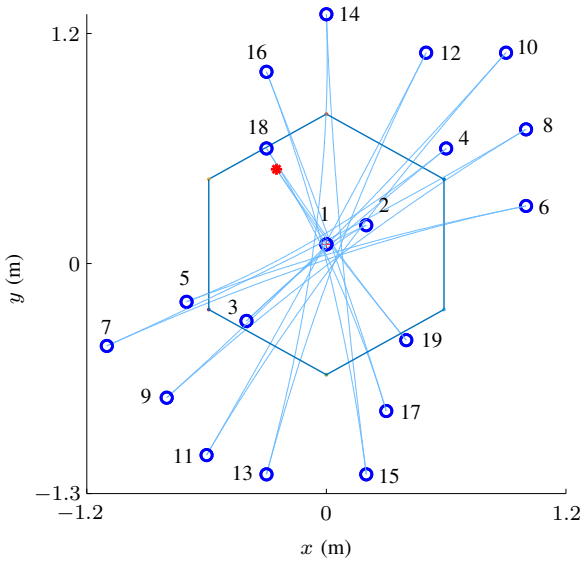

(c) Top view.

Figure 6.5 – Translational component of the test trajectory (Marker ∘ represents target points while ∗ represents an intermediate point).

$\epsilon_3 = 0$, the rotational trajectories can be visualized on a unit sphere in S^2 with the coordinates $(\eta, \epsilon_1, \epsilon_2)$, as shown in Fig. 6.6a.

The initial orientation at point 1 is $\theta = 0$, which corresponds to the identity quaternion $[1, 0, 0, 0]^T$. Trajectory points 8, 10, 13, 16, and 19, which are not shown in the figure, have the same orientation as point 1. It can be clearly seen that the orientation along the trajectory is well interpolated, which is expected with the quaternion representation being singularity-free. The platform pose is illustrated at several trajectory points in Fig. 6.6c to provide a more intuitive depiction of the orientation changes. The cable tensions remain positive and

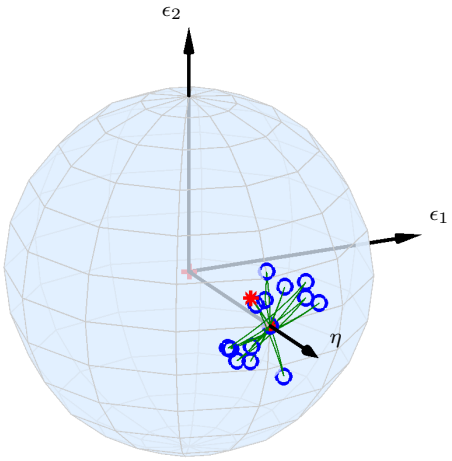

(a) A projection onto the unit sphere in S^2 for three of the four components of the unit quaternion $\mathbf{q}$.

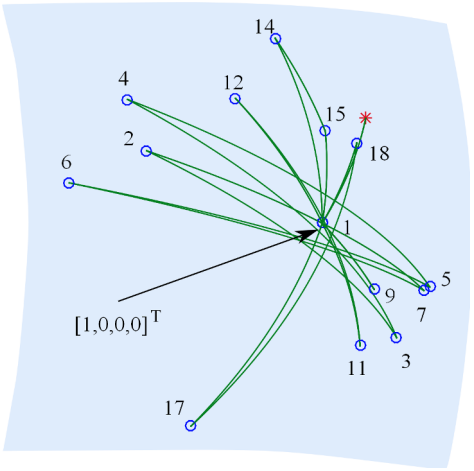

(b) A closer view of the trajectory shown in (a).

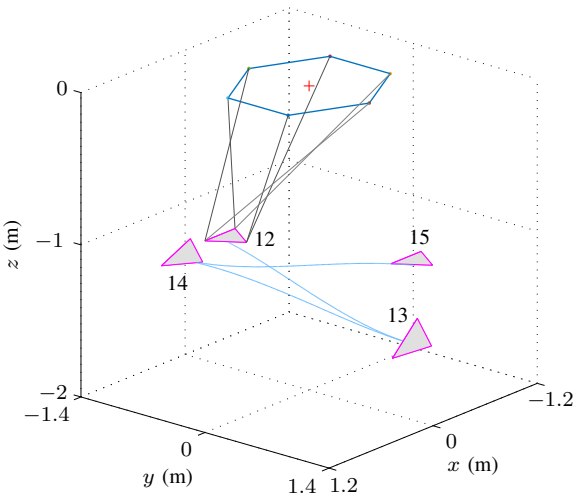

(c) A 3D representation of some trajectory segments, with the end-effector pose shown at the segment end-points.

Figure 6.6 – The rotational component of the 19-point trajectory. Marker ∘ represents target points while ∗ represents an intermediate point.

continuous along the entire trajectory, as shown in Fig. 6.7.

As shown in Fig. 6.5, an intermediate point is used on the 19-point trajectory in between the final two points. This is a special case because the acceleration at the final point is zero. Under this zero-acceleration constraint, if z_* is specified, x_* and y_* can be found using (6.27) and (6.30). Rather than exploiting this simplification, however, the general procedure is shown below, which can be applied to find any intermediate point.

In Fig. 6.8, Region 19 represents the set of points that can be reached from point 19, while

respecting positive tension constraints. Region 1 represents a similar set of points from which a trajectory segment must start in order to reach point 1. Clearly, point 1 does not lie within the feasible region for point 19, and point 19 does not lie within the feasible region for point 1, thereby confirming that an intermediate point is necessary.

A general feasible region consists of a six-dimensional enclosed surface with coordinates in x, y, z, θ, ϕ, and σ. However, σ_i is always zero, to minimize torsion of the end-effector. Additionally, ϕ_i is chosen such that the axis $\mathbf{n}_i$ in (6.45) is aligned with the position vector $(x_i, y_i, 0)$. Finally, z_* is prescribed. Under these assumptions, the remaining unknown coordinates for the intermediate point are x_*, y_*, and θ_*. A three-dimensional grid in these coordinates is formed, and for each point on the grid, the associated trajectory segments from point 19 to * and * to 1 are formed. Each segment is discretized and tension constraints are verified by solving the inverse dynamics equation (6.4). The two regions found with this procedure are shown three dimensionally in Fig. 6.8a, with a slice at $\theta = 0.4$ rad shown in Fig. 6.8b. The intermediate point must lie within the intersection of Regions 1 and 19; the specific point within this intersection is chosen as that which reduces the ratio between the maximum and minimum cable tensions. In practice, this objective provides a better margin for maintaining taut cables than the simpler objective of maximizing the minimum cable tension. The coordinates of this point are

$$(x, y, z, \theta, \phi, \sigma) = (-0.25, 0.3, -1.7, 0.4, 2.14, 0) \tag{6.46}$$

with linear coordinates in metres and angular coordinates in radians.

As mentioned above, a simpler approach could be applied to find this specific intermediate point because it lies between the final two trajectory points. Using this approach, two additional constraints can be applied because the acceleration in x and y must be zero at the end

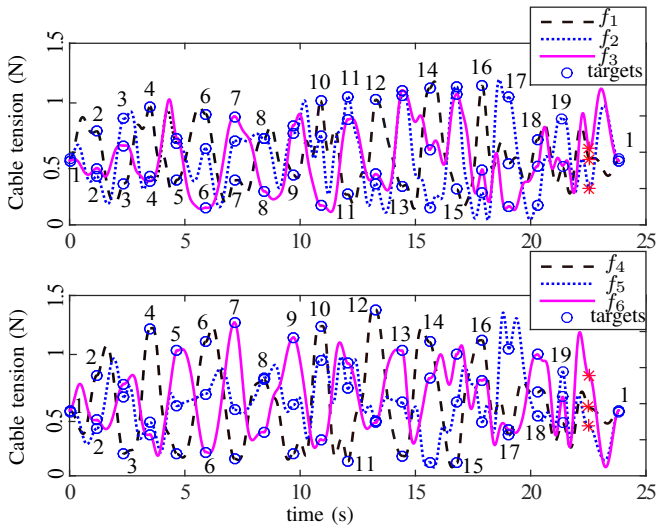

Figure 6.7 – Cable Tensions along the 19-point trajectory.

of the trajectory. In turn, this leads to a problem with only three independent coordinates for point *, namely z_*, θ_*, and ϕ_*. Finally, if z_* and ϕ_* are defined as in the general case described above, only the θ_* is left to be found.

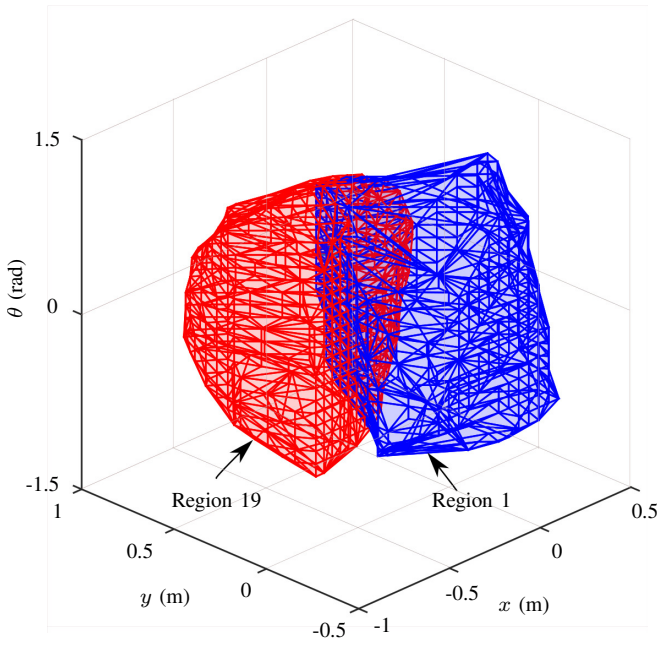

(a) 3D view.

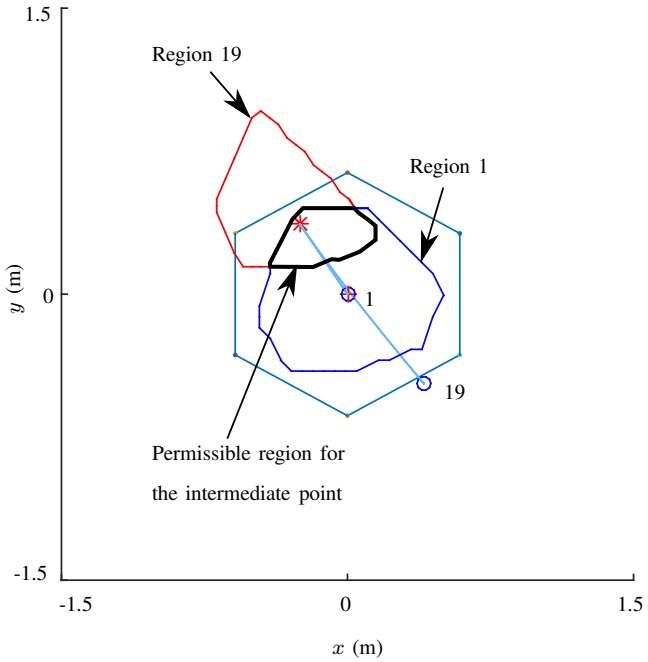

(b) Top view with $\theta = 0.4$ rad.

Figure 6.8 – Determination of an intermediate point between the final two trajectory points. When this point lies within the permissible region, the trajectory segments from 19 to $*$ and $*$ to 1 are guaranteed to be dynamically feasible, i.e., cable tensions will always remain positive.

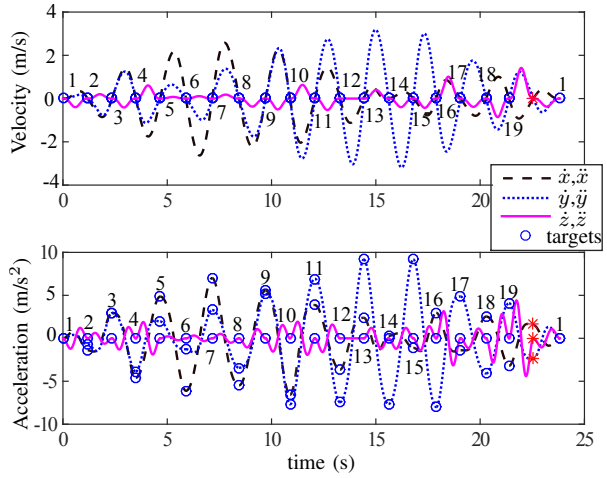

(a) Translational velocities and accelerations.

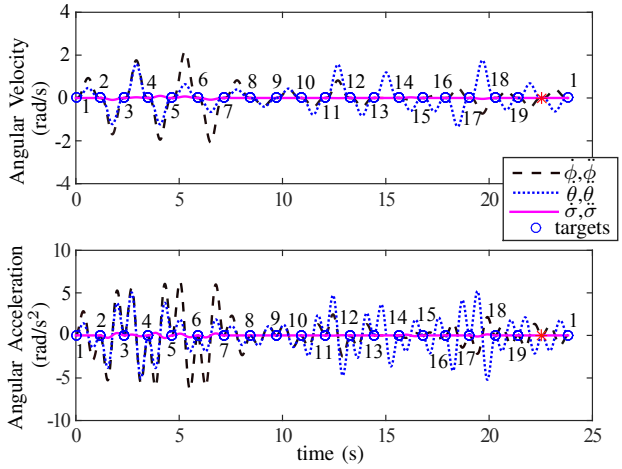

(b) Angular velocities and accelerations

Figure 6.9 – Velocities and accelerations along the 19-point trajectory.

In Fig. 6.9, the translational and angular velocities and accelerations of the end-effector throughout the sequence of points are plotted. As prescribed during construction of the basis motions, the translational and angular velocities are zero at every target point. Additionally, the z acceleration and all three angular acceleration components are zero at the target points, as prescribed, and all accelerations are continuous along the entire trajectory. This figure also demonstrates that the angular velocity and acceleration for the torsion angle σ are not always zero, which is expected since the zero-torsion-angle constraint is only imposed at the target points.

6.5 Conclusion

The main contribution of this chapter is the introduction of a dynamic trajectory planning technique that permits a six-DOF cable-suspended parallel robot to reach a series of target points *outside* its static workspace in a controlled, predictable manner.

Trajectory segments are planned one at a time, using the basis motion which is a simplified segment function. A straightforward procedure for imposing kinematic constraints is designed. Quaternions, which are singularity-free and which are the preferred representation for interpolating between large changes in orientation, are used to describe the rotational component. Dynamic constraints are verified for all trajectory segments and a procedure for searching for intermediate points is provided for cases where this verification fails.

6.6 Supplementary Data

Extension4-chapter6-point-to-point-6DOF.mp4 —The supplementary video file shows the experimental prototype following a dynamic point-to-point trajectory. Initially, the platform is moved slowly in a horizontal direction until one of the cables is clearly sagging, thereby showing the approximate edge of the static workspace. Then, an example trajectory involving the interpolation of both position and orientation along a sequence of 19 points is shown.

Part III

Dynamic Transition Trajectory Planning

Chapter 7

Dynamic Transition Trajectory Planning of Three-DOF CSPRs

7.1 Introduction

Although specific trajectories can be generated separately, in a real application the robot is required to move from one trajectory to the next in order to automatically chain multiple pre-generated trajectories with different starting points. Therefore, the goal of this chapter is to plan such feasible transition trajectories with positive cable tensions at all times. In particular, the transition trajectory is designed to connect any two or multiple periodic trajectories, obtained in Chapter 2, in sequence. Since these target trajectories can extend beyond the static workspace of the robot and do not include points representing the state of rest, the transition trajectories must be capable of extending beyond the static workspace, as well as having the ability to start from/end with a resting position. In the proposed scheme, the source and goal trajectories are blended with a transition trajectory that increasingly adapts the parameters to those of the goal trajectory, as illustrated in Fig. 7.1. The transition trajectory begins as the robot leaves the source trajectory at point *start* and ends as the robot merges into the goal trajectory at point *arrival*.

The rest of the chapter is arranged as follows. In Section 7.2, the kinematic and dynamic models of the mechanism are presented. Section 7.3 introduces the novel transition trajectory planning technique. Section 7.4 provides example trajectories and results.

7.2 Kinematic and Dynamic Modelling

As illustrated in Fig. 7.2, the spatial three-DOF CSPR with three cables and a point mass end-effector built in Chapter 2 is again applied to the generation of transition trajectories, with the symbols denoted in the introduction of the thesis, unless specified otherwise. One

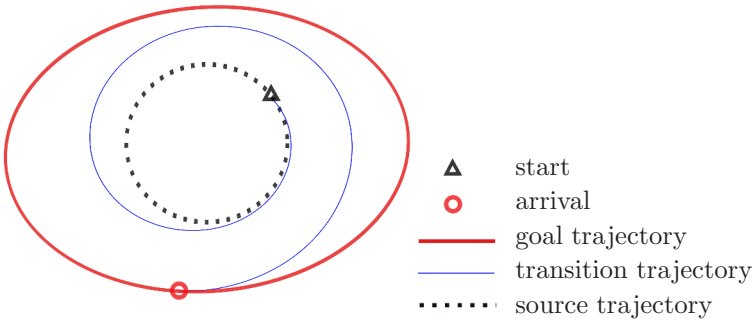

Figure 7.1 – Blending source and goal trajectories with a transition trajectory that increasingly adapts the parameters to those of the goal trajectory.

of the benefits of the proposed technique is the ability to chain multiple target trajectories located beyond the static workspace of the robot in sequence. Below, indices j should be assumed to go from 1 to 3 and a plural form of an item h_j is denoted $\{h_j\}_1^3$.

The kinematics and dynamics of this mechanism is recalled from Chapter 2. The inverse kinematic equations can be written as

$$\boldsymbol{\rho}_j = \mathbf{p} - \mathbf{b}_j. \tag{7.1}$$

The unit vector in the direction of the jth cable and oriented from the pulley to the end-effector $\mathbf{e}_j$ is

$$\mathbf{e}_j = \frac{1}{\rho_j}(\mathbf{p} - \mathbf{b}_j). \tag{7.2}$$

The dynamic model is built by considering the force balance on the point mass end-effector,

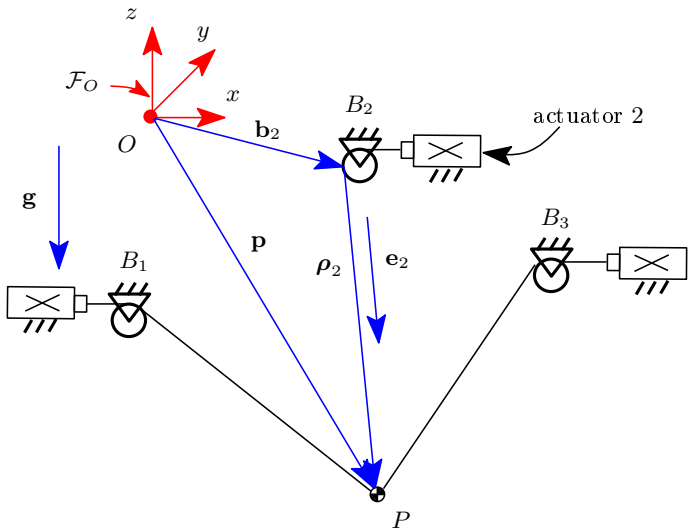

Figure 7.2 – A spatial three-DOF CSPR with point-mass.

which yields

$$\sum_{j=1}^{3} -k_j \boldsymbol{\rho}_j + m\mathbf{g} = m\ddot{\mathbf{p}}, \tag{7.3}$$

with

$$k_j = \frac{f_j}{\rho_j}, \quad j = 1, 2, 3.$$

The dynamic equation (7.3) can be considered as a system of three linear equations in three unknowns (k_j): one can explicitly solve for k_j, according to a specific architecture.

The specific architecture applied in Chapter 2 is that the cable attachment points $\{\mathbf{b}_j\}_1^3$ form an equilateral triangle with circumradius R and are located at the same height, i.e., in a horizontal plane. One then has

$$\mathbf{b}_j = R\left[\cos\beta_j, \sin\beta_j, 0\right]^T, \quad \beta_j = \frac{2\pi(j-1)}{3}. \tag{7.4}$$

Substituting the above geometric parameters into (7.3), one can explicitly solve for k_j yielding

$$k_j = -\frac{m}{3Rz} k'_j > 0, \tag{7.5}$$

where $z < 0$ and

$$\begin{aligned} k'_1 &= (2x + R)(g + \ddot{z}) - 2z\ddot{x} > 0, \\ k'_2 &= (-x + \sqrt{3}y + R)(g + \ddot{z}) + z(\ddot{x} - \sqrt{3}\ddot{y}) > 0, \\ k'_3 &= (-x - \sqrt{3}y + R)(g + \ddot{z}) + z(\ddot{x} + \sqrt{3}\ddot{y}) > 0. \end{aligned} \tag{7.6}$$

The above inequalities represent the constraints to be satisfied in order to ensure that the cables remain under tension. Since the first factor $-\frac{m}{3Rz}$ of (7.5) is always positive under the assumption that the platform remains *suspended*, i.e., $z < 0$, inequalities (7.5) are automatically satisfied when inequalities (7.6) are satisfied. Therefore, if inequalities (7.6) are satisfied at all points of a given trajectory, it can be guaranteed that the cables will remain under tension throughout the trajectory. These conditions are necessary and sufficient.

7.3 Transition Trajectory Planning

Transition trajectories that can automatically chain multiple feasible target trajectories in sequence with different starting points are developed. This trajectory is generated by combining two consecutive target trajectories, considered as source and goal trajectories for each transition, with a proper time function. As a result, the goal trajectory is gradually reached by changing parameters from that of the source trajectory. As illustrated in Fig. 7.3, the robot follows a source trajectory since its arrival and until the departure for a goal trajectory while starting the transition at a proper starting point. It is obvious that the preparation stage for

transition is guaranteed to be feasible, since the robot is following the source trajectory during which cable tensions remain positive at all times.

Mathematically, such a procedure for the preparation stage is given as

$$\mathbf{p}(t) = \mathbf{p}_i(t), \quad 0 \leq t \leq \delta_i, \tag{7.7}$$

and for the transition given as

$$\mathbf{p}(t) = \mathbf{p}_i(t) + U(\tau)\mathbf{s}_i(t), \quad \delta_i \leq t \leq T_i + \delta_i, \quad 0 \leq \tau \leq 1, \tag{7.8}$$

where $\mathbf{p}_i(t)$ represents trajectory i, $\mathbf{s}_i(t) = \mathbf{p}_{i+1}(t - \delta_i) - \mathbf{p}_i(t)$, $U(\tau) \in [0, 1]$, with

$$U(0) = 0, \quad U(1) = 1, \tag{7.9}$$

is an increasingly monotonous time function with $\tau = (t - \delta_i)/T_i$ whereas δ_i, a time offset, is the departure time, T_i is the total transitioning time from $\mathbf{p}_i(t)$ to $\mathbf{p}_{i+1}(t)$, and there is no time offset for $\mathbf{p}_{i+1}(t)$. Therefore, the transition trajectory depends only on two parameters, the departure time (δ_i) from the source trajectory and the total transition time (T_i) until arrival at the goal trajectory. The values of the two parameters can be adjusted to obtain optimal transition trajectories.

Taking the first three derivatives of the transition trajectory (7.8) with respect to time, yields

$$\begin{aligned}
\dot{\mathbf{p}}(t) &= \dot{U}(\tau)\mathbf{s}_i(t) + \dot{\mathbf{p}}_i(t) + U(\tau)\dot{\mathbf{s}}_i(t), \\
\ddot{\mathbf{p}}(t) &= \ddot{U}(\tau)\mathbf{s}_i(t) + 2\dot{U}(\tau)\dot{\mathbf{s}}_i(t) + \ddot{\mathbf{p}}_i(t) + U(\tau)\ddot{\mathbf{s}}_i(t), \\
\dddot{\mathbf{p}}(t) &= \dddot{U}(\tau)\mathbf{s}_i(t) + 3\ddot{U}(\tau)\dot{\mathbf{s}}_i(t) + 3\dot{U}(\tau)\ddot{\mathbf{s}}_i(t) + \dddot{\mathbf{p}}_i(t) + U(\tau)\dddot{\mathbf{s}}_i(t).
\end{aligned} \tag{7.10}$$

where $\dot{U}(\tau)$, $\ddot{U}(\tau)$, $\dddot{U}(\tau)$ are the first three derivatives of $U(\tau)$ with respect to time. Thus, the continuity of $\mathbf{p}(t)$ can be preserved up to the acceleration level with (7.9) and the following constraints on $\dot{U}(\tau)$ and $\ddot{U}(\tau)$, namely

$$\dot{U}(0) = \dot{U}(1) = 0, \quad \ddot{U}(0) = \ddot{U}(1) = 0. \tag{7.11}$$

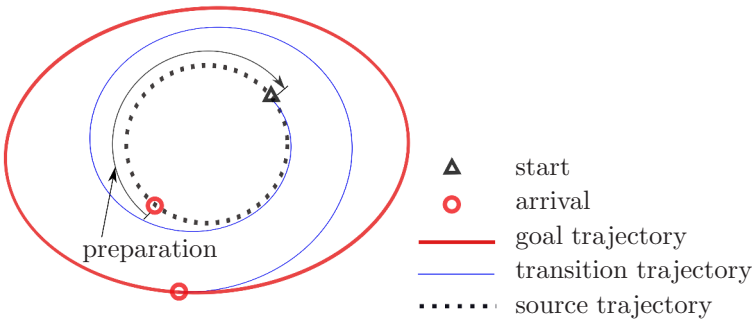

Figure 7.3 – Transition trajectory planning with preparation stage.

Indeed, according to (7.9) and (7.11), the first two rows of (7.10) become

$$\begin{aligned}\dot{\mathbf{p}}(\delta_i) &= \dot{\mathbf{p}}_i(\delta_i), \quad \dot{\mathbf{p}}(T_i+\delta_i) = \dot{\mathbf{p}}_{i+1}(T_i),\\ \ddot{\mathbf{p}}(\delta_i) &= \ddot{\mathbf{p}}_i(\delta_i), \quad \ddot{\mathbf{p}}(T_i+\delta_i) = \ddot{\mathbf{p}}_{i+1}(T_i).\end{aligned}$$

Additionally, in some cases where the continuity of the jerk is required to yield smooth accelerations/cable forces of the robot, i.e.,

$$\dddot{\mathbf{p}}(\delta_i) = \dddot{\mathbf{p}}_i(\delta_i), \quad \dddot{\mathbf{p}}(T_i+\delta_i) = \dddot{\mathbf{p}}_{i+1}(T_i), \tag{7.12}$$

the corresponding constraints can also be found. Substituting (7.9) and (7.11) into the last row of (7.10) yields the value of the jerk at both ends of a transition trajectory, which is

$$\begin{aligned}\dddot{\mathbf{p}}(\delta_i) &= \dddot{U}(0)\mathbf{s}_i(\delta_i) + \dddot{\mathbf{p}}_i(\delta_i),\\ \dddot{\mathbf{p}}(T_i+\delta_i) &= \dddot{U}(1)\mathbf{s}_i(T_i+\delta_i) + \dddot{\mathbf{p}}_{i+1}(T_i).\end{aligned} \tag{7.13}$$

Thus, according to (7.13), the requirement for respecting (7.12) can be readily obtained, namely

$$\dddot{U}(0) = \dddot{U}(1) = 0. \tag{7.14}$$

In summary, transition trajectories with continuity up to the acceleration level can be obtained according to (7.8), with proper time function $U(\tau)$ while respecting (7.9) and (7.11). Moreover, for preserving the continuity of the jerk, an additional requirement (7.14) should also be respected.

7.4 Example

An example is given to demonstrate the transition trajectory technique proposed above. In this example, the robot transitions between the feasible periodic trajectories that were generalized in Chapter 2. Two elementary time functions $U(\tau)$ are applied to generate the transition trajectory defined in (7.8), including the standard 5-th degree polynomial function and the 7-th degree polynomial function. Then, an optimal combination of the parameters δ_i and T_i are obtained, such that the cable tensions remain positive along the trajectory, and the execution time is as small as possible.

7.4.1 Time Function $U(\tau)$

Two elementary time functions $U(\tau)$ based on polynomials are applied to generate the transition trajectory defined in (7.8). The standard 5-th degree polynomial trajectory which can ensure the continuity up to the acceleration level, proposed in (Gosselin and Hadj-Messaoud, 1993), is first introduced. This time function and its first three derivatives are recalled, namely

$$\begin{aligned}U(\tau) &= 6\tau^5 - 15\tau^4 + 10\tau^3, \quad \dot{U}(\tau) = (30\tau^4 - 60\tau^3 + 30\tau^2)/T_i,\\ \ddot{U}(\tau) &= (120\tau^3 - 180\tau^2 + 60\tau)/T_i^2, \quad \dddot{U}(\tau) = (360\tau^2 - 360\tau + 60)/T_i^3,\end{aligned} \tag{7.15}$$

which meets the constraints given in (7.9) and (7.11). However, there exists discontinuities of the jerk at both ends of the trajectory since

$$\dddot{U}(0) = \dddot{U}(1) = 60/T_i^3, \tag{7.16}$$

which implies that the minimization of the trajectory time T_i increases the jerk.

Then, the 7-th degree polynomial trajectory with third derivative continuity, proposed in (Gosselin and Hadj-Messaoud, 1993), is applied as an alternative. This time function and its first three derivatives are recalled, namely

$$\begin{aligned}
U(\tau) &= -20\tau^7 + 70\tau^6 - 84\tau^5 + 35\tau^4, \\
\dot{U}(\tau) &= (-140\tau^6 + 420\tau^5 - 420\tau^4 + 140\tau^3)/T_i, \\
\ddot{U}(\tau) &= (-840\tau^5 + 2100\tau^4 - 1680\tau^3 + 420\tau^2)/T_i^2, \\
\dddot{U}(\tau) &= (-4200\tau^4 + 8400\tau^3 - 5040\tau^2 + 840\tau)/T_i^3,
\end{aligned} \tag{7.17}$$

which satisfies the constraints given in (7.9) and (7.11). It can be readily seen from the latter time function that the jerk is smooth at both ends of the trajectory since (7.14) is respected.

7.4.2 Transition between Periodic Trajectories

Based on (7.7) and (7.8), transition with its preparation stage between a sequence of periodic trajectories is demonstrated. Periodic trajectories obtained in Chapter 2 are briefly recalled. The CSPR is equivalent to a passive mechanical system, obtained by replacing the actuator-cable units with linear constant-stiffness springs. Applying (7.1), its dynamic equation (7.3) is written as

$$m\ddot{\mathbf{p}} + \sum_{j=1}^{3} k_j \mathbf{p} - \mathbf{w} - m\mathbf{g} = 0, \tag{7.18}$$

where

$$\mathbf{w} = \sum_{j=1}^{3} k_j \mathbf{b}_j = m[v_1, v_2, 0]^T.$$

Periodic trajectories are then directly integrated from (7.18), namely

$$\mathbf{p} = \mathbf{p}_d + \mathbf{p}_s \tag{7.19}$$

with

$$\mathbf{p}_s = [x_s, y_s, z_s]^T = [-\frac{v_1}{\omega_n^2}, -\frac{v_2}{\omega_n^2}, -\frac{g}{\omega_n^2}]^T, \quad \omega_n^2 = \sum_{j=1}^{3} k_j/m,$$

and $\mathbf{p}_d = \mathbf{c}\cos\omega_n t + \mathbf{s}\sin\omega_n t$, with constant $\mathbf{c} = [\mu_{xc}, \mu_{yc}, \mu_{zc}]^T$ and $\mathbf{s} = [\mu_{xs}, \mu_{ys}, \mu_{zs}]^T$. Geometrically speaking, $\mathbf{p}_s$ represents the central static equilibrium position, and the *unbounded* $\mathbf{c}$ and $\mathbf{s}$ are design parameters that determine the shape of the motion, implying that these trajectories can extend beyond the static workspace. When trajectories of the real robot are

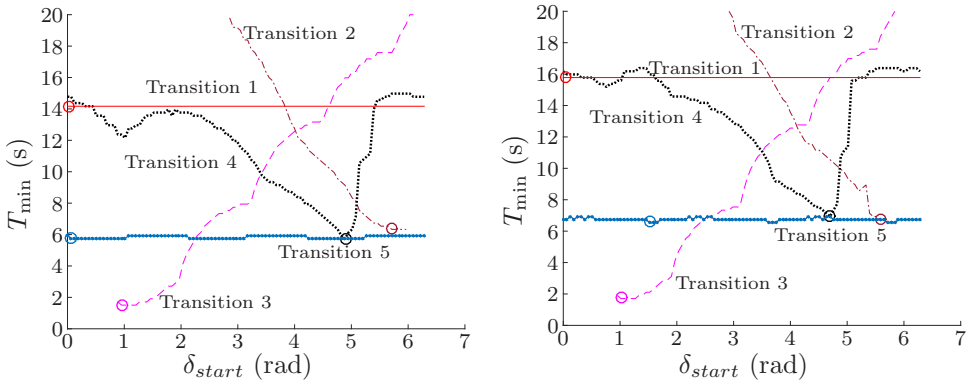

(a) Based on the 5-th degree polynomial. (b) Based on the 7-th degree polynomial.

Figure 7.4 – Optimized $T_{\min}$ and δ_{start}.

designed as in (7.19) with parameters $\mathbf{p}_s$ located in the static workspace, it can be guaranteed that the tensions in the cables will remain positive.

In the example, the robot is requested to start from the state of rest, merge into two consecutive ellipses, a straight line and a circle in sequence and then go back to the state of rest. All these target trajectories can be represented by (7.19) by selecting proper parameters $\mathbf{p}_s$, $\mathbf{c}$, and $\mathbf{s}$. For each transition, the robot moves along a source trajectory for one turn since its arrival, continues following this trajectory while preparing for the next transition within the first phase, then starts the transition to reach a goal trajectory at a proper departure point. The transition with its preparation stage is designed in (7.8) and (7.7).

Optimal values of the phase $\delta_{start} = \omega_n \delta_i$ that corresponds to the moment when the robot leaves trajectory i (the source trajectory) and the minimum time T_i for the transition from trajectory i to $i+1$ are fixed by sweeping the (δ_{start}, T_i) plane, as shown in Fig. 7.4. Points marked by a small circle represent the optimal values of δ_{start} and $T_{\min}$ for each transition. The strategy is as follows. For a given value of T_i and δ_{start}, the constraint of positive cable tensions during a transition trajectory is numerically verified through a discretization of time. Each point on the curves in Fig. 7.4 represents a feasible minimum T_i for each δ_{start}. Then, the global minimum value of $T_{\min}$ for all the values of δ_{start} in one period can be readily obtained.

Applying the optimized δ_{start} and $T_{\min}$, the example trajectory guarantees continuous and positive cable tensions, as is confirmed in Fig. 7.5. In this figure, a small triangle represents the moment at which the end-effector starts a transition while a small circle indicates the moment when the end-effector arrives and merges into the steady-state target trajectory. Additionally, the transition is able to start from/end with a resting position, as shown in Fig. 7.6. The advantage of using the 5-th degree polynomial is that the transition time is smaller than when using the the 7-th degree polynomial.

The complete trajectory, using the 5-th degree polynomial for its transitions, is illustrated in

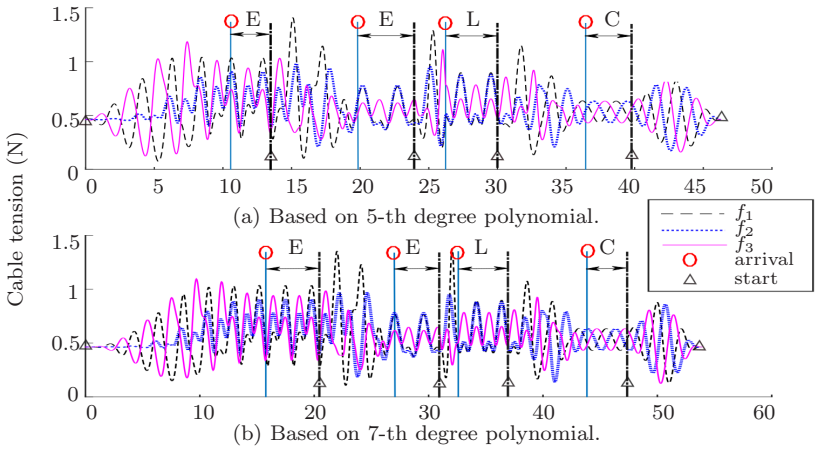

Figure 7.5 – Cable Tensions during the trajectory (E: Ellipse, L: Straight Line, C: Circle).

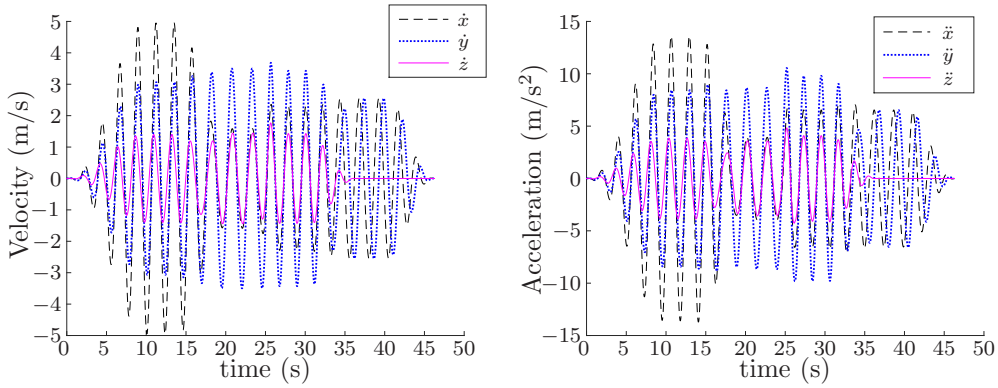

(a) Cartesian velocities. (b) Cartesian accelerations.

Figure 7.6 – Velocities and accelerations of the trajectory using the 5th degree polynomial.

Fig. 7.7. The transition trajectories using the 7-th degree polynomial are similar and thus the corresponding trajectory is not presented. As shown in Fig. 7.7, transition trajectories gradually go beyond the static workspace to join target trajectories which are located beyond the static workspace. Points marked by small triangles represent points at which the end-effector starts the transition and leaves the source trajectory while points marked by small circles represent the points at which the end-effector arrives at and merges into the steady-state target trajectory.

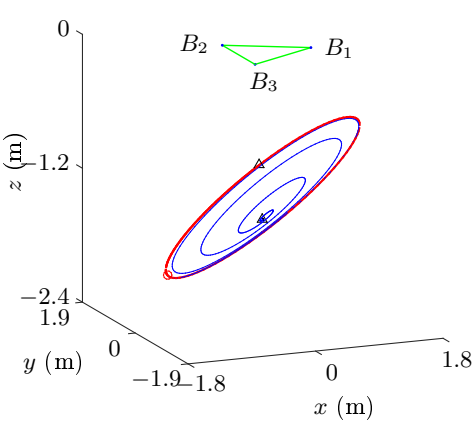

(a) Transition 1: state of rest to ellipse 1.

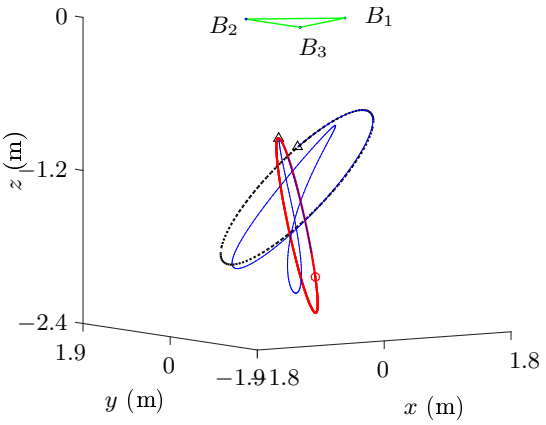

(b) Transition 2: ellipse 1 to ellipse 2.

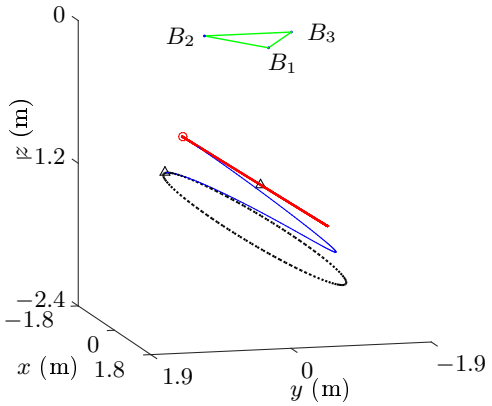

(c) Transition 3: ellipse 2 to straight line.

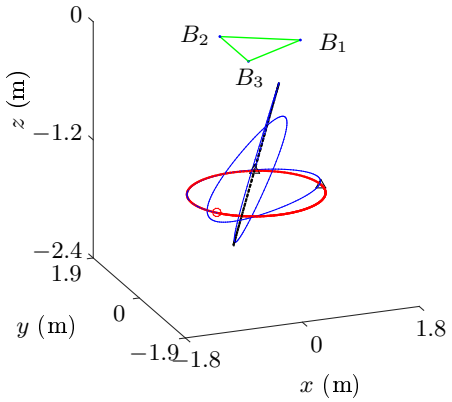

(d) Transition 4: straight line to circle.

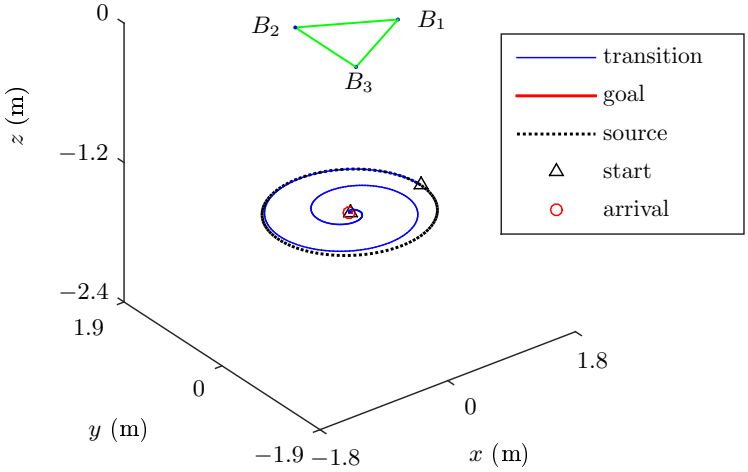

(e) Transition 5: circle to state of rest.

Figure 7.7 – Transition trajectories between periodic trajectories using the 5-th degree polynomial.

7.5 Conclusion

The contribution of this chapter lies in the definition of transition trajectories that can be used to chain multiple dynamic trajectories beyond a robot's static workspace in sequence, with continuity up to the acceleration level. The approach is relatively simple but effective: a target trajectory is gradually reached by approaching the amplitude and frequency of its parameters from that of its preceding trajectory, using proper time functions. Transition trajectories are obtained by optimizing the time offset of a source trajectory, corresponding to the departure time for a goal trajectory, and minimum execution time, as long as the cable tensions remain positive.

An example trajectory is performed by applying the novel technique to a specific mechanism. Periodic trajectories obtained in Chapter 2 are chosen as target trajectories. Using the transition trajectory proposed, the robot is able to smoothly start from the state of rest, merge into two consecutive ellipses, a straight line and a circle in sequence and then go back to the state of rest. In future work, time offsets will be added to both the source and goal trajectories such that optimal points at which the robot leaves for and lands on the goal trajectory can be obtained based on the minimization of the transitioning time or other criteria.

Discussion and Conclusion

The main contribution of this thesis is the introduction of trajectory planning and synthesis techniques that permit a fully actuated CSPR to move its end-effector *beyond* its static workspace in a controlled, predictable manner. Trajectories that involve variable stiffness equivalent springs and variable orientation are introduced, which is novel compared to previous work.

To the best of the author's knowledge, the results presented in this thesis are original in the field of dynamic trajectory planning for fully actuated CSPRs. This work has led to the publication of three conference proceedings papers and two journal articles (Jiang and Gosselin, 2014, 2015, 2016b,a, 2018). Two other journal articles have also been submitted (Jiang et al., a,b).

Discussion

The proposed trajectories are good candidates for applications that do not require high accuracy, such as photography, surveillance, artistic performances (Tempel et al., 2015), virtual reality and entertainment (Miermeister et al., 2016), and even for certain pick-and-place operations. Indeed, given the high velocities attained along the trajectories, high accuracy would be very difficult to achieve at all times. In a point-to-point trajectory, the positioning accuracy matters most at the target point and is not that important along the approach and recede segments of the trajectory. Moreover, when the trajectory is designed such that the end-effector passes through the important point at zero speed, the positioning accuracy can be maximized and the time spent *near* this point can also be maximized.

The experimental prototypes shown in the supplementary videos are only intended as a proof of concept that can demonstrate that the designed trajectories are feasible and clearly exit the static workspace. While the prototypes cannot achieve a high degree of accuracy, the experimental accuracy for similar CSPRs which are compatible with the proposed technique has been demonstrated. For example, in (Barnett and Gosselin, 2015a), a larger six-DOF CSPR with the same architecture was used as a 3D printer and built a 2.16-m-tall statue occupying a volume of 182 L. For this system, the positioning error for each cable is typically less than 1 mm, at speeds up to 0.3 m/s and accelerations up to 0.3 m/s^2. Additionally,

a three-DOF CSPR that positioned a point mass within a triangular-prism-shaped static workspace of side length 9 m achieved a positioning error on the order of 1 cm, with platform speeds of up to 6 m/s, which is deemed reasonable for pick-and-place operations within a large workspace (Gosselin and Foucault, 2015).

The chosen six-DOF CSPR architecture is an attractive option for many applications since it provides full translational and rotational control. However, it is not an obvious choice for CSPR applications that require positioning and orientation of the platform. For example, it may be argued that a three- or four-cable positioning robot with actuators *on the platform* (e.g., the SkyCam (Cone, 1985)) is a better choice because it eliminates cable interference issues and can provide full rotational control. Obviously, this architecture is a better choice for some applications. However, the chosen six-actuator, six-DOF architecture has many promising features, which were exploited in the applications described in (Gosselin and Bouchard, 2010; Barnett and Gosselin, 2015a). Firstly, the mechanism is fully parallel, with no actuators installed on the platform, thereby greatly simplifying the end-effector design and reducing its weight. Secondly, the chosen *crossing-cables* design resists off-centre-of-mass forces and a carefully balanced end-effector is therefore unnecessary. Additionally, with the proposed trajectory planning method, the dynamic-workpace-to-winch-footprint ratio is theoretically infinite. Obviously, the dynamic workspace is not relevant for applications that require the end-effector to stop and reach the state of rest at target points. However, the dynamic workspace is acceptable when the end-effector is only required to *pass through* target points.

Conclusion

First, an analytical way of planning periodic trajectories is introduced in the first part of the thesis. These trajectories can be guaranteed to be feasible, i.e., the cables are guaranteed to remain in tension during the whole trajectories. This approach is more straightforward and systematic compared to previous techniques that involved *directly* using dynamic equations. More importantly, it reveals the fundamental dynamic properties of CSPRs.

Natural frequencies as well as associated periodic trajectories are obtained from the integration of the dynamic model of an equivalent mass-spring system. These trajectories, referred to as natural trajectories, have no restriction on the amplitude, since they are the response of the linear system that is driven by springs with constant stiffness. The synthesis approach is applied in the trajectory planning of a three-DOF point-mass CSPR, in the translational component generation of a planar three-DOF CSPR and a spatial six-DOF CSPR. Additionally, for a planar three-DOF CSPR, the rotational component is determined from a nonlinear differential equation with constant coefficients. The combination of the translational component and the rotational component produces different types of trajectories that can involve variable rotations. All these trajectories are associated with constant-stiffness equivalent springs and

are guaranteed to be feasible since the cable tensions are always positive. Moreover, linear trajectories are designed for a six-DOF CSPR from the dynamic equations, by introducing the tilt-and-torsion angle convention. Natural trajectories as well as other trajectories associated with a linear system that is driven by springs with variable stiffness and corresponding global conditions that can keep the cables in tension are obtained. Example trajectories and the experimental implementation of these trajectories on prototypes are provided in order to illustrate the results.

Second, an approach for the generation of dynamic point-to-point trajectories for a three-DOF point-mass CSPR and a six-DOF CSPR is proposed in the second part of the thesis. These trajectories are used to chain a sequence of points that may locate beyond the static workspace of the robot. The technique ensures zero velocity at each of the target points and preserves the continuity up to the acceleration level, while satisfying cable tension constraints. The proposed technique provides a much more straightforward procedure for passing through a *sequence* of target points, when compared to the *periodic* method disclosed in the preceding part, which would require several *transition* trajectories to accomplish such a task. Additionally, the proposed unit-quaternion scheme can be used to interpolate between *arbitrary* orientations, as opposed to the method introduced in Chapter 4, which required the end-effector to face toward the z axis at all times. However, as mentioned in Chapter 4, an advantage of the technique is that the trajectories designed there are *guaranteed* to satisfy cable tension constraints.

Several essential ideas are incorporated within the proposed technique to make it simple and robust. Firstly, trajectory segments are planned one at a time, using a simplified segment function, the basis motion, and a straightforward procedure for imposing kinematic constraints. Secondly, quaternions are used to describe the rotational component. These parameters are free from singularities and are the preferred representation for interpolating between distant orientations. Finally, dynamic constraints are verified for all trajectory segments and an intermediate-point-finding procedure is provided for cases where this verification fails.

Third, a scheme for the design of transition trajectories is introduced in the third part. This technique can be used to go beyond the static workspace of the robot to connect a sequence of pre-defined feasible trajectories, and to start from/end with the state of rest. Compared to the method involved in previous work, this method is more general, since it can be applied to chain target points and target trajectories.

A general form is proposed, which allows the robot to automatically chain multiple trajectories in order at different starting points . A goal trajectory is gradually attained by approaching the amplitude parameters and frequencies from those of a source trajectory. For each transition, the departure point from its source trajectory is determined by minimizing the travel time to its goal trajectory. Example trajectories are provided to demonstrate the scheme.

Future Work

For periodic trajectory planning, the analytical approach that is used to explore natural trajectories could be extended to more complex trajectories of CSPRs. As an example, for six-DOF CSPRs, future work will involve extending the technique to permit the use of more complex linear trajectories and solutions to the nonlinear dynamic equations.

For point-to-point trajectory planning, the proposed synthesis technique could be improved to consider the interdependence among trajectory segments to a greater degree. This would eliminate the need for intermediate points and provide a better framework for optimizing trajectory parameters such as the travel time. Additionally, the concept of basis motions could be expanded to permit additional constraints for non-trigonometric curves such as splines.

The proposed technique could also be adapted for solving the more general problem of *finding* the sequence of points needed to reach a target that cannot be reached even when an intermediate point is used. For example, if the robot lies within the static workspace and a target point is far outside this workspace, it might need to oscillate back and forth several times before the target becomes feasible.

Additionally, for the point-to-point and transition trajectory planning, time functions only satisfy obvious conditions about continuity of the position and its derivatives up to a given order and other goals to be pursued could be considered. Among the different possibilities, the amplitude of the acceleration profile, in order to avoid efforts on the load due to inertial forces or vibrational effects of the mechanical structure could be taken into account. Moreover, analytical techniques could be used to facilitate the imposition of cable tension constraints during trajectory planning.

Bibliography

J. Albus, R. Bostelman, and N. Dagalakis. The NIST Robocrane. *Journal of Robotic Systems*, 10(5):709–724, 1993.

A. B. Alp and S. E. Agrawal. Cable suspended robots: design, planning and control. In *IEEE International Conference on Robotics and Automation (ICRA)*, volume 4, pages 4275–4280, 2002.

K. Azizian, P. Cardou, and B. Moore. Classifying the boundaries of the wrench-closure workspace of planar parallel cable-driven mechanisms by visual inspection. *ASME Journal of mechanisms and robotics*, 4(2):024503, 5 pages, 2012.

R. Babaghasabha, M. A. Khosravi, and H. D. Taghirad. Adaptive robust control of fully-constrained cable driven parallel robots. *Mechatronics*, 25:27 – 36, 2015.

M. Bamdad. Time-energy optimal trajectory planning of cable-suspended manipulators. In T. Bruckmann and A. Pott, editors, *Cable-Driven Parallel Robots: Proceedings of the First International Conference on Cable-Driven Parallel Robots*, pages 41–51. Springer, 2013.

E. Barnett and C. Gosselin. Large-scale 3D printing with a cable-suspended robot. *Additive Manufacturing*, 7:27–44, 2015a.

E. Barnett and C. Gosselin. Time-optimal trajectory planning of cable-driven parallel mechanisms for fully specified paths with G1-discontinuities. *ASME Journal of Dynamic Systems, Measurement, and Control*, 137(7):071007, 2015b.

G. Barrette and C. M. Gosselin. Determination of the dynamic workspace of cable-driven planar parallel mechanisms. *ASME Journal of Mechanical Design*, 127(2):242–248, 2005.

H. Baruh. *Analytical Dynamics*. WCB/McGraw-Hill, 1999.

A. Beléndez, C. Pascual, D. Méndez, T. Beléndez, and C. Neipp. Exact solution for the nonlinear pendulum. *Revista brasileira de ensino de física*, 29(4):645–648, 2007.

A. O. Belyakov, A. P. Seyranian, and A. Luongo. Dynamics of the pendulum with periodically varying length. *Physica D: Nonlinear Phenomena*, 238(16):1589–1597, 2009.

A. Berti, J.-P. Merlet, and M. Carricato. *Workspace Analysis of Redundant Cable-Suspended Parallel Robots*, pages 41–53. Springer International Publishing, Cham, 2015.

J. E. Bobrow, S. Dubowsky, and J. Gibson. Time-optimal control of robotic manipulators along specified paths. *The International Journal of Robotics Research*, 4(3):3–17, 1985.

O. Bohigas, M. Manubens, and L. Ros. Planning wrench-feasible motions for cable-driven hexapods. *IEEE Transactions on Robotics*, 32(2):442–451, April 2016.

I. A. Bonev, D. Zlatanov, and C. Gosselin. Advantages of the modified Euler angles in the design and control of PKMs. In *Parallel Kinematic Machines International Conference*, pages 171–188, Chemnitz, Germany, April 23-25 2002.

P. Bosscher and I. Ebert-Uphoff. Wrench-based analysis of cable-driven robots. In *IEEE International Conference on Robotics and Automation (ICRA)*, volume 5, pages 4950–4955, New Orleans, Louisiana, April 26 - May 1 2004.

T. Bruckmann, A. Pott, and M. Hiller. Calculating force distributions for redundantly actuated tendon-based stewart platforms. In *Advances in Robot Kinematics*, pages 403–412. Springer, 2006.

R. Campa and K. Camarillo. *Unit quaternions: A mathematical tool for modeling, path planning and control of robot manipulators*. INTECH Open Access Publisher, 2008.

W. B. Case. The pumping of a swing from the standing position. *American Journal of Physics*, 64(3):215–220, 1996.

W. B. Case and M. A. Swanson. The pumping of a swing from the seated position. *American Journal of Physics*, 58(5):463–467, 1990.

T. Chettibi, H. Lehtihet, M. Haddad, and S. Hanchi. Minimum cost trajectory planning for industrial robots. *European Journal of Mechanics - A/Solids*, 23(4):703 – 715, 2004.

L. L. Cone. Skycam: An aerial robotic camera system. *Byte*, 10(10):122, 1985.

D. Cunningham and H. H. Asada. The Winch-Bot: a cable-suspended, under-actuated robot utilizing parametric self-excitation. In *IEEE International Conference on Robotics and Automation (ICRA)*, pages 1844–1850, Kobe, Japan, May 12-17 2009.

E. B. Dam, M. Koch, and M. Lillholm. Quaternions, interpolation and animation. Technical report, 1998.

H. T. Davis. *Introduction to nonlinear differential and integral equations*. Courier Corporation, 1962.

J. Diebel. Representing attitude: Euler angles, unit quaternions, and rotation vectors. *Matrix*, 58(15-16):1–35, 2006.

P. Dion-Gauvin and C. Gosselin. Trajectory planning for the static to dynamic transition of point-mass cable-suspended parallel mechanisms. *Mechanism and Machine Theory*, 113:158 – 178, 2017.

B. R. Donald and P. G. Xavier. Provably good approximation algorithms for optimal kinodynamic planning for cartesian robots and open-chain manipulators. *Algorithmica*, 14(6): 480–530, 1995.

Q. Duan, V. Vashista, and S. K. Agrawal. Effect on wrench-feasible workspace of cable-driven parallel robots by adding springs. *Mechanism and Machine Theory*, 86:201–210, 2015.

H. R. Fahham and M. Farid. Minimum-time trajectory planning of spatial cable-suspended robots along a specified path considering both tension and velocity constraints. *Engineering Optimization*, 42(4):387–402, 2010.

I. Fantoni and R. Lozano. *Non-linear control for underactuated mechanical systems*. Springer Science & Business Media, 2002.

A. Fortin-Côté, P. Cardou, and C. Gosselin. A tension distribution algorithm for cable-driven parallel robots operating beyond their wrench-feasible workspace. In *International Conference on Control, Automation and Systems (ICCAS)*, pages 68–73, Gyeongju, Korea, October 16-19 2016.

T. Fraichard and C. Laugier. Path-velocity decomposition revisited and applied to dynamic trajectory planning. In *IEEE International Conference on Robotics and Automation (ICRA)*, volume 2, pages 40–45, Atlanta, Georgia, May 2-6 1993a.

T. Fraichard and C. Laugier. Dynamic trajectory planning, path-velocity decomposition and adjacent paths. In *International Joint Conference on Artificial Intelligence (IJCAI)*, pages 1592–1599, Chambéry, France, August 28 - September 3 1993b.

A. Gasparetto, P. Boscariol, A. Lanzutti, and R. Vidoni. *Path Planning and Trajectory Planning Algorithms: A General Overview*, pages 3–27. Springer International Publishing, Cham, 2015.

C. Gosselin. Cable-driven parallel mechanisms: state of the art and perspectives. *Mechanical Engineering Reviews*, 1(1):DSM0004, 17 pages, 2014.

C. Gosselin and A. Hadj-Messaoud. Automatic planning of smooth trajectories for pick-and-place operations. *ASME Journal of Mechanical Design*, 115(3):450–456, 1993.

C. Gosselin. Global planning of dynamically feasible trajectories for three-dof spatial cable-suspended parallel robots. In T. Bruckmann and A. Pott, editors, *Cable-Driven Parallel Robots: Proceedings of the First International Conference on Cable-Driven Parallel Robots*, pages 3–22. Springer, 2013.

C. Gosselin and M. Grenier. On the determination of the force distribution in overconstrained cable-driven parallel mechanisms. *Meccanica*, 46(1):3–15, 2011.

C. Gosselin, P. Ren, and S. Foucault. Dynamic trajectory planning of a two-dof cable-suspended parallel robot. In *IEEE International Conference on Robotics and Automation (ICRA)*, pages 1476–1481, St. Paul, Minnesota, May 14–18 2012.

C. Gosselin and S. Foucault. Dynamic point-to-point trajectory planning of a two-dof cable-suspended parallel robot. *IEEE Transactions on Robotics*, 30(3):728–736, 2014.

C. Gosselin and S. Foucault. Experimental determination of the accuracy of a three-dof cable suspended parallel robot performing dynamic trajectories. In A. Pott and T. Bruckmann, editors, *Cable-Driven Parallel Robots: Proceedings of the Second International Conference on Cable-Driven Parallel Robots*, pages 101–112. Springer International Publishing, 2015.

C. M. Gosselin and S. Bouchard. A gravity-powered mechanism for extending the workspace of a cable-driven parallel mechanism: Application to the appearance modelling of objects. *International Journal of Automation Technology*, pages 372–379, July 2010.

M. Gouttefarde and C. Gosselin. Analysis of the wrench-closure workspace of planar parallel cable-driven mechanisms. *IEEE Transactions on Robotics*, 22(3):434–445, June 2006.

M. Gouttefarde, J.-P. Merlet, and D. Daney. *Determination of the wrench-closure workspace of 6-DOF parallel cable-driven mechanisms*, pages 315–322. Springer Netherlands, Dordrecht, 2006.

M. Gouttefarde, D. Daney, and J. P. Merlet. Interval-analysis-based determination of the wrench-feasible workspace of parallel cable-driven robots. *IEEE Transactions on Robotics*, 27(1):1–13, 2011.

M. Gouttefarde, J. F. Collard, N. Riehl, and C. Baradat. Geometry selection of a redundantly actuated cable-suspended parallel robot. *IEEE Transactions on Robotics*, 31(2):501–510, 2015a.

M. Gouttefarde, J.-P. Merlet, and D. Daney. Wrench-feasible workspace of parallel cable-driven mechanisms. In *IEEE International Conference on Robotics and Automation (ICRA)*, pages 1492–1497, Roma, Italy, April 10- 14 2007.

M. Gouttefarde, J. Lamaury, C. Reichert, and T. Bruckmann. A versatile tension distribution algorithm for n-dof parallel robots driven by $n+2$ cables. *IEEE Transactions on Robotics*, 31(6):1444–1457, 2015b.

E. Idá, A. Berti, T. Bruckmann, and M. Carricato. Rest-to-rest trajectory planning for planar underactuated cable-driven parallel robots. In C. Gosselin, P. Cardou, T. Bruckmann, and A. Pott, editors, *Cable-Driven Parallel Robots: Proceedings of the Third International Conference on Cable-Driven Parallel Robots*, pages 207–218, Québec, Canada, August 2–4 2018.

X. Jiang and C. Gosselin. Dynamic point-to-point trajectory planning of a three-dof cable-suspended parallel robot. *IEEE Transactions on Robotics*, 32(6):1550–1557, 2016a.

X. Jiang and C. Gosselin. Dynamic transition trajectory planning of three-dof cable-suspended parallel robots. In C. Gosselin, P. Cardou, T. Bruckmann, and A. Pott, editors, *Cable-Driven Parallel Robots: Proceedings of the Third International Conference on Cable-Driven Parallel Robots*, pages 231–242, Québec, Canada, August 2–4 2018.

X. Jiang, E. Barnett, and C. Gosselin. Periodic trajectory planning beyond the static workspace for six-dof cable-suspended parallel robots. *submitted as T-RO paper number 17-0208*, a.

X. Jiang, E. Barnett, and C. Gosselin. Dynamic point-to-point trajectory planning for six-dof cable-suspended parallel robots using a basis motion and unit quaternions. *submitted as T-RO paper number 17-0357*, b.

X. Jiang and C. Gosselin. Dynamically feasible trajectories for three-dof planar cable-suspended parallel robots. In *38th Mechanisms and Robotics Conference (ASME/IDETC)*, pages V05AT08A085, 10 pages, Buffalo, New York, August 17–20 2014.

X. Jiang and C. Gosselin. Trajectory generation for three-degree-of-freedom cable-suspended parallel robots based on analytical integration of the dynamic equations. In *39th Mechanisms and Robotics Conference (ASME/IDETC)*, pages V05AT08A051, 9 pages, Boston, Massachusetts, August 2–5 2015.

X. Jiang and C. Gosselin. Trajectory generation for three-degree-of-freedom cable-suspended parallel robots based on analytical integration of the dynamic equations. *ASME Journal of Mechanisms and Robotics*, 8(4):041001–1–041001–9, 2016b.

S. Kawamura, W. Choe, S. Tanaka, and S. R. Pandian. Development of an ultrahigh speed robot falcon using wire drive system. In *IEEE International Conference on Robotics and Automation (ICRA)*, volume 1, pages 215–220, Nagoya, Aichi, Japan, 1995.

S. Kawamura, H. Kino, and C. Won. High-speed manipulation by using parallel wire-driven robots. *Robotica*, 18(1):13–21, 001 2000.

M. A. Khosravi and H. D. Taghirad. Robust PID control of fully-constrained cable driven parallel robots. *Mechatronics*, 24(2):87 – 97, 2014.

M. Korayem and M. Bamdad. Dynamic load-carrying capacity of cable-suspended parallel manipulators. *The International Journal of Advanced Manufacturing Technology*, 44(7): 829–840, 2009.

M. Korayem, E. Davarzani, and M. Bamdad. Optimal trajectory planning with the dynamic load carrying capacity of a flexible cable-suspended manipulator. *Scientia Iranica Transaction B-Mechanical Engineering*, 17(4):315–326, 2010.

M. H. Korayem, M. Bamdad, H. Tourajizadeh, A. H. Korayem, and S. Bayat. Analytical design of optimal trajectory with dynamic load-carrying capacity for cable-suspended manipulator. *The International Journal of Advanced Manufacturing Technology*, 60(1):317–327, 2012.

W. Kraus. *Force Control of Cable-Driven Parallel Robots Force Control of Cable-Driven Parallel Robots*. Ph. D. thesis, Stuttgarter Beiträge Zur Produktionsforschung, 2015.

J. Lamaury and M. Gouttefarde. Control of a large redundantly actuated cable-suspended parallel robot. In *IEEE International Conference on Robotics and Automation (ICRA)*, pages 4659–4664, Karlsruhe, Germany, May 6-10 2013.

J. Lamaury, M. Gouttefarde, M. Michelin, and O. Tempier. *Design and Control of a Redundant Suspended Cable-Driven Parallel Robots*, pages 237–244. Springer Netherlands, Dordrecht, 2012.

S. M. LaValle. *Planning Algorithms*. Cambridge University Press, Cambridge, U.K., 2006. Available at http://planning.cs.uiuc.edu/.

S. Lefrançois and C. Gosselin. Point-to-point motion control of a pendulum-like 3-dof underactuated cable-driven robot. In *IEEE International Conference on Robotics and Automation (ICRA)*, pages 5187–5193, Anchorage, AK, USA, May 03-08 2010.

T. Li, X. Tang, and L. Tang. Algebraic expression and characteristics of static wrench-closure workspace boundary for planar cable-driven parallel robots. *Advances in Mechanical Engineering*, 8(3):1687814016638217, 2016.

Z. Liu, X. Tang, Z. Shao, L. Wang, and L. Tang. Research on longitudinal vibration characteristic of the six-cable-driven parallel manipulator in fast. *Advances in Mechanical Engineering*, 5:547416, 2013.

J. Y. Luh and M. W. Walker. Mininum-time along the path for a mechanical arm. In *IEEE Conference on Adaptive Processes and A Special Symposium on Fuzzy Set Theory and Applications*, pages 755–759, New Orleans, LA, USA, December 7-9 1977.

J. B. Marion. *Classical dynamics of particles and systems.* Academic Press, 2013.

J.-P. Merlet. *Wire-driven Parallel Robot: Open Issues*, pages 3–10. Springer Vienna, Vienna, 2013.

P. Miermeister, M. Lächele, R. Boss, C. Masone, C. Schenk, J. Tesch, M. Kerger, H. Teufel, A. Pott, and H. H. Bülthoff. The CableRobot simulator large scale motion platform based on cable robot technology. In *IEEE/RSJ International Conference on Intelligent Robots and Systems (IROS)*, pages 3024–3029, Daejeon, Korea, October 9-14 2016.

A. Ming and T. Higuchi. Study on multiple degree-of-freedom positioning mechanism using wires. 1. concept, design and control. *International Journal of the Japan Society for Precision Engineering*, 28(2):131–138, 1994.

R. Nan, D. Li, C. Jin, Q. Wang, L. Zhu, W. Zhu, H. Zhang, Y. Yue, and L. Qian. The five-hundred-meter aperture spherical rodio telescope(FAST) project. *International Journal of Modern Physics D*, 20(06):989–1024, 2011.

D. Q. Nguyen, M. Gouttefarde, O. Company, and F. Pierrot. On the simplifications of cable model in static analysis of large-dimension cable-driven parallel robots. In *IEEE/RSJ International Conference on Intelligent Robots and Systems (IROS)*, pages 928–934, Tokyo, Japan, November 3-7 2013.

S.-R. Oh and S. K. Agrawal. Cable-suspended planar parallel robots with redundant cables: controllers with positive cable tensions. In *IEEE International Conference on Robotics and Automation (ICRA)*, volume 3, pages 3023–3028, Taipei, China, September 14-19 2003.

S. Perreault, P. Cardou, C. M. Gosselin, and M. J.-D. Otis. Geometric determination of the interference-free constant-orientation workspace of parallel cable-driven mechanisms. *ASME Journal of Mechanisms and Robotics*, 2(3):031016, 2010.

F. Pfeiffer and R. Johanni. A concept for manipulator trajectory planning. *IEEE Journal on Robotics and Automation*, 3(2):115–123, 1987.

B. Piccoli and J. Kulkarni. Pumping a swing by standing and squatting: do children pump time optimally? *IEEE Control Systems*, 25(4):48–56, 2005.

A. Pott and W. Kraus. Determination of the wrench-closure translational workspace in closed-form for cable-driven parallel robots. In *IEEE International Conference on Robotics and Automation (ICRA)*, pages 882–887, Stockholm, Sweden, May 16-21 2016.

A. Pott. An improved force distribution algorithm for over-constrained cable-driven parallel robots. In *Computational Kinematics*, pages 139–146. Springer, 2014.

J. Pusey, A. Fattah, S. Agrawal, and E. Messina. Design and workspace analysis of a 6–6 cable-suspended parallel robot. *Mechanism and Machine Theory*, 39(7):761 – 778, 2004.

C. Reichert, K. Müller, and T. Bruckmann. *Robust Internal Force-Based Impedance Control for Cable-Driven Parallel Robots*, pages 131–143. Springer International Publishing, Cham, 2015.

A. T. Riechel and I. Ebert-Uphoff. Force-feasible workspace analysis for underconstrained, point-mass cable robots. In *IEEE International Conference on Robotics and Automation (ICRA)*, volume 5, pages 4956–4962, New Orleans, Louisiana, April 26 - May 01 2004.

V. Schmidt, W. Kraus, W. Y. Ho, J. Seon, A. Pott, J. O. Park, and A. Verl. Extending dynamic trajectories of cable-driven parallel robots as a novel robotic roller coaster. In *International Symposium on Robotics (ISR/Robotik)*, pages 1–7, Entrance East, Munich, Germany, June 02–03 2014.

Z. Shiller and H. Lu. Computation of path constrained time optimal motions with singularities. *ASME Journal of dynamic systems measurement and control*, 114(1):34–40, 1992. ISSN 00220434.

Z. Shiller and S. Dubowsky. Robot path planning with obstacles, actuator, gripper, and payload constraints. *The International Journal of Robotics Research*, 8(6):3–18, 1989.

K. Shin and N. McKay. Minimum-time control of robotic manipulators with geometric path constraints. *IEEE Transactions on Automatic Control*, 30(6):531–541, 1985a.

K. Shin and N. McKay. Minimum-time control of robotic manipulators with geometric path constraints. *IEEE Transactions on Automatic Control*, 30(6):531–541, 1985b.

K. Shoemake. Animating rotation with quaternion curves. In *ACM SIGGRAPH computer graphics*, volume 19, pages 245–254. ACM, 1985.

D. S. Stilling and W. Szyszkowski. Controlling angular oscillations through mass reconfiguration: a variable length pendulum case. *International Journal of Non-Linear Mechanics*, 37 (1):89–99, 2002.

E. Stump and V. Kumar. Workspaces of cable-actuated parallel manipulators. *ASME Journal of Mechanical Design*, 128(1):159–167, 2006.

P. Tempel, F. Schnelle, A. Pott, and P. Eberhard. Design and programming for cable-driven parallel robots in the German Pavilion at the EXPO 2015. *Machines*, 3(3):223–241, 2015.

P. Veronesi. Classical dynamics of particles and systems. *Il Nuovo Cimento A (1965-1970)*, 4 (2):431–432, 1971.

R. Yao, X. Tang, J. Wang, and P. Huang. Dimensional optimization design of the four-cable-driven parallel manipulator in FAST. *IEEE/ASME Transactions on Mechatronics*, 15(6): 932–941, 2010.

D. Zanotto, G. Rosati, and S. K. Agrawal. Modeling and control of a 3-dof pendulum-like manipulator. In *IEEE International Conference on Robotics and Automation (ICRA)*, pages 3964–3969, Shanghai, China, May 09–13 2011.

N. Zhang, W. Shang, and S. Cong. Geometry-based trajectory planning of a 3-3 cable-suspended parallel robot. *IEEE Transactions on Robotics*, 33(2):484–491, 2017.

N. Zhang and W. Shang. Dynamic trajectory planning of a 3-dof under-constrained cable-driven parallel robot. *Mechanism and Machine Theory*, 98:21 – 35, 2016.

L. Ẑlajpah. On time optimal path control of manipulators with bounded joint velocities and torques. In *IEEE International Conference on Robotics and Automation (ICRA)*, volume 2, pages 1572–1577, Minneapolis, MN, USA, April 22-28 1996.

N. Zoso and C. Gosselin. Point-to-point motion planning of a parallel 3-dof underactuated cable-suspended robot. In *IEEE International Conference on Robotics and Automation (ICRA)*, pages 2325–2330, St. Paul, MN, USA, May 14–18 2012.